

RESEARCH REPORT
Agreement T4118, Task 05
Rapid Construction

ANCHORAGE OF LARGE-DIAMETER REINFORCING BARS GROUTED INTO DUCTS

by

Kyle P. Steuck
Graduate Research Assistant

Jason B.K. Pang
Graduate Research Assistant

Marc O. Eberhard
Professor

John F. Stanton
Professor

Department of Civil and Environmental Engineering
University of Washington, Box 352700
Seattle, Washington 98195

Washington State Transportation Center (TRAC)
University of Washington, Box 354802
1107NE 45th Street, Suite 535
Seattle, Washington 98105-4631

Prepared for
Washington State Transportation Commission
Department of Transportation
and in cooperation with
U.S. Department of Transportation
Federal Highway Administration

July 2008

TECHNICAL REPORT STANDARD TITLE PAGE

1. REPORT NO. WA-RD 684.1		2. GOVERNMENT ACCESSION NO.		3. RECIPIENT'S CATALOG NO.	
4. TITLE AND SUBTITLE ANCHORAGE OF LARGE-DIAMETER REINFORCING BARS GROUTED INTO DUCTS				5. REPORT DATE July 2008	
				6. PERFORMING ORGANIZATION CODE	
7. AUTHORS Kyle P. Steuck, Jason B.K. Pang, Marc O. Eberhard John F. Stanton				8. PERFORMING ORGANIZATION CODE	
9. PERFORMING ORGANIZATION NAME AND ADDRESS Washington State Transportation Center University of Washington, Box 354802 University District Building, 1107 NE 45th Street, Suite 535 Seattle, Washington (98105-7370)				10. WORK UNIT NO.	
				11. CONTRACT OR GRANT NUMBER T4118, Task 05	
12. SPONSORING AGENCY NAME AND ADDRESS Research Office Washington State Department of Transportation Transportation Building, MS 47372 Olympia, Washington 98504-7372 Project Manager: Kim Willoughby, 360-705-7978				13. TYPE OF REPORT AND PERIOD COVERED Research Report	
				14. SPONSORING AGENCY CODE	
15. SUPPLEMENTARY NOTES					
16. ABSTRACT <p>The use of a few large-diameter reinforcing bars for the construction of precast concrete bridge bents allows simplified construction by reducing the number of alignments to be made in the field. These bars are grouted into ducts in a precast concrete cap beam. In the proposed precast concrete substructure system, the grouted bars carry tensile forces across the joint between the column and cap beam. This joint is the yielding element in the structural system, and it is crucial to the performance of the structure that the bars yield before other failure mechanisms, including bond failure, occur. However, the cap beam is typically insufficient to anchor the bar, as the depth of the beam is substantially less than the American Association of State Highway and Transportation Officials (AASHTO) bridge code allows.</p> <p>For this project, 17 pullout tests were conducted to determine the bond characteristics and development length of large-diameter bars grouted into ducts. The bars tested ranged in size from #8 to #18. Pullout tests conducted with embedment lengths of at least six bar diameters yielded the reinforcing bar, while the test conducted with an embedment length of 14 bar diameters resulted in bar fracture.</p> <p>The tests and subsequent analysis showed that the bond of these grouted connections is significantly better than the bond of bars cast directly into concrete. The development lengths needed to fully anchor the bar are therefore within the depth available in the cap beam.</p>					
17. KEY WORDS Bond strength, deformed bars, cement grouts, precast concrete, bridge substructures, joint construction, bents, anchorage, ducts				18. DISTRIBUTION STATEMENT	
19. SECURITY CLASSIF. (of this report)		20. SECURITY CLASSIF. (of this page)		21. NO. OF PAGES	22. PRICE

DISCLAIMER

The contents of this report reflect the views of the authors, who are responsible for the facts and the accuracy of the data presented herein. The contents do not necessarily reflect the official views or policies of the Washington State Transportation Commission, Washington State Department of Transportation, or Federal Highway Administration. This report does not constitute a standard, specification, or regulation.

CONTENTS

EXECUTIVE SUMMARY	xiii
Objectives	xiii
Background	xiii
Results	xiii
Conclusions	xiv
CHAPTER 1: INTRODUCTION.....	1
1.1 Precast Concrete Construction for Rapid Construction of Bridges	1
1.2 Proposed Precast Substructure System	3
1.3 The Importance of Bond to the Proposed System	4
1.4 The Mechanism of Bond.....	5
1.5 Code Development Length Expressions.....	7
1.6 Previous Research.....	8
1.7 Research Program	9
1.8 Organization of Report	10
CHAPTER 2: EXPERIMENTAL PROGRAM	11
2.1 Overview of Testing	11
2.2 Specimen Design	13
2.3 Materials	14
2.3.1 Concrete.....	14
2.3.2 Ducts	14
2.3.3 Reinforcing Bars	15
2.3.4 Grout	16
2.3.5 Fibers	17
2.4 Test Bar Grouting Procedure	18
2.5 Loading Apparatus.....	18
2.5.1 Reaction Block.....	19
2.5.2 Rams	21
2.5.3 Load Cell.....	21
2.5.4 Grips.....	21
2.6 Instrumentation	22
2.6.1 Load Cell.....	22
2.6.2 Linear Potentiometers	23
2.6.3 Strain Gages.....	24
2.7 Test Procedure	25
2.7.1 Setup	25
2.7.2 Pullout Test.....	25
2.7.3 Post-Test Reset	26
CHAPTER 3: RESULTS OF MATERIAL TESTS.....	27
3.1 Reinforcing Bar Geometry.....	27
3.2 Reinforcing Bar Stress-Strain Data.....	30
3.3 Grout Strengths	31

3.4	Concrete Strengths	33
CHAPTER 4: PULLOUT RESULTS		34
4.1	Peak Results	34
4.2	Force-Displacement Behavior	35
4.2.1	Calculation of Front-End Slip	36
4.2.2	Short-Embedment Length Tests	37
4.2.3	Long-Embedment Length Tests	39
4.3	Damage Observations	40
4.3.1	Short-Embedment Length Tests	41
4.3.2	18S04	44
4.3.3	Long-Embedment Length Tests	46
4.3.4	Scaled Tests	48
CHAPTER 5: DISCUSSION OF FINDINGS		50
5.1	Grout Failure Mechanisms	50
5.2	Effect of Grout Strength	52
5.3	Effect of Fibers	55
5.4	Effect of Bar Size and Geometry	57
5.4.1	Full-Scale Tests	58
5.4.2	Scaling for Joint Tests	60
5.5	Effect of Yielding	61
5.6	Comparison to Codes and Previous Research	62
CHAPTER 6: LINEAR AND NONLINEAR MODELING		64
6.1	Linear Model	64
6.1.1	Model Form	64
6.1.2	Model Calibration	66
6.2	Nonlinear Bond Model	70
6.2.1	Key Variables	71
6.2.2	Unconfined Model	71
6.2.3	Confined Model	72
6.2.4	Comparison to Other Bond Models	75
6.3	Nonlinear Analysis Method	76
6.4	Results of Nonlinear Model	78
6.4.1	Peak Loads by Test	78
6.4.2	Force-Displacement Behavior	80
6.4.3	Bond Stress Distribution	81
6.4.4	Development Length	83
CHAPTER 7: CONCLUSIONS		86
7.1	Conclusions	86
7.2	Implementation Recommendations	87
7.3	Suggestions for Further Research	87
REFERENCES		89

APPENDIX A: SYSTEM TABLE AND SCHEMATIC DRAWINGS.....	A-1
APPENDIX B: NET STRESS-STRAIN PLOTS	B-1
APPENDIX C: FORCE-DISPLACEMENT PLOTS	C-1
APPENDIX D: FEM CODE	D-1
APPENDIX E: MODEL RESULTS.....	E-1

FIGURES

<u>Figure</u>	<u>Page</u>
1.1 Schematic of two-column bent with moment diagram from seismic loading	1
1.2 Comparison of reinforced concrete (left) and precast (right) column-to-cap beam joints	2
1.3 Displaced columns and rotations	3
1.4 Big bar system.....	4
1.5 Equilibrium of pullout test.....	6
2.1 Tests performed in each specimen.....	13
2.2 Bamboo ribs on a #18 bar	16
2.3 Preliminary grout strengths.....	17
2.4 Test setup	19
2.5 Annuli of contact for ram and reaction block	20
2.6 Reaction block design.....	20
2.7 Triple ram used to yield and fracture #18 bars	21
2.8 Wedge grip design	22
2.9 Schematic of instrumentation bridge with pots	23
2.10 Photo of pots for test 18N02	24
3.1 Bar dimensions for net area calculations	28
3.2 Bar dimensions for relative rib area.....	29
3.3 Net stress-strain curve.....	31
3.4 Test mix grout strengths	32
4.1 Peak nominal bar stress vs L_e/db	35
4.2 Bar stretch above the grout surface.....	36
4.3 Short-embedment length force-displacement curves.....	37
4.4 Ascending branch of short, no fiber, #18 tests	38
4.5 Force-displacement: 18N08.....	39
4.6 Force-displacement to yield: 18N08.....	40
4.7 Grout cone: 18F02	42
4.8 Grout cone: 18N02.....	42
4.9 Layered grout cone: 14N08	43
4.10 Grout cone and sheared grout: 18F04.....	44
4.11 Force-displacement: 18S04.....	45
4.12 Reinforcement: 18S04	45
4.13 Concrete splitting: 18S04.....	46
4.14 Fractured bar: 18N14	47
4.15 Concrete damage: 08C08.....	48
4.16 Grout damage: 08N08.....	48
5.1 Struts in grout.....	51
5.2 τ_{avg} vs grout strength	52
5.3 τ_{avg} vs L_e	53

5.4	τ_{avg}/Γ'_g vs l_e	54
5.5	$\tau_{avg}/\sqrt{f'_g}$ vs l_e	55
5.6	Fiber and no fiber bond stress-displacement comparison.....	56
5.7	Ascending branch of bond-slip histories	57
5.8	Eight-db embedment length tests.....	58
5.9	Four-db embedment length tests.....	59
5.10	Initial response of four- d_b embedment length tests	60
5.11	Scaling comparison.....	61
5.12	Stress vs l_e/d_b with predictions.....	63
6.1	Slip distributions for varying λL_e values	66
6.2	Bond stiffness calculation	67
6.3	Local bond stiffnesses.....	68
6.4	Back-end slip for test 18N08	70
6.5	Unconfined bond model.....	72
6.6	Assumed strain and slip distributions	74
6.7	Confined bond model.....	75
6.8	Bond model comparison	76
6.9	Schematic of the nonlinear model.....	77
6.10	Steel constitutive model.....	77
6.11	Peak loads from FEM and experiments.....	79
6.12	Test and FEM force-displacement comparison	80
6.13	Bond stress distributions.....	81
6.14	Slip distributions.....	83
6.15	FEM development length predictions.....	84

TABLES

<i>Table</i>		<i>Page</i>
2.1	Test matrix	12
2.2	Duct dimensions.....	15
3.1	Bar dimensions.....	27
3.2	Yield stresses and elastic moduli	30
3.3	Test day grout strengths.....	32
4.1	Peak resistances	34
6.1	Average and local bond stiffness	68
6.2	Bond stiffnesses and slip fractions.....	69

LIST OF SYMBOLS

A	Bar cross sectional area
A_{avg}	Average bar area
A_b	Bar area (AASHTO)
A_{net}	Net bar area
A_{nom}	Nominal bar area
c_b	Bar spacing (ACI)
d_b	Bar diameter
d_{duct}	Duct diameter
E	Elastic modulus
f'_c	Concrete compressive strength
f'_g	Grout compressive strength
f_y	Steel yield stress
h_r	Height of reinforcing bar deformation
k	Local bond stiffness
K	Average bond stiffness
K_{tr}	Transverse reinforcement index (ACI)
L_{air}	Length between grout surface and pot measurement
L_{bar}	Length of measured bar
L_e	Embedment length
$L_{unconfined}$	Length of unconfined region (cone)
l_d	Development length
P	Axial load on reinforcing bar
$P_{unconfined}$	Load accounted for in unconfined region
S_r	Spacing of deformations on reinforcing bar
u	Displacement in direction of pulled bar
u_{air}	In-air stretch of the reinforcing bar
$u_{confined}$	Displacement of the midpoint of the confined region
$u_{surface}$	Displacement at the grout surface
u_{pot}	Displacement measured by the linear potentiometers
u_{mid}	Displacement calculated at midpoint of the embedded length
W_{actual}	Weight of a section of reinforcing bar
W_{nom}	Weight per unit length of reinforcing bar as given by ASTM
w_r	Width of deformation on reinforcing bar
x	Distance along reinforcing bar
β	Slip fraction (see Chapter 6)
γ	Shear strain
ε	Axial strain
ε_{air}	Bar strain measured by strain gages
ε_{cone}	Calculated bar strain at the base of the unconfined region
λ	Stiffness parameter (see Chapter 6)
Π	Bar perimeter
σ	Bar stress
σ_{avg}	Bar stress calculated using average area
σ_{net}	Bar stress calculated using net area

σ_{nom}	Bar stress calculated using nominal area
σ_u	Ultimate bar stress
τ	Bond stress on bar surface
τ_{avg}	Average bond stress on bar surface
τ_{duct}	Average bond stress on duct surface
Ψ_e	Epoxy coating factor (ACI)
Ψ_s	Size factor (ACI)
Ψ_t	Top bar factor (ACI)

EXECUTIVE SUMMARY

OBJECTIVES

This research program consisted of experimental tests and numerical simulations of the anchorage of large-diameter reinforcing bars grouted into steel ducts. The research was conducted to support the development of a new precast column and beam system, which is intended to help accelerate the construction of bridge bents in seismically active regions. In this system, a small number of large-diameter reinforcing bars project from the top of the column into large ducts cast into the cap beam. The bars are then grouted in the ducts to provide continuity. These large-diameter ducts, formed with 8-inch corrugated steel pipe, allow the proposed system to be constructed easily in the field.

BACKGROUND

In the proposed system, the grouted bars carry tensile forces across the joint between the column and cap beam. This joint is the yielding element in the structural system, and it is crucial to the performance of the structure that the bars yield before other failure mechanisms, including bond failure, occur. The bars must therefore be fully developed.

The experimental program consisted of 17 monotonic pullout tests on bars ranging in size from No. 8 to No. 18 and with embedment lengths of 2 to 14 bar diameters. Both fiber-reinforced and unreinforced grouts were tested. The tests on No. 8 bars were conducted in scaled ducts to replicate the sizes used in the scaled beam-column joint tests.

RESULTS

In fourteen of the seventeen tests, failure occurred by bar pullout through the grout. Near the surface of the grout, a cone also pulled out. Over the remaining embedded length, a cylinder, consisting of the bar surrounded by an annulus of grout captured between the lugs, pulled through the surrounding grout. This shearing cylinder provided greater bond resistance per unit area than did the unconfined cone region. Two

tests (18S04 and 08C08) resulted in concrete splitting failures, and one test (18N14) resulted in bar fracture.

Reinforcing the grout with fibers did not provide any advantage in the monotonic pullout tests. As mixed, the presence of fibers reduced the compressive strength of the grout. The unreinforced grout used in the majority of these tests had an average strength of 8.5 ksi on test day, five days after placing the grout. The fiber-reinforced grout averaged 7.3 ksi on test day. In the tests with fiber-reinforced grout, the pullout resistance was typically lower than in the equivalent tests with unreinforced grout.

Constitutive bond-slip relationships were developed from the results of tests with short embedment lengths. In these tests, the slip was almost the same all along the embedded length, so it was assumed that the local shear stress was also uniformly distributed and equal to the average. The constitutive bond-slip relationships were incorporated into analytical models of the pullout tests. The accuracy of these models was confirmed by the results from the long-embedment length tests. The models were used to determine the necessary embedment lengths to achieve various bar stresses, including yield and fracture.

CONCLUSIONS

Testing and analysis of the anchorage of large-diameter bars grouted into ducts showed that these bars can be developed in much shorter lengths than current code expressions suggest. In the test program, a No. 18 bar was developed to fracture with an anchorage length of 14 bar diameters (31.5 inches). The analytical model suggests that fracture could be achieved with a development length of 10 bar diameters. Further tests on bars with embedment lengths between these two values, to confirm the precise embedment length needed to achieve fracture, were not conducted. These development lengths are much shorter than the development lengths given by the American Association of State Highway and Transportation Officials (AASHTO) for bars embedded in concrete.

Because the grouted bars develop in shorter lengths than bars embedded in concrete, bar anchorage is not a barrier to implementation of the proposed precast column and cap beam system. The depth available in typical cap beams (about 42 inches) is much greater than the monotonic development length for No. 18 bars (about 16 inches).

The cap beam is sufficiently deep to accommodate a development length with both a 50 percent increase to allow for cyclic loading and an eight-bar-diameter debonded length. Debonding the reinforcing bars in the grouted duct may be desirable to reduce the strain concentration in the bar at the joint.

CHAPTER 1: INTRODUCTION

1.1 PRECAST CONCRETE CONSTRUCTION FOR RAPID CONSTRUCTION OF BRIDGES

Typical cast-in-place (CIP) bridge construction practice requires that concrete substructures be built on site. This practice involves a number of time-consuming on-site activities, such as tying the reinforcement, building formwork, pouring concrete, waiting for concrete to cure, and removing formwork. It is important to accelerate this construction sequence because the indirect costs of time on site are high. Reducing the time required on site improves worker safety, and decreases disruption to traffic flow, and any reduction in the use of site-cast-concrete mitigates environmental impact (Wacker 2005).

Previous research at the University of Washington, in coordination with the Washington State Department of Transportation (WSDOT), contractors, and precast concrete fabricators, developed several bridge structural systems that shorten construction time. A summary of these systems, their strengths and weaknesses, and schematic drawings can be found in Appendix A. These systems use precast concrete to fabricate the columns and cap beams of the bridge substructure, just as many current designs utilize precast girders for the superstructure. The current research effort aimed to develop a precast concrete column-to-cap beam connection that can be used for multi-column bent caps, as shown in Figure 1.1 with the column-to-cap beam connection region shown enclosed in a box.

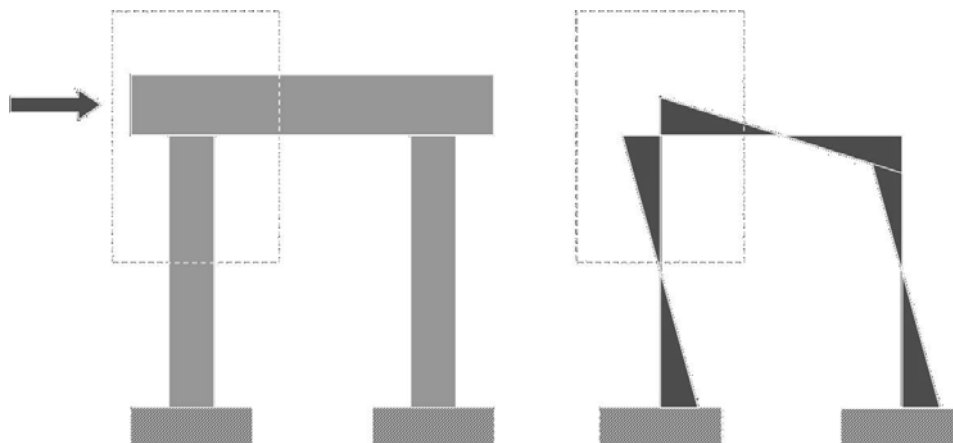


Figure 1.1: Schematic of two-column bent with moment diagram from seismic loading

Precast concrete connections can be particularly vulnerable to earthquakes. Unlike building design, which follows a strong-column-weak-beam philosophy, in typical bridge design the columns are designed to yield during an earthquake. This inelastic action is typically concentrated at the top and bottom of the columns. In CIP construction, this inelastic action tends to be spread over the column ends in a region known as the plastic hinge, shown in Figure 1.2. In precast construction, the precast elements are typically stronger and stiffer than the joints between them. Consequently, inelastic action tends to be concentrated at the joint, and the precast elements rotate as nearly rigid bodies.

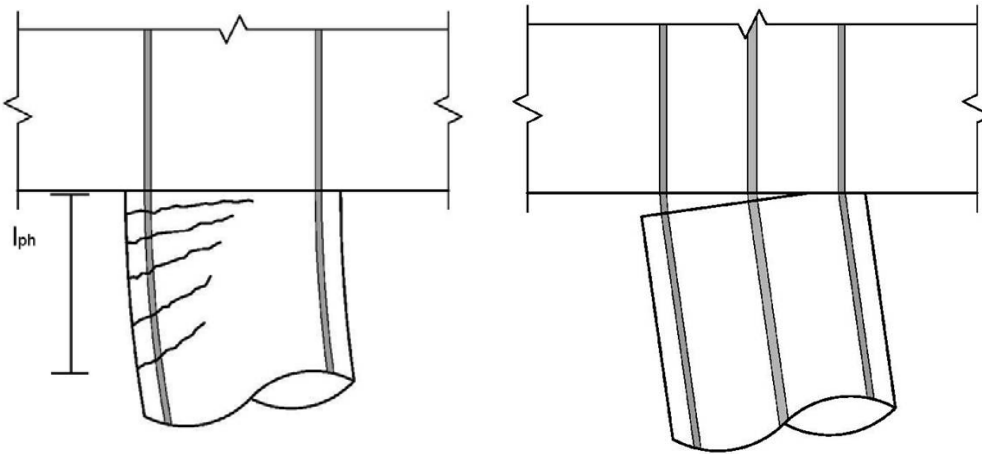


Figure 1.2: Comparison of reinforced concrete (left) and precast (right) column-to-cap beam joints

Two strategies have been proposed for designing precast joints at locations where high seismic moments can be expected. First, the designer may choose to reinforce the joint so that it is stronger than the surrounding precast elements and thus force the inelastic action to occur in the interior of the precast elements. This approach essentially emulates cast-in-place construction. This type of column is shown on the right in Figure 1.3. The figure also illustrates how the rotation at the joint increases with decreasing effective length. The reduced effective length of the column in turn increases the shear demand on the column and decreases ductility of the system.

Alternatively, the designer can ensure that the link between relatively rigid elements remains ductile during the earthquake. This strategy has been used in building design and tested in the PRESSS program (Nakaki 1999, Priestley 1999, Palmieri 1996).

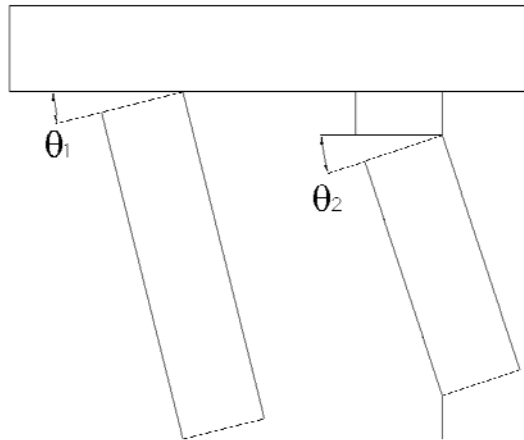


Figure 1.3: Displaced columns and rotations

The precast bridge substructure systems in Appendix A are intended to provide ductile connections between precast columns and cap beams. To meet the needs of WSDOT, the system must provide desirable seismic behavior, be quick to construct, and provide adequate construction tolerances.

1.2 PROPOSED PRECAST SUBSTRUCTURE SYSTEM

From many possible precast substructure systems, the “big bar” system shown in Figure 1.4 was selected for further research. The big bar system incorporates several large-diameter bars projecting from the top of a precast column into openings formed by metal ducts in the cap beam. In this system, the bars are then grouted into these openings. The advantages of this system include a cap beam design that is similar to cast-in-place (CIP) designs, larger construction tolerances than other duct-based systems, and a simplified construction procedure during which the cap beam can be placed on the column without a mating collar.

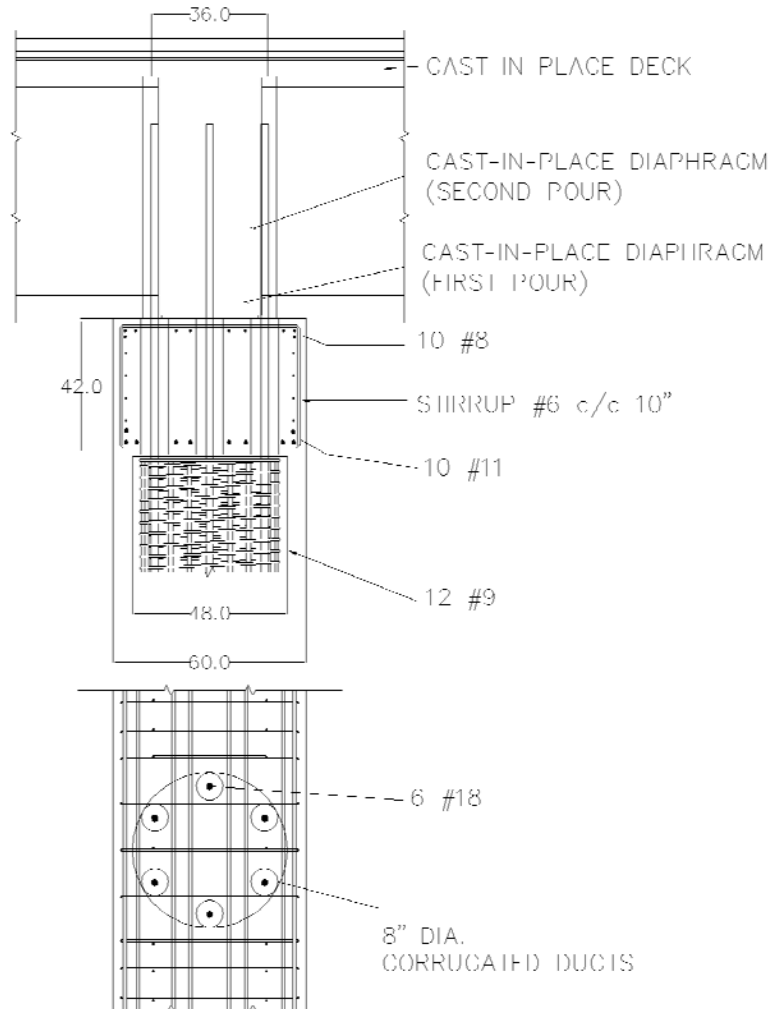


Figure 1.4: Big bar system

1.3 THE IMPORTANCE OF BOND TO THE PROPOSED SYSTEM

In the proposed system, the grouted large-diameter reinforcing bars carry tensile forces between the column and cap beam. To provide the full design strength of the reinforcing bars, the bars must be fully developed.

Two important loading combinations impose moments on the column-to-cap beam joint during the life of the bridge substructure that give rise to tensile stresses in the reinforcing bars. Seismic loading is probably the most critical of these loads. This joint is the yielding element in the structural system, and it is crucial to the performance of the structure that the bars yield before other failure mechanisms develop.

A second loading combination occurs during construction. During construction, loads are placed on the cap beam that impose moments in the columns. For example, girders may be placed on one span before they are placed on the next span. These moments are smaller in comparison to those imposed by seismic loads, but in this case, the diaphragm has not yet been constructed, so only the grouted duct is available to develop the bar.

The development of the bar is also linked to the strain concentration in precast joints. A bar developed into a CIP cap beam will pull out slightly from the cap beam, reducing the bar strain at the joint. In contrast, bars grouted into ducts provide excellent bond, in which case the bar strains in precast systems are concentrated over a very short length. There is then a risk of early bar fracture and, consequently, brittle behavior. Also, a bar that is developed in a very short length into the cap beam complicates the state of stress in the joint region (Sritharan 2005). One design intended to avoid a brittle joint includes intentionally debonding the large diameter bars to reduce the strain concentration at the joint.

In the absence of testing, the large-diameter bars must be continued to at least the code-required development length above the column, extending well beyond the cap beam and into the cast-in-place diaphragm. These requirements need to be reconsidered for this new application.

1.4 THE MECHANISM OF BOND

Some of the key relationships that govern the development of reinforcing bars are discussed here.

Bond stress (τ) is the first of these quantities. The bond stress is defined as the force along the bar axis per unit surface area transferred between the bar and the surrounding medium. Figure 1.5 and equations 0.1 to 0.6 show the equilibrium relationships between embedded length (L_e), bar perimeter (Π), bar stress (σ), and bond stress (τ).

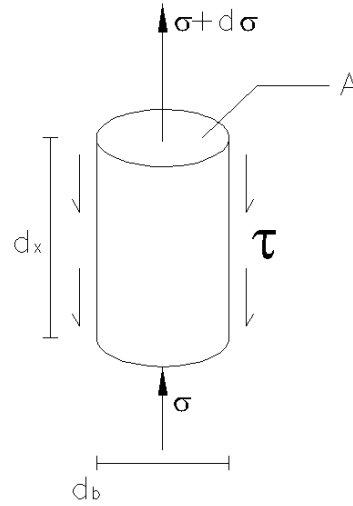


Figure 1.5: Equilibrium of pullout test

Equation 0.1 describes the equilibrium of forces on the differential element shown in Figure 1.5.

$$(\sigma + d\sigma) \cdot A - \sigma \cdot A = \tau \cdot \Pi \cdot dx \quad 0.1$$

Solving for the bond stress,

$$\tau = \frac{A}{\Pi} \frac{d\sigma}{dx} \quad 0.2$$

where A is the bar cross-sectional area.

By replacing the local bond stress, τ , with the average bond stress, τ_{avg} , this differential equation can be solved for the embedded length, l_e , to give following the linear equation:

$$\tau_{avg} = \frac{A}{\Pi} \frac{\sigma}{L_e} \quad 0.3$$

Equation 0.3 assumes that one end of the bar has no stress. A reinforcing bar is not a cylinder, but if we assume that $A = \frac{\pi}{4} d_b^2$ and $\Pi = \pi \cdot d_b$, then the average bond stress can be given by Equation 0.4,

$$\tau_{avg} = \frac{\sigma \cdot d_b}{4 \cdot L_e} \quad 0.4$$

which can be rearranged to give Equation 0.5,

$$\sigma = 4 \cdot \tau_{avg} \frac{L_e}{d_b} \quad 0.5$$

and Equation 0.6.

$$L_e = \frac{\sigma}{4 \cdot \tau_{avg}} d_b \quad 0.6$$

Equation 0.6 forms the basis for code development length equations, which incorporate a variety of factors that influence τ_{avg} . To fully develop a bar, the stress in the bar must reach f_y . In this case, the embedment length becomes the development length, l_d .

The local bond stress, τ , in Equation 0.2 at a point along a reinforcing bar under load is a function of the relative displacement between the bar and the surrounding medium. This constitutive relationship has been based on the shear strain, γ , in the medium surrounding the bar (Viathanatepa 1979). More recent research has related the local bond stress to the slip of the bar through the medium (Eligehausen 1983, Raynor 2000). Slip occurs along the bar-grout interface. The slip of the bar at the surface of the grout at the loaded end is termed the front-end slip. The slip at the bar at the opposite end of the embedded length is termed the back-end slip.

1.5 CODE DEVELOPMENT LENGTH EXPRESSIONS

Both the Association of State Highway and Transportation Officials (AASHTO) and American Concrete Institute (ACI) codes specify development lengths for bars embedded in concrete. These equations are based on the equilibrium principles in Equation 0.6. Neither code has addressed the development of bars grouted into ducts. By using the properties of the high-strength grout as the concrete strength, the code expressions result in development lengths that exceed the depth of the cap beam.

The ACI equation, with stresses in psi, is as follows:

$$l_d = \left(\frac{3}{40} \frac{f_y}{\sqrt{f'_c}} \frac{\psi_t \psi_e \psi_s \lambda}{\left(\frac{c_b + K_{tr}}{d_b} \right)} \right) d_b \quad 0.7$$

This equation results in $l_d = 45$ in. for a Grade 60 #18 bar embedded in 8000-psi grout with the maximum confinement term allowed, $\left(\frac{c_b + K_{tr}}{d_b}\right) = 2.5$. This value, given in Chapter 12 of ACI 318, is for non-seismic loading. For seismic loading, Chapter 21 of ACI 318 provides values only for bar sizes No. 3 through No. 11. For these bars embedded in 8000 psi concrete, the straight bar seismic development length is 34 bar diameters. This criterion would lead to $l_d = 75$ in. for a No 18 bar.

AASHTO gives separate equations for the development length, depending on the bar size. Stresses are in ksi for all AASHTO expressions. Bars smaller than #14 are governed by Equation 0.8.

$$l_d = \frac{1.25A_b f_y}{\sqrt{f'_c}} \quad 0.8$$

Equation 0.9 governs #14 bars.

$$l_d = \frac{2.7 f_y}{\sqrt{f'_c}} \quad 0.9$$

Equation 0.10 governs #18 bars.

$$l_d = \frac{3.5 f_y}{\sqrt{f'_c}} \quad 0.10$$

For a Grade 60 #18 in 8-ksi concrete, the non-seismic AASHTO development length is 74 inches. The seismic development length is 125 percent of the nonseismic length, or 93 inches. These equations are intended for use with bars embedded in concrete alone. However, previous research, discussed below, suggests that bars grouted into ducts are developed much more quickly than bars cast into concrete.

1.6 PREVIOUS RESEARCH

Although there has been a substantial amount of research into the development of reinforcing bars in normal-weight concrete, much less research has been performed on bars grouted into ducts. Research at the University of Washington (Raynor 2000) showed that small-diameter bars grouted into ducts develop very high bond stresses and can be developed to fracture in six to eight bar diameters. This research was primarily

conducted on #8 bars, with three tests on #10 bars. Raynor's development length equation for monotonic loading is shown in Equation 0.11.

$$\frac{l_d}{d_b} = \frac{0.5\sigma_u}{f'_g} \quad 0.11$$

where σ_u is the ultimate steel stress and f'_g is the grout compressive strength.

Other research has indicated that duct pullout through the concrete matrix can be an important failure mechanism (Palmeri 1996, Brenes 2006). This research was conducted with relatively large bars in smaller ducts. Because of the large diameter of the duct required to maintain the desired construction tolerances, duct pullout is less likely to be a factor.

The duct will pull through the concrete when the applied load exceeds the bond capacity between the concrete and duct. This mechanism will not control when the bar capacity is less than the duct capacity (Equation 0.12).

$$P_{duct} \geq P_{bar} \quad 0.12$$

These capacities are functions of the diameter of the bar and duct, shown in Equation 0.13.

$$\tau_{duct} \cdot l_e \cdot \pi \cdot d_{duct} \geq \tau_{bar} \cdot l_e \cdot \pi \cdot d_{bar} \quad 0.13$$

As the bar-to-duct diameter ratio decreases with increasing duct size, less demand is placed on the duct-concrete bond. As long as the inequality in Equation 0.14 is satisfied, the bar will pull out through the grout before the duct pulls out through the concrete.

$$\frac{\tau_{duct}}{\tau_{bar}} \geq \frac{d_{bar}}{d_{duct}} \quad 0.14$$

1.7 RESEARCH PROGRAM

This research developed a novel combination of materials and applications to develop large-diameter bars in the “big bar” precast bridge rapid construction system. Bond relationships and development lengths for these bars grouted into ducts were developed. The range of bar sizes tested by Raynor was extended to the largest bars available. The bars were tested in a configuration similar to that in the intended application.

This research also supports ongoing testing of the “big bar” column and cap beam system. Because the joint cannot be tested at full scale with current lab conditions, scaled tests of the column-to-cap beam joint are being conducted. Pullout tests of the full-scale and scaled bars were conducted to validate the use of scaled materials in the pseudostatic column-to-cap beam joint tests.

1.8 ORGANIZATION OF REPORT

Chapter 2 describes the pullout tests performed for the experimental program. Chapter 3 presents the results of material testing associated with the experimental program. Chapter 4 presents the results of the pullout tests. Chapter 5 discusses findings from these results. Chapter 6 describes analytical modeling performed in support of the pullout tests, and Chapter 7 presents a summary and conclusions.

CHAPTER 2: EXPERIMENTAL PROGRAM

This chapter describes the experimental program, which consisted of a series of 17 monotonic pullout tests of reinforcing bars anchored in grout and concrete. All but one of these tests were performed on bars grouted in steel ducts, which were cast into blocks of concrete. The remaining test was performed on a bar cast directly into the concrete.

2.1 OVERVIEW OF TESTING

The tests conducted in this study were designed to determine the influence of the following parameters:

- embedment length
- bar diameter
- fiber-reinforcement of the grout
- scaling.

Table 2.1 below shows the test matrix. Each test was denoted by a five-digit code to indicate the bar size, type of test, and embedment length. Its form was xxAyy, where xx represents the bar size, A represents an alphabetic code shown below, and yy represents the nominal embedment length in bar diameters. Tests are broken down into two groups: full-scale tests and scaled tests. Full-scale tests were conducted in the large-diameter steel ducts called for in the proposed substructure system, while the scaled tests were conducted in smaller ducts that were used in the scaled column tests.

Table 2.1: Test matrix

		Bar size			
		Full-scale tests			Scaled tests
		#18	#14	#10	#8
Embedment length	2 d _b	18N02, 18F02			
	3 d _b	18N03, 18F03			
	4 d _b	18N04, 18F04, 18S04		10N04, 10F04	
	6 d _b	18N06		10N06	
	8 d _b	18N08	14N08	10N08	08N08, 08C08
	14 d _b	18N14			

N = non-fiber reinforced grout

F = fiber reinforced grout

S = surface test (no fibers)

C = concrete embedment

Monotonic testing was selected over cyclic testing. In research conducted on bars embedded in concrete, monotonic tests have been found to provide a useful approximation of the envelope curve of cyclic tests (Eligehausen 1983). In addition, cyclic tests of these large bars would also have been difficult because of the large forces applied, which require both high-capacity and complex connections between the actuators and test specimen. The loading connections for a cyclic test must accommodate some tolerances in the location and angle of the grouted bar and carry large loads between the actuator and test specimen.

The test sequence began with the shortest embedment length tests and progressed to greater lengths in order to find the embedment length necessary to yield or fracture a bar. Initially, tests were performed both with fibers and without fibers at the same development lengths, but the fiber tests were dropped from later testing when the fibers were shown to have little beneficial effect.

For the majority of the tests, the duct was continuously cast into the concrete beyond the grouted region, virtually eliminating the possibility of the duct slipping through the concrete. A continuous duct also allowed for much greater flexibility in conducting the tests because several tests were conducted in each duct. Each test used a fresh region of the duct. In the remaining tests (18S04, 18N14, and 08N08), the bar was embedded in a separate section of duct. A spacer separated the back end of the duct from the rest of the specimen, and the grout filled the full duct length.

It would have been impractical to test the column-cap beam connections at full scale. The joint tests were conducted at a scale factor of 2.4. Scaled ducts and bars were used in the seismic joint tests. In support of the joint tests, two pullout tests, 08N08 and 08C08, were performed to ensure that scaling the bars and ducts was appropriate. These tests also provide a more direct comparison with Raynor's work because of the matching bar size, although the duct-to-bar diameter ratio was larger for these tests.

2.2 SPECIMEN DESIGN

The seventeen pullout tests were conducted in five concrete specimens. The tests performed in each specimen are shown schematically in Figure 2.1. The test specimens were designed to allow a relatively large number and variety of tests. This resulted in successive tests located in the same specimen being conducted directly above each other, approaching the top of the specimen in later tests.

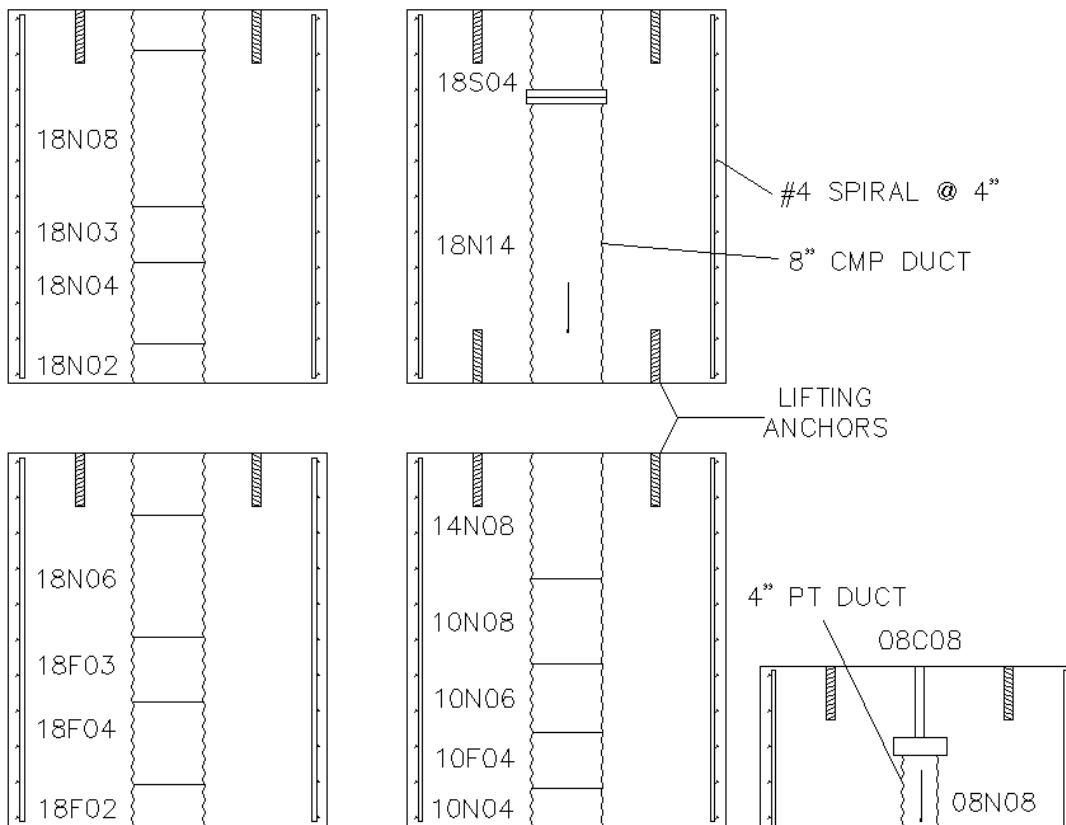


Figure 2.1: Tests performed in each specimen

For the full-scale bar tests, four large concrete cylinders (36 in. diameter by 42 in. tall) were cast, each with a single 8-in.-diameter duct along the axis. Three of the specimens had continuous ducts while the fourth had a plywood spacer to separate the duct for two tests (18S04 and 18N14). Unlike the other specimens, this specimen was designed to be inverted to allow tests to be conducted from each end. The specimens were reinforced lightly with #4 spiral spaced at 4 in. on center and six #3 vertical bars to support the spiral.

The scaled (#8) bar tests were performed in a fifth, shorter cylinder (36 in. diameter by 18 in. tall). The matching cylinder diameter allowed the same loading equipment to be used in all the tests. This cylinder was also designed to be inverted between the two tests. The specimen was cast with a #8 bar embedded 8 in. in concrete for test 08C08 and with an 8-in. length of 4-in.-diameter duct for test 08N08.

Each test specimen included two recessed Dayton Superior B-16 lifting anchors on the top surface. The two specimens that were designed to be inverted had lifting anchors on both ends of the cylinder. In addition to providing a means to move the specimens about the lab, these anchors were used to attach instrumentation to measure displacement of the concrete and bar.

2.3 MATERIALS

2.3.1 Concrete

The concrete used in the construction of the test specimens and test apparatus had a target strength of 6000 psi. Because of the expected overstrength of delivered concrete, a 5000-psi mix was ordered. Because the concrete was not typically damaged during testing, concrete cylinders were tested intermittently.

2.3.2 Ducts

Previous research on grouted bars has been conducted in unlined holes (Darwin 1993) or on bars grouted into post-tensioning (PT) ducts (Raynor 2000). PT duct is available up to an outer diameter of 6 in. This diameter is insufficient to accommodate the 2.25-in. nominal diameter #18 bar and the desired construction tolerances (+/- 3 in.). For the tests on #10, #14, and #18 bars, the duct cast into the concrete test specimen was

an 8-in. nominal diameter corrugated steel pipe. These galvanized pipes are available in diameters from 6 in. to 12 ft.

The corrugated metal pipes (CMP) are fabricated from a long piece of galvanized steel, which is then helically wound to the required diameter. These ducts have the advantage of having large surface deformations, which increase the resistance to shear between the duct and its surrounding medium. Furthermore, the increased thickness of the pipe in comparison to the PT duct increases the confinement of the grout, potentially strengthening the grout and preventing radial bond cracks from propagating to the surrounding concrete.

For the scaled-down pullout test (08N08), 4-in.-diameter PT duct created the void into which the bar was grouted because 4-in. CMP was not available. The same PT duct was used in the scaled column-cap beam joint connections tested for the project. Scaled comparisons are shown in Table 2.2.

Table 2.2: Duct dimensions (all dimensions inches)

Duct	Outer diameter	Inner diameter	Thickness	Wavelength	Deformation height
8 in. CMP	8.81	8.19	0.068	1.59	0.25
Scaled CMP	3.67	3.41	0.028	0.66	0.10
4 inch PT	3.94	3.19	0.023	0.53	0.16

2.3.3 Reinforcing Bars

The bars used in these pullout tests were all A706 Grade 60 with bamboo-style deformations, seen in Figure 2.2. Each bar was used for more than one test as long as the bar remained elastic during the initial tests. For subsequent tests, the embedded section of the bar was cut off to eliminate contamination from previous grout and to facilitate the construction of the test stack. Two #8, two #10, one #14, and four #18 bars were used during the tests.

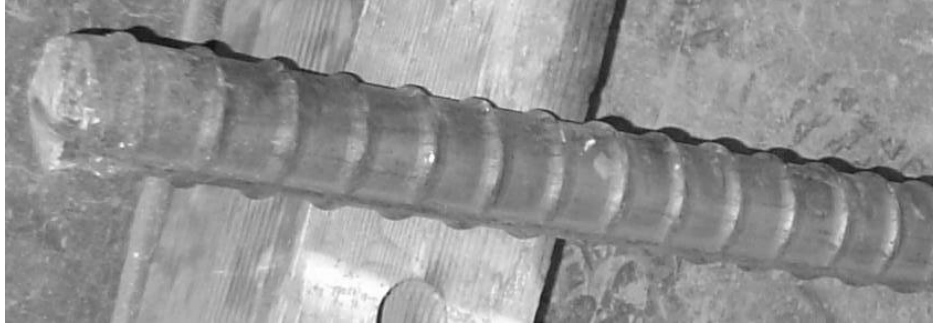


Figure 2.2: Bamboo ribs on a #18 bar

Because of the high tensile capacity of the #18 bars, no separate stress-strain tests to failure were performed, although the pullout tests themselves provided stress-strain data. Stress-strain curves are reported in Chapter 3. Key bar geometric properties, including relative reinforcement ratios, for each bar are also reported in Chapter 3.

2.3.4 Grout

The grout used in the pullout tests was Dayton Superior Sure-Grip High Performance Grout. The grout was mixed according to the manufacturer's instructions to provide a "fluid" mix. The grout was proportioned by converting the manufacturer's volumetric instructions to a weight ratio of 0.15 lb of water per pound of grout. Total weights were determined by calculating the desired grout volume, including allowances for test cubes and waste, and finding the weight of grout required. One bag of grout weighed about 50 lb and produced about 0.5 ft³ of grout.

Mixing was performed with a handheld electric drill in a bucket. Approximately 2/3 of the water was placed in the bucket. Grout was slowly added and mixed, with water being added intermittently to maintain a fluid mix. When all the water and grout were in the bucket, mixing continued until the grout was smooth and even.

Grout strengths were determined by cube testing per ASTM C109. The 2-in. cube samples were cast from each batch after the grout was mixed. The cubes were demolded after 24 hours of curing under plastic and were placed in a fog room until tested. Each cube was measured with calipers before testing, and the area calculated from these measurements was used to determine the strength at the peak load.

Before the pullout specimens were grouted, four series of grout tests were performed. Grout strengths for the preliminary mixes are reported in Figure 2.3. These

tests determined the desirable mix and test age for the grout. The first two batches were prepared according to the manufacturer’s instructions for “fluid” and “flowable” mixes. Despite containing less water, the flowable mix achieved lower early strengths, so the fluid mix was selected for all further testing. Next, two more fluid mixes were tested at three, four, five, seven, and nine days to determine an appropriate age for testing. With many tests run in each specimen, the grout curing time was a significant factor in the overall test-to-test cycle time. These tests indicated that the strength of a mix remained stable after five days. A further increase in strength was within the scatter of the data. From these preliminary tests, the researchers decided to test each specimen at five days, when grout strengths were approximately 8000 psi.

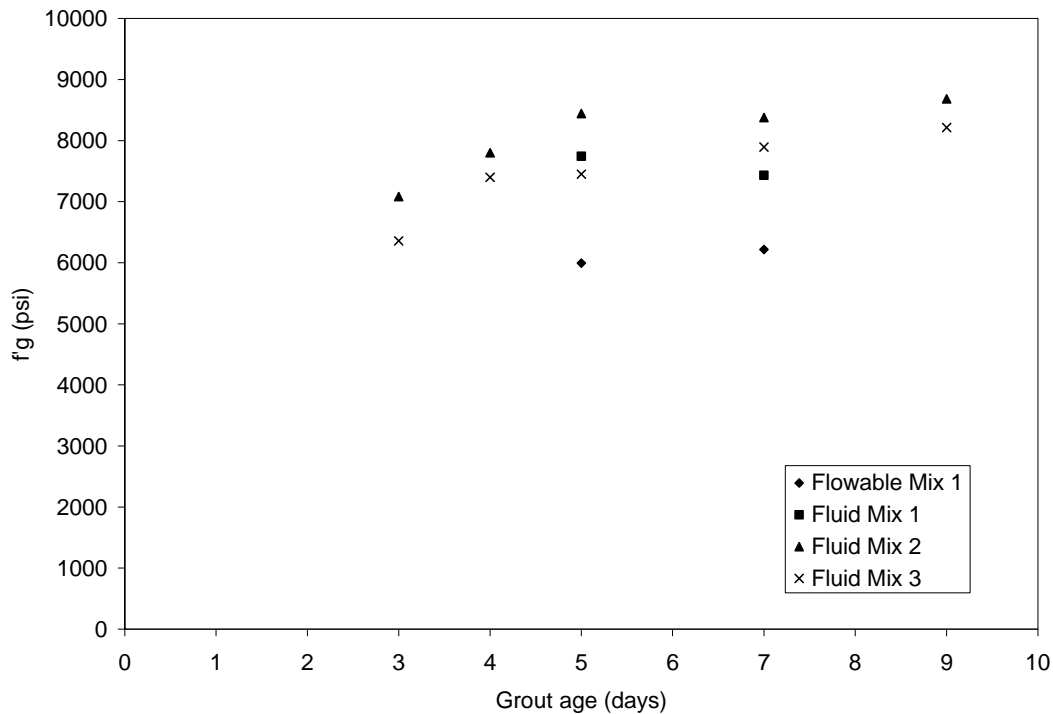


Figure 2.3: Preliminary grout strengths

2.3.5 Fibers

The fiber reinforcement used in the “F” series of tests was Fibermesh 150 polypropylene fiber. The fibers were dosed at 3 lb/yd³ to replicate the materials used in previous research at the University of Washington (UW), although this is twice the

manufacturer's recommended dose (Raynor 2000). The fibers were added to the mixing bucket after the grout had been mixed to an even consistency. Mixing continued until the fibers were evenly distributed.

2.4 TEST BAR GROUTING PROCEDURE

The first step in preparing the test specimen was to grout the bar into the duct for the appropriate length. Appropriate quantities of grout and water were proportioned by weight and mixed. If required, fibers were also proportioned by weight and added to the mix. The grout was placed in the specimen by means of a PVC tremie pipe. The depth of the grout was monitored by means of a dipstick. Depending on the location and length of the grouted region, various methods were used to ensure that the embedded bar was centered and plumb. Typically, this was accomplished by centering the bottom of the bar in a divot in the center of the duct before the grouting operation began and by centering the bar at the surface of the specimen with a wooden crosshead attached to the lifting anchors. A level was always used to establish that the bar was vertical.

2.5 LOADING APPARATUS

The pullout tests were conducted by using the self-reacting test setup shown in Figure 2.4. The test stack consisted of a specimen with its grouted bar, a concrete reaction block, a ram, a load cell, and a bar grip.

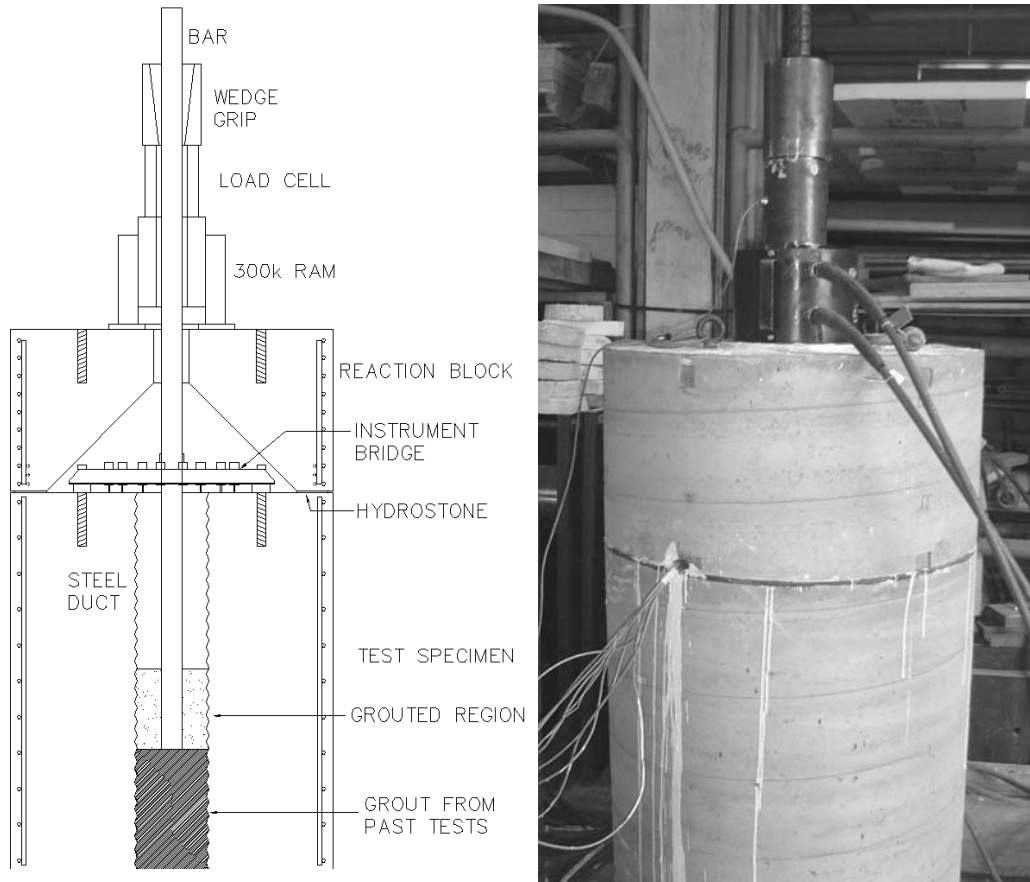


Figure 2.4: Test setup

2.5.1 Reaction Block

Immediately above the test specimen, a concrete reaction block filled two roles. First, it spread the load applied by the ram from a small area to a larger annulus on the test specimen, as shown in Figure 2.5. Second, it created a space for instrumentation to be placed on the concrete surface and bar to measure displacements and strains during the course of the test. This void was roughly conical, with a center hole to allow the bar to pass through the top of the block. An opening was provided at the base for instrumentation wires to pass from this central void to the data acquisition system.

The reaction block, shown in Figure 2.6, was designed by using strut-and-tie concepts for a capacity of 300 kips. It performed well in tests of up to 420 kips without substantial cracking. Reinforcement consisted of both #4 spiral and 1/2-inch prestressing strand. An annular steel plate was permanently attached with hydrostone to the top surface of the reaction block to provide a smooth surface for the ram to sit on.

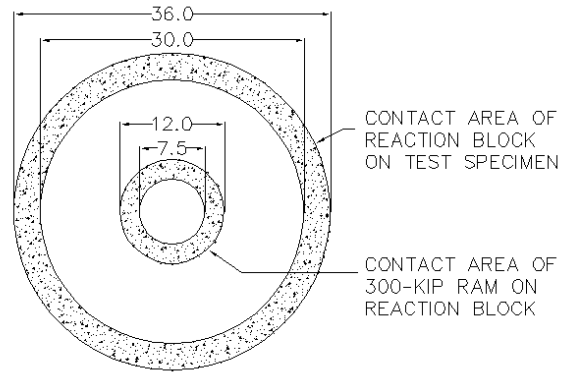


Figure 2.5: Annuli of contact for ram and reaction block

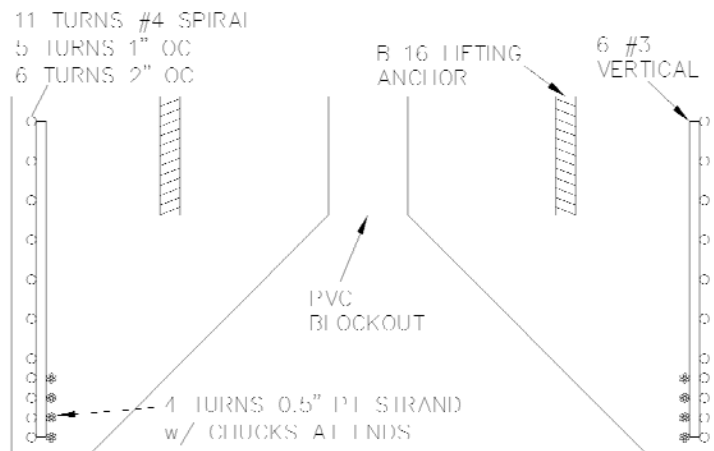


Figure 2.6: Reaction block design

The large diameter of the concrete specimens allowed the load to be applied by reacting against the top surface of the specimen without providing excessive restraint near the duct. The free surface on the top of the specimen also allowed the instrumentation to be placed on the top surface of the concrete.

2.5.2 Rams

Loading for the tests was provided by one of two ram setups. For the majority of the tests, a 300-kip, low-profile, double-acting center-hole ram applied the load. The ram was capable of yielding, but not fracturing, a #18 bar. A 600-kip capacity ram was used for the longer embedment length tests of the #18 bars (18N06, 18N08, 18N14) in order to apply the loads needed to fracture a #18 bar. The 600-kip ram assembly, shown in Figure 2.7, was composed of three 200-kip rams acting together. A hydraulic manifold allowed simultaneous, equal loading of the three rams. Steel plates on each face and a sliding center-hole assembly kept the load centered and plane. Hydraulic pressure for both ram setups was provided by an electric pump.



Figure 2.7: Triple ram used to yield and fracture #18 bars

2.5.3 Load Cell

Between the rams and the grips, a center hole load cell was placed in series to measure the applied load. The load cell is further discussed in the instrumentation section below.

2.5.4 Grips

To transfer the load from the stack to the bar, a custom-made grip topped the test stack. The grip was patterned after wedges that had been used in smaller (#6 and #8) reinforcing bar tests, which had been scaled up from a prestressing strand chuck. The grip consisted of a large steel collar mated with three hardened wedges. The same collar

was used for the #10, #14, and #18 bar tests, with different wedges for each diameter bar. For the #8 tests, the wedges and collar from previous UW testing were used. Although most dimensions for the larger collar and wedges were scaled directly from the #8 grip, the overall height of the collar and wedges was increased by 50 percent to reduce the stresses on the sliding surface. The dimensions of the large collar and wedges are shown in Figure 2.8. During one test on a #18 bar, one wedge cracked lengthwise. The crack initiated on the face with the threads and propagated radially to the angled surface. This crack was analogous to the splits between the wedges and did not affect the performance of the grip.

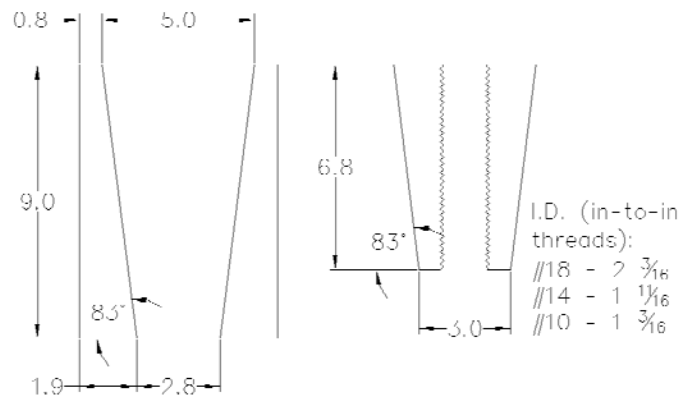


Figure 2.8: Wedge grip design (dimensions in inches)

2.6 INSTRUMENTATION

Load, strain, and displacement data were collected to characterize the response of the specimen.

2.6.1 Load Cell

For the #10, #14, and #18 bar tests, a 300-kip load cell was part of the test stack. Like the collar block, the load cell was originally designed for 300 kips but performed well up to the 420-kip maximum load applied during the test series. For the #8 bar tests, a 200-kip load cell was used. Both load cells were calibrated against the laboratory's 300-kip Baldwin testing machine before testing with the data acquisition system used for the test.

2.6.2 Linear Potentiometers

During each test, an array of linear potentiometers (pots) measured the displacements of the concrete surface, bar, and either the grout surface or duct. The layout of pots on the bridge is shown schematically in Figure 2.9, and with a photo in Figure 2.10. The pots had a nominal stroke of 1.5 in. and generally provided good data for about 1.3 in. For all tests, an aluminum bridge provided the mounting surface for the pots. This bridge was anchored to the test specimen with the lifting anchors. Four pots measured concrete displacements 5.5 in. and 7 in. from the axis of the bar. Two pots measured grout or duct displacements, and two measured bar displacements. The pots labeled “Duct” in Figure 2.9 measured duct displacements for most tests. These pots measured grout displacements on the tests that were conducted at the top surface of the specimen.

The pots measuring the concrete and grout displacements were glued to the aluminum bridge and touched glass slides attached to the rougher concrete or grout surface. For duct and bar measurements, the nose of the pot touched aluminum angles attached to the duct or bar. One limitation of this method of attachment was that in later tests, the mill scale flaked off the bar as the bar yielded. The aluminum angles then detached from the bar, and measurements became undependable.

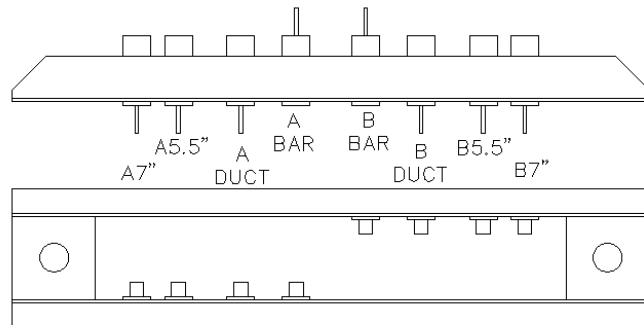


Figure 2.9: Schematic of instrumentation bridge with pots

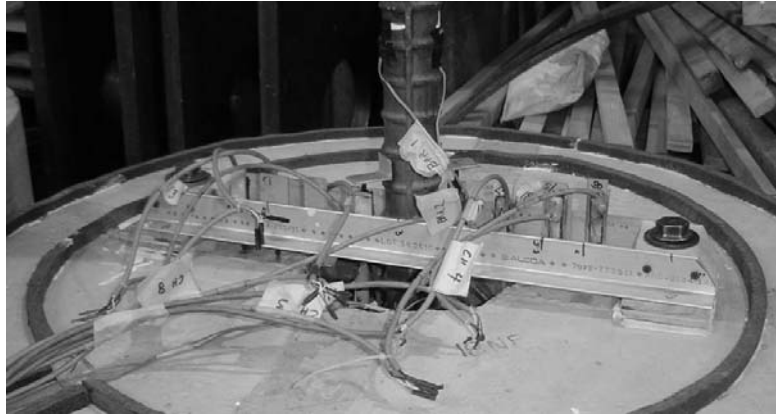


Figure 2.10: Photo of pots for test 18N02

For one test, 18N08, an additional potentiometer measured the movement of the back end (bottom) of the bar. For most tests, this surface was inaccessible because of the hydrostone poured into the duct that filled the damaged grout from previous tests. For test 18N08, this hydrostone was drilled out to provide access to the back end of the bar. The pot was anchored to a PVC pipe, which was in turn anchored to the bottom face of the test specimen.

2.6.3 Strain Gages

For each test, two strain gages were attached to the bar above the grout surface, immediately above the attachment for the bar potentiometers. The gages used were type FLA-5-11 from TML. The strain data from these “in air” gages were useful in several respects, including measuring the strain demand at the grout surface, providing data for stress-strain curves for each bar, and allowing the displacement of the bar at the grout surface to be calculated, as discussed in Chapter 3.

For test 18N14, substantially more gages were installed. In addition to the “in air” gages used in each test, gages were placed on the test bar at several depths in the grout to measure the strain penetration and to provide data on the distribution of bond stresses. Gages were also placed on the confining #4 spiral in the concrete, and strain gage rosettes were placed on the confining duct. The rosettes used were FRA-5-11. Although standard procedures to waterproof and protect these gages were utilized, the data from the gages embedded in concrete or grout were generally poor.

2.7 TEST PROCEDURE

Because the bars and specimens were used for several tests in a series, the test procedure included a period of setup, the actual test, and resetting for the next test.

2.7.1 Setup

After the grout had set, the centering crosshead could be removed and the specimen prepared for testing. First, the instrumentation bridge shown in Figure 2.10 was bolted into the recessed lifting anchors. After the instrumentation was in place, the concrete reaction block was placed on top of the specimen. Contact between the two concrete blocks was ensured by placing a layer of hydrostone on the annulus of contact. The lab's overhead crane facilitated the accurate placement of the reaction block and the test stack above it.

The remainder of the test stack (rams, load cell, and stressing collar) was then placed and centered on the bar. The final step was to place the wedges into the stressing collar. After this was completed, the test itself was ready to be run.

2.7.2 Pullout Test

After it had been confirmed that the electronic data acquisition system was running and recording data, pressure was applied to the ram or rams by means of an electric pump. The loading rate, determined by modulating the running of the pump, was approximately 0.1 in./min in the elastic range. After the bar yielded, the pump was run constantly, and the flow capacity determined the loading rate.

Each test consisted of two phases. In the first phase, the bar was loaded to 5 ksi and then unloaded. This procedure allowed the grips to set and confirmed that the pump and data acquisition electronics were functioning properly. After unloading, the second phase of the test involved running the pump as above until either the bar unloaded or the stroke of the ram was reached. In the latter case, the ram was unloaded, steel shims were placed between the load cell and the grips, and the ram was reloaded. Tests on bars embedded in concrete have shown that this unload/reload cycle does not significantly affect the envelope behavior (Eligehausen 1983). During some tests, this unload/reload cycle had to be carried out two or three times to provide enough stroke to pull out the bar.

2.7.3 Post-Test Reset

After each test, the grips were removed from the bar. This procedure was sometimes difficult because the high loads gripping the bar squeezed the wedges and collar block together. To loosen the collar from the wedges, an annular steel cylinder was placed over the collar and hit with a sledgehammer. On one occasion, the collar was also heated to separate the collar and wedges. After the wedges had been removed, the test stack could be removed in reverse order (load cell, rams, reaction block). At this point, the damage to the bar, grout, and concrete could be observed.

The test procedure consistently loosened the bar to the point where it could be removed from the damaged grout by hand or with the overhead crane. For tests in which the bar remained elastic, the bar was then prepared for further testing by cutting off the section of the bar that had been embedded in the grout. This eliminated the need to clean the grout off the embedded section bar and also kept the overall height of the fully prepared test specimen roughly constant. This meant that the “in air” strain gages could be reused if they were undamaged.

The concrete cylinders were used for several tests. Loose grout was removed from the duct, and a smooth, level surface was created by pouring hydrostone into the duct. As a result of this procedure, early tests in each specimen were deeper than the later ones, which occurred closer to the surface. Although this changed the stress conditions in the concrete outside the ducts, the performance of the concrete was rarely critical to the result of the test.

CHAPTER 3: RESULTS OF MATERIAL TESTS

This chapter presents the results of the pullout tests and supplementary material testing. Section 3.1 describes the geometry of the reinforcing bars used in the pullout tests, Section 3.2 describes the stress-strain relationships of the reinforcing bars, Section 3.3 reports grout strengths, and Section 3.4 reports concrete strengths.

3.1 REINFORCING BAR GEOMETRY

This section describes the geometric properties of the reinforcing bars. The area, diameter, and relative rib area of each bar are listed in Table 3.1.

Table 3.1: Bar dimensions

Tests	Nominal diameter	Lug diameter	Nominal area	Average area	Net area	Relative rib area
	d_b	d_l	A_{nom}	A_{avg}	A_{net}	R_r
	(in.)	(in.)	(in. ²)	(in. ²)	(in. ²)	(--)
08C08 08N08	1	1.08	0.79	0.75	0.72	0.081
10N04 10F04 10N06	1.27	1.38	1.27	1.21	1.15	0.077
10N08	1.27	1.35	1.27	1.23	1.17	0.067
14N08	1.69	1.80	2.25	2.19	2.11	0.056
18N02 18N03 18N04 18N08	2.26	2.37	4.00	3.74	3.67	0.063
18F02 18F03 18F04 18N06	2.26	2.41	4.00	3.75	3.66	0.078
18N14	2.26	2.38	4.00	3.91	3.77	0.063
18S04	2.26	2.39	4.00	3.75	3.62	0.074

The nominal values of the bar area and diameter, defined by the American Concrete Institute and the ASTM International, are the basis for design calculations. Unless otherwise noted, these nominal quantities were used for all calculations. The nominal area is based on the nominal weight per unit length of the bar. The cross-

sectional area of an equivalent smooth cylinder is calculated by dividing this nominal weight by an assumed density of steel.

$$A_{nom} = \frac{w_{nom} / ft}{490 \frac{lb}{ft^3}} \left(\frac{12in}{1ft} \right)^2 \quad 3.1$$

The nominal diameter of the bar is the diameter of the equivalent cylinder.

$$d_b = \frac{4}{\pi} \sqrt{A_{nom}} \quad 3.2$$

The actual average bar area was calculated by using the actual weight of a length of the bar and Equation 3.3.

$$A_{avg} = \frac{W_{actual}}{L_{bar} \cdot 490 \frac{lb}{ft^3}} \left(\frac{12in}{1ft} \right)^2 \quad 3.3$$

On average, the average area was 95.4 percent of the nominal area, ranging from 93.8 percent to 97.7 percent of the nominal value. ASTM Specification A706 specifies that this area be at least 94 percent of the nominal area. Two bars just failed this criterion.

The net area is the minimum area available for carrying longitudinal stresses: the body of the bar and the longitudinal ribs. Figure 3.1 shows the locations of the measurements of each bar. Two measurements, a and b, were taken of the diameter of the body of the bar. The height and width of the longitudinal ribs, h_r and w_r , respectively, were also measured.

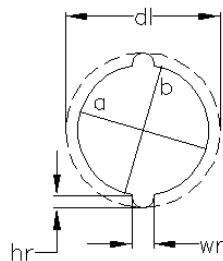


Figure 3.1: Bar dimensions for net area calculations

The net area was calculated as follows:

$$A_{net} = \pi \cdot a \cdot b + 2 \cdot w_r \cdot h_r \quad 3.4$$

The net area of each bar ranged from 90.5 percent to 94.2 percent of the nominal area, with the average being 92.0 percent of the nominal area.

The perimeter of the circle described by the transverse lugs was used for some bond calculations. This perimeter is defined by a diameter, d_l , which includes the body of the bar and the lugs. The average bond stresses calculated with this perimeter are denoted by the subscript *cyl*.

Relative rib area is a quantity that relates the bearing area of the transverse ribs to the shearing area along the surface of the bar (see Figure 3.2). The area of a rib is given as follows (ACI 408.3 2001).

$$A_r = (\pi d_b - 2w_r)h_r \quad 3.5$$

The relative rib area is then:

$$R_r = \frac{A_r}{\pi d_b s_r} \quad 3.6$$

Bars with relative rib areas of greater than 0.1 are allowed by ACI to have shorter development lengths than other bars (ACI 408.3 2001). The relative rib areas of the bars used in this study did not exceed this value and ranged from 0.056 to 0.081.

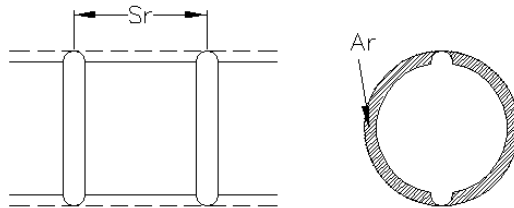


Figure 3.2: Bar dimensions for relative rib area

3.2 REINFORCING BAR STRESS-STRAIN DATA

Each pullout test provided stress-strain data from the load cell and the strain gages. Most bars were loaded in the elastic range for more than one test. Comparing the stress-strain curves for each test confirmed the accuracy of the data.

Each of the three bar areas was used to calculate the stress on the bar and stress-derived quantities such as the yield strength, f_y , and the elastic modulus, E . The yield strength was calculated by using the 0.2 percent offset method. E was calculated in the linear range of the steel. Table 3.2 shows the values of f_y and E determined for each bar from each area.

Table 3.2: Yield stresses and elastic moduli

Tests	Nominal area		Average area		Net area	
	f_y	E	f_y	E	f_y	E
	(ksi)	(ksi)	(ksi)	(ksi)	(ksi)	(ksi)
08C08 08N08	62.5	23120	66.0	24370	68.7	25360
10F04 10N04 10N06	61.1	22790	64.0	24710	67.4	25960
10N08	62.0	23950	64.1	24300	67.6	25200
14N08	65.8	24990	67.7	25760	70.2	26890
18N02 18N03 18N04 18N08	65.6	24600	70.4	26620	71.6	27110
18F02 18F03 18F04 18N06	69.3	27430	74.0	29022	71.7	29750
18N14	69.3	26550	70.8	27050	73.4	27950
18S04	¹	25730	¹	27230	¹	27940

¹ Note: Bar used for test 18S04 did not yield

A net area stress-strain curve is shown in Figure 3.3, and plots for each bar are shown in Appendix B. The net stresses provided the best agreement with the expected value of Young's modulus because the strain measurements were taken at a point between lugs, where only the net area was available to resist longitudinal stress.

However, even more steel was removed to place the gages, further decreasing the stiffness of the bar at the location where the strains are measured. This effect was more pronounced for the smaller bars, where the steel removed for the gage was a larger percentage of the overall bar area.

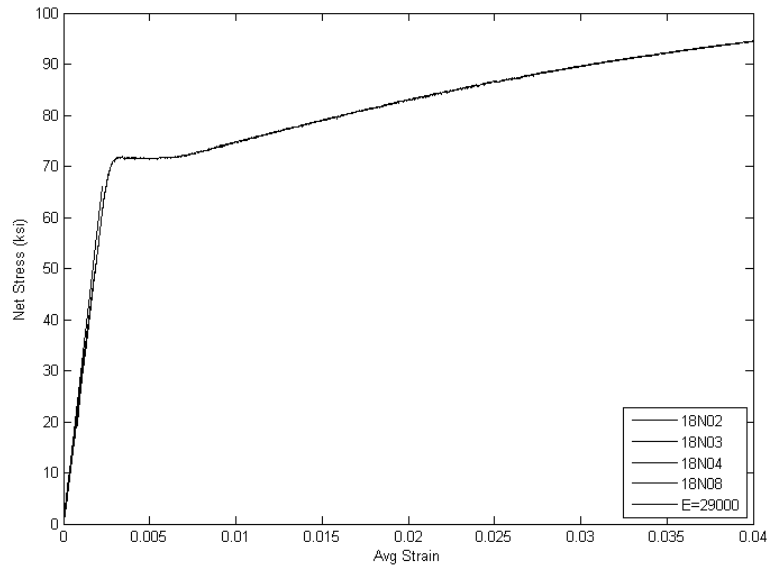


Figure 3.3: Net stress-strain curve

3.3 GROUT STRENGTHS

Grout strength gain with time is shown in Figure 3.4. Grout cubes were tested on the day of each pullout test and at seven days after mixing. In addition, several mixes were tested at ages of eight to 61 days to measure long-term strength gain. The grout strength on each test day is shown in Table 3.3 and was typically 7500 psi to 8500 psi. Cubes tested after 28 days had an average compressive strength of 10,000 psi.

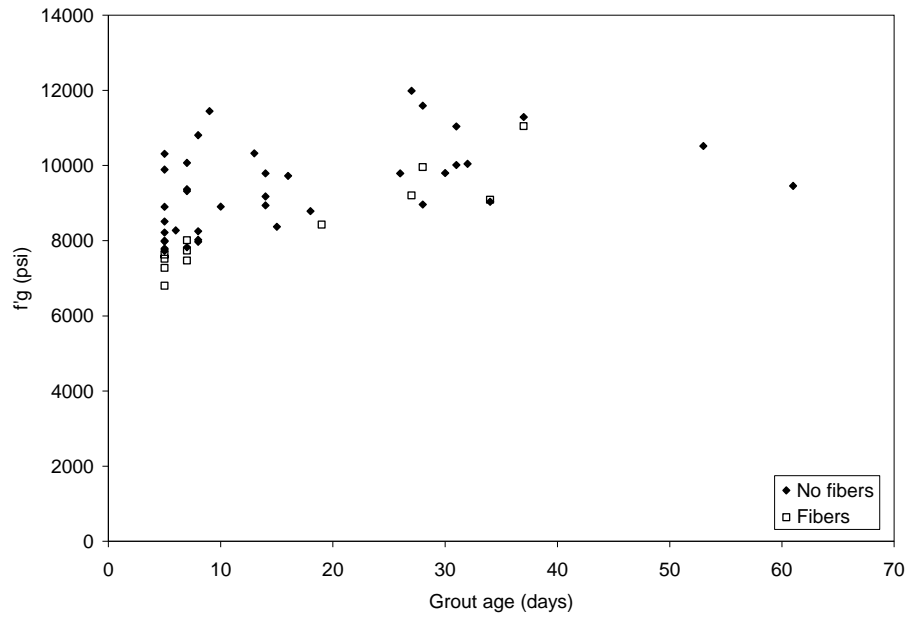


Figure 3.4: Test mix grout strengths

Table 3.3: Test day grout strengths

Test	Grout age	f'_g
	(day)	(ksi)
08C08	46 ¹	8.07 ¹
08N08	5	7.79
10F04	5	7.63
10N04	5	7.98
10N06	6	8.27
10N08	5	8.00
14N08	5	8.22
18F02	5	7.27
18F03	5	7.52
18F04	5	6.80
18N02	15	8.37
18N03	5	7.77
18N04	5	8.51
18N06	5	9.89
18N08	5	8.90
18N14	5	10.31
18S04	5	7.98

¹ No grouted duct, concrete age and f'_c shown

The presence of fibers reduced the grout cube compressive strength. The average test day unreinforced grout strength was 8.5 ksi, whereas the average test day fiber-reinforced grout strength was 7.3 ksi. The fiber-reinforced grout was mixed with the same water/grout ratio but resulted in reduced early strengths. The grout cubes failed through spalling of the side surfaces, with the remaining core area crushing. By displacing grout, the fibers create an overall weaker cube. Because the fibers were randomly oriented, for every fiber that reinforced a crack, another fiber was lying along the direction of cracking, creating a weak line. The increased tensile strength merely held the cube together after the sides of the cube had spalled off.

3.4 CONCRETE STRENGTHS

The concrete strengths of the four large test specimens were tested at seven, 30, and 91 days after the pour. Cylinders were not tested on other days because no significant damage to the concrete was observed. At seven days, the average compressive strength was 4040 psi. At 30 days, the compressive strength was 6220 psi. On the test day of 18S04, the compressive strength was 7430 psi and the split-cylinder strength was 716 psi.

The concrete strength of the smaller cylinder was tested at seven, 28, and 46 days after the pour. At seven days, the compressive strength was 5320 psi. At 28 days, the compressive strength was 7070 psi. At 46 days, on the test day of 08C08, the compressive strength was 8070 psi.

CHAPTER 4: PULLOUT TEST RESULTS

A total of 17 pullout tests were performed as part of this research. These tests can be divided into two categories based on whether or not the bar yielded. The bar remained elastic and failed by pull-out in all tests in which the embedded lengths were four bar diameters or less. These tests are denoted as short-embedment tests. All tests with embedded lengths of six bar diameters or more yielded the bar and are denoted as long-embedment tests.

Section 4.1 discusses the peak resistances reached during each test. Section 4.2 discusses the force-displacement behavior of the tests. Section 4.3 discusses the damage observed as a result of the tests.

4.1 PEAK RESULTS

The measured embedment length and peak tensile resistance reached during each test is listed in Table 4.1. The peak resistance is given as a load, as bar stresses calculated with each of the three bar areas, as average bond stresses, and as normalized average bond stresses achieved by dividing by f'_g or $\sqrt{f'_g}$.

Table 4.1: Peak resistances

Test	l_e (in.)	l_e/d_b (--)	P (kip)	σ_{nom} (ksi)	σ_{avg} (ksi)	σ_{net} (ksi)	τ_{avg} (ksi)	τ_{avg}/f'_g (--)	$\tau_{avg}/\sqrt{f'_g}$ (ksi)	Slip at P_{max} (in.)
08C08	8.00	8.00	58.0	73.4	77.3	80.6	2.31	0.29	0.96	¹
08N08	8.00	8.00	60.3	76.3	80.4	83.8	2.40	0.31	1.02	0.134
10F04	6.31	4.97	33.1	26.1	27.4	28.8	1.31	0.17	0.92	0.098
10N04	4.25	3.35	40.2	31.7	33.2	35.0	2.37	0.30	2.93	0.074
10N06	7.63	6.00	88.0	69.3	72.7	76.5	2.89	0.35	1.67	0.052
10N08	9.75	7.68	112.3	88.4	91.3	96.0	2.89	0.36	1.48	0.150
14N08	13.13	7.75	178.7	79.4	81.6	84.7	2.56	0.31	1.14	¹
18F02	4.63	2.05	37.5	9.4	10.0	10.2	1.14	0.16	0.98	0.048
18F03	7.19	3.18	119.7	29.9	31.9	32.7	2.35	0.31	1.35	0.045
18F04	9.38	4.15	167.0	41.8	44.5	45.6	2.51	0.37	1.34	0.149
18N02	4.38	1.94	29.4	7.3	7.8	8.0	0.95	0.11	0.81	0.052
18N03	6.19	2.74	142.5	35.6	38.1	38.8	3.25	0.42	2.02	0.120
18N04	9.50	4.21	186.2	46.6	49.8	50.7	2.76	0.32	1.31	0.112
18N06	13.81	6.12	301.0	75.3	80.3	82.2	3.07	0.31	1.21	¹
18N08	18.00	7.98	358.9	89.7	96.0	98.8	2.81	0.32	1.10	0.803
18N14	31.5	13.96	420.0	105.0	107.4	111.4	1.88	0.18	0.64	¹
18S04	9.00	3.99	93.2	23.3	24.9	25.7	1.46	0.18	0.73	0.041

¹Peak load reached after displacement readings became unreliable.

If τ_{avg} remained constant, the maximum bar stress achieved during a test would be linearly related to the normalized embedment length, l_e/d_b , according to the relationship in Equation 0.5. This assumption is implicit in the permission to reduce the development length by a factor of (As required)/(As provided) per ACI 318 §12.2.5 or AASHTO §5.11.2.1.3 (ACI 318-02, AASHTO LRFD 2005).

Figure 4.1 shows the peak nominal bar stress plotted against the normalized embedment length for each test. The relationship is roughly linear for a range of embedded lengths from three to eight bar diameters. However, the data do not tend toward the origin at very short embedment lengths. The test at 14 bar diameters departs from the linear relationship because of the capacity of the bar being reached.

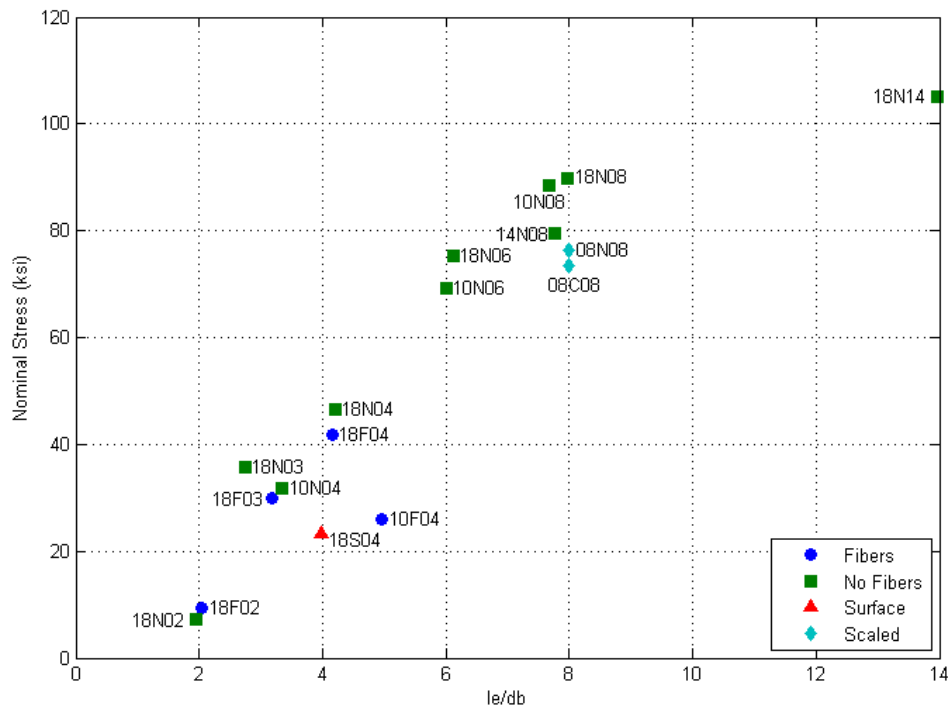


Figure 4.1: Peak nominal bar stress vs Le/db

4.2 FORCE-DISPLACEMENT BEHAVIOR

The front-end force-displacement behavior of the specimens is discussed here. The individual force-displacement plots for all 17 tests are provided in Appendix C. Examples of the short-embedment length tests are discussed in Section 4.2.2. Test

18N08, which included measurement of the back-end slip, is discussed in Section 4.2.3 as an example of a long-embedment length test.

4.2.1 Calculation of Front-End Slip

As shown in Figure 4.2, the actual front-end displacement can be calculated from the measured displacements and strains by subtracting the extension of the bar between the location of the displacement measurement and the surface of the grout. Equation 4.1 assumes that the strain measured by the gage is constant over the length between the pots and the surface of the grout.

$$u_{air} = \epsilon_{air} \cdot L_{air} \quad 4.1$$

Equation 4.2 was then used to calculate the front-end slip.

$$u_{surface} = u_{pot} - u_{air} \quad 4.2$$

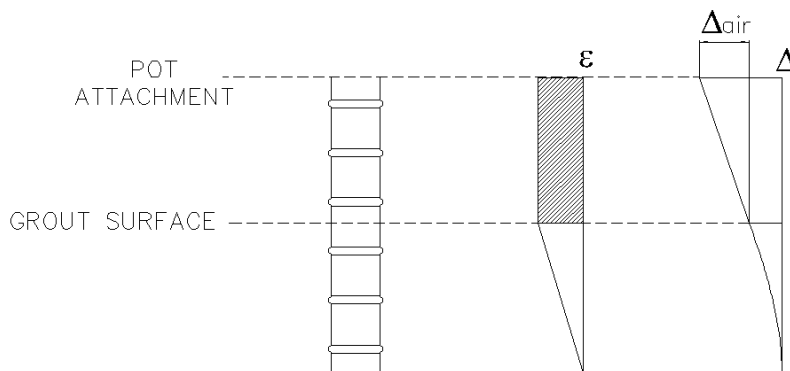


Figure 4.2: Bar stretch above the grout surface

The strain gages provided a local measurement of the bar strain at a location where the bar area was smaller than average. The gages were located between ribs of the reinforcing bars, and some steel was removed to place the gages. The measured strain was thus higher at this location than for the remainder of the “in air” bar, especially once yielding began. The calculated front-end displacement was therefore only an approximation of the actual front-end displacement.

4.2.2 Short-Embedment Length Tests

Four force-displacement plots are shown in Figure 4.3, representative of the short-embedment length test behavior. Test 18N02 is an example of a very short-embedment length test. Test 18N04 represents a more typical force-displacement behavior for short-embedment length tests. Test 18S04 displayed behavior very different than that seen in any other test.

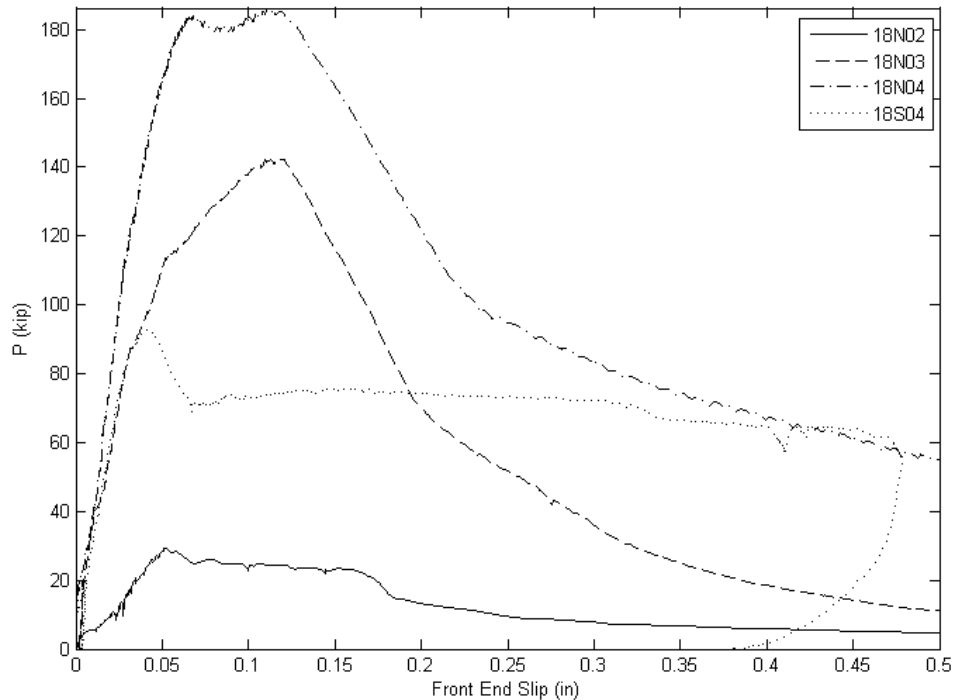


Figure 4.3: Short-embedment length force-displacement curves

The ascending branch of the force-displacement curves, shown in Figure 4.4, began almost linearly. The low-load (5 ksi) cycle at the beginning of each test imposed small permanent deformations. The largest of these deformations was 0.02 in. in test 18F02. The reloading path was identical to the unloading path. The stiffness decreased as the peak load was approached.

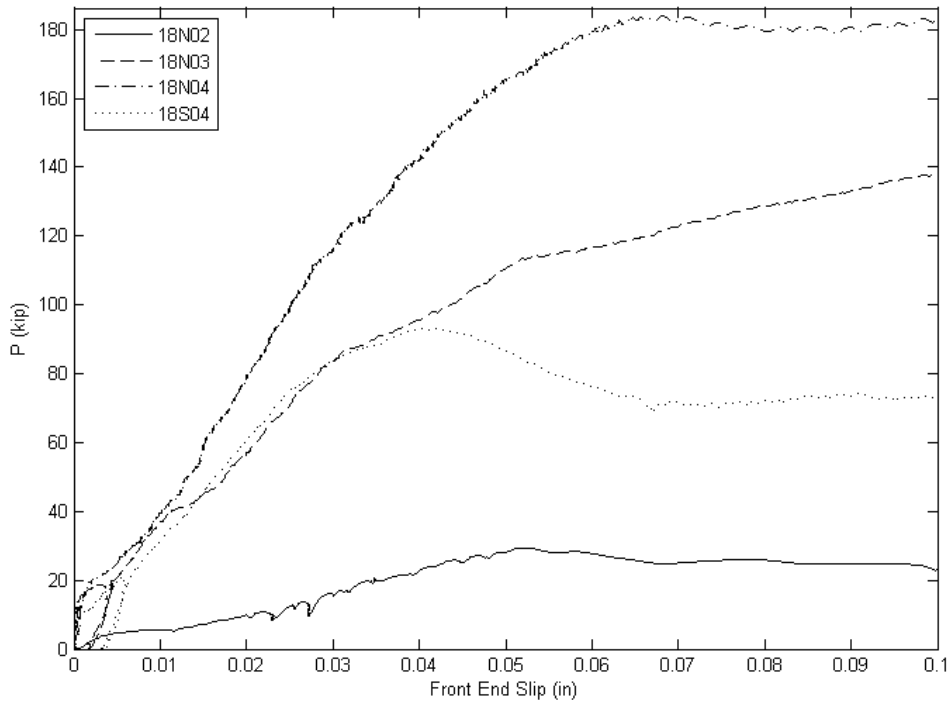


Figure 4.4: Ascending branch of short, no fiber, #18 tests

For most of the short-embedment length tests, a relatively flat section of the force-displacement curve was reached around the peak load. For example, test 18N04 exhibited two peaks of approximately similar magnitudes, and test 18N02 exhibited a relatively flat plateau after the peak. This plateau typically extended from a front-end slip of about 0.06 in. to about 0.12 in. Three short-embedment length tests reached the peak load without a plateau, including tests 10N04, 18F02, and 18N03.

In all tests except 18S04, further displacement resulted in significantly reduced resistance. This decreased resistance typically happened in two stages. In the first 0.1 in. after the peak load was reached, a sharp drop in load occurred. After reaching 0.2 to 0.25 inches of displacement, the resistance to further displacement continued to drop, but less rapidly, until the bar was completely removed from the grout.

Test 18S04 had a force-displacement relationship that differed significantly from that observed in any other test. The peak load was much lower than in test 18N04 with the same embedded length. After the peak load had been reached, displacements of the bar, grout, and concrete began to increase without significant change in the load. The

cause of the increased displacements and lowered peak load became apparent when the reaction block was lifted and the damage to the test specimen became visible, as discussed in Section 4.3.

4.2.3 Long-Embedment Length Tests

The force-displacement behavior of test 18N08 is shown in Figure 4.5 to illustrate the typical force-displacement behavior of the long-embedment length tests. The test setup for 18N08 included measurement of the back-end slip, which is shown in Figure 4.6.

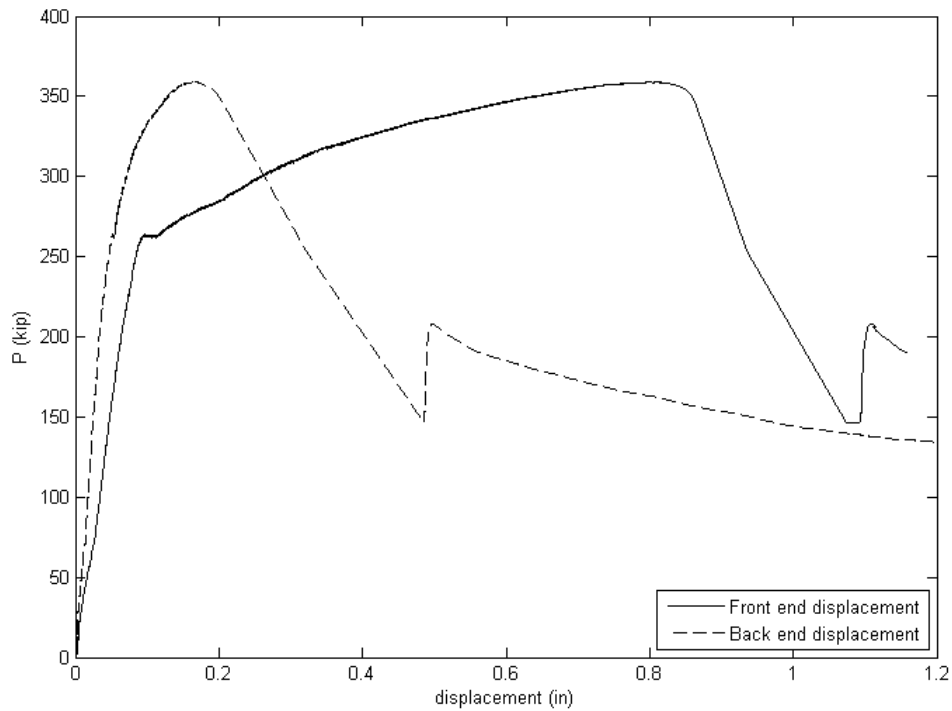


Figure 4.4: Force-displacement: 18N08

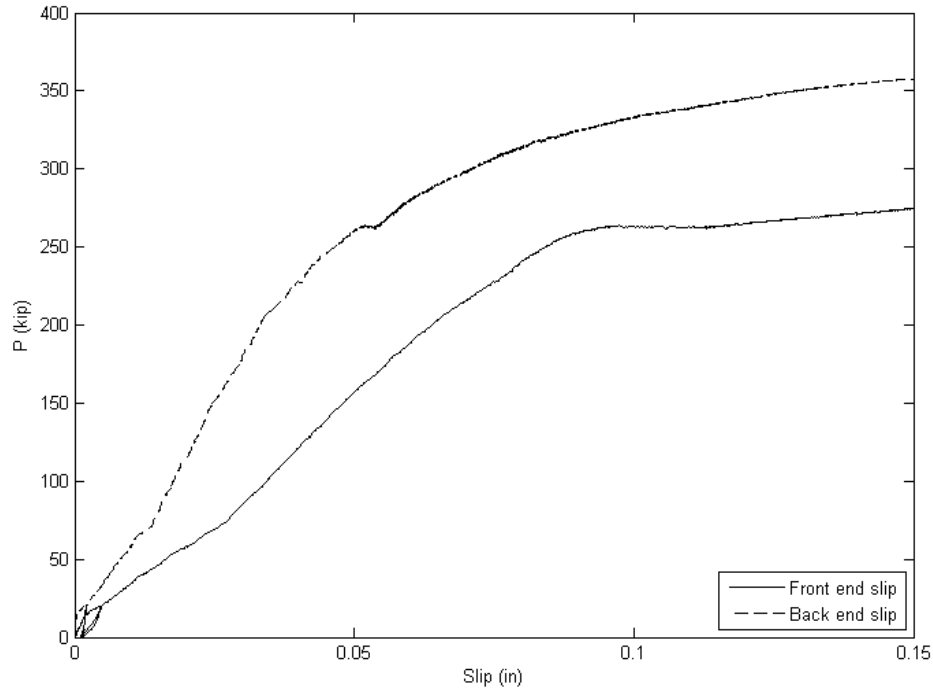


Figure 4.6: Force-displacement to yield: 18N08

The long-embedment length tests showed larger displacements than the short-embedment length tests, in part because of the bar yielding. The yield point was visible as a change in displacement without significant change of load. This effect was noticed even though an approximation of the deformation of the bar between the pots and the grout surface had been subtracted. As the bar strain hardened, displacements and load continued to increase until the grout or bar failed. Grout failure led to a sudden load drop of about 200 kips and a rigid-body motion of the embedded bar of 0.25 in. This failure was accompanied by a loud bang.

The back end of the bar began moving almost immediately in the test. At yield, the back end had moved 0.05 in., and it had moved 0.16 in. at the peak load. The difference between the front-end and back-end movement of the bar was the stretch of the bar inside the grout.

4.3 DAMAGE OBSERVATIONS

Damage to the grout and concrete was monitored in two ways. First, potentiometers measured displacements of the surface movements. In tests where the

grout surface was even with the surface to the top specimen (18S04, 18N14, 14N08, and 08N08), displacements of the grout surface were measured. In all other tests, the displacement of the duct at the surface of the specimen was measured. Second, damage was visually observed after the reaction block had been removed from the test specimen.

4.3.1 Short-Embedment Length Tests

No short-embedment test other than 18S04 exhibited surface movements of more than 0.003 in. These displacements were small because the forces applied were less than the yield forces of the embedded bars, and many of these tests were conducted deep in the test specimen. Testing low in the specimen resulted in smaller forces being applied to the concrete, resulting in small displacements of the duct and concrete and no cracking on the concrete surface.

Each bar was removed with some grout still attached. Other grout remained in the duct, either as a relatively undamaged mass or as fragments that could be removed. The damaged fiber-reinforced grout tended to be removed as a large block attached to the bar. Smaller cracks in the grout were held together by the fibers. In the specimens without fiber reinforcement, these cracks left the grout in fragments.

In test 18F02, the grout removed with the bar formed the cone shown in Figure 4.7. After test 18N02, a similar cone was reconstructed from the large fragments of grout found in the duct. The cone of grout removed with 18F02 extended from the lowest embedded lug to the top surface of the grout at approximately a 45-degree angle. The reconstructed cone from 18N02, shown in Figure 4.8, was somewhat shallower. The cone may have been steeper in the specimen, since not all fragments of grout were recovered. Both cones showed signs of radial cracking in addition to the angled failure surface.



Figure 4.7: Grout cone: 18F02



Figure 4.8: Grout cone: 18N02

Grout cones were found after each grouted test except 18S04. The depth and angle of the cone varied slightly among the tests but generally were between 30 and 45 degrees from horizontal. Some cones, like that in 18N04, appeared to be formed by a single, angled crack extending from the bar to the duct. Others formed a series of cones, with some conical cracks at very shallow angles. Grout damage of this kind is shown in Figure 4.9.



Figure 4.9: Layered grout cone: 14N08

Below the cone, the bar pulled through the grout. In several tests, grout remained in the interstices between transverse lugs, forming a relatively smooth cylinder, shown in Figure 4.10. This cylinder was defined by the diameter of the lugs.



Figure 4.10: Grout cone and sheared grout: 18F04

This cone-and-cylinder failure surface through the grout was found in all short-embedment length tests except 18S04. This includes the tests on #10 and #14 bars. The size of the cone was similar for these tests, indicating that the diameter of the duct, rather than the size of the bar, controlled the depth of the cone. The confinement that the duct provided to the grout below the cone prevented deeper cones from forming.

4.3.2 18S04

Test 18S04 was run in a separate section of duct, which was thus freer to move through the concrete than the ducts used for other tests. The concrete and grout surfaces moved much more in test 18S04 than in any other test. These movements are shown in Figure 4.11. The unique behavior is attributed to the fact that the bar was bonded in a 9-in.-length of duct embedded in the top of the cylinder, as shown in Figure 2.1. Failure was associated by a concrete splitting failure of the top surface of the cylinder.

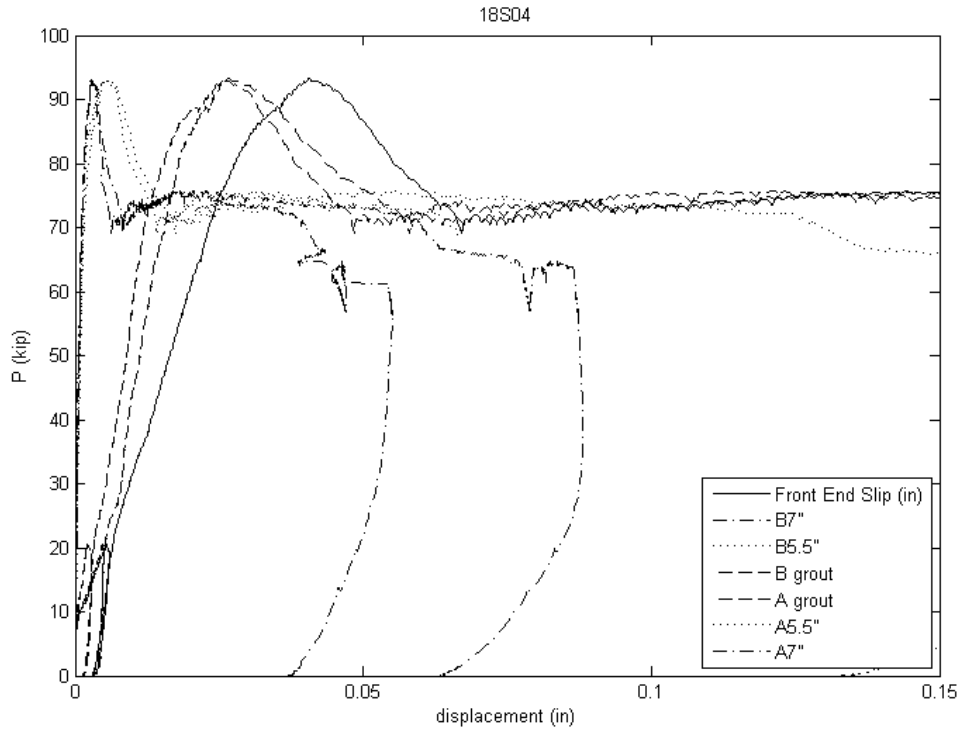


Figure 4.11: Force-displacement: 18S04

The spiral reinforcement in the test specimen also debonded and was pulling around the concrete cylinder, shown in Figure 4.12. This reinforcement was ineffective at confining the concrete, and the concrete split. When the reaction block was removed, the splitting of the top surface was observed. The grout was intact, but the duct pulled through the split concrete.



Figure 4.12: Reinforcement: 18S04

This mode of failure was suppressed in many of the other specimens. Other tests were run in ducts that were embedded in the concrete beyond the grouted embedment length. The duct in 18S04 was embedded in the concrete for 9 in., the same as the embedment length of the bar. This specimen was not restrained by any effective reinforcement, leading to the splitting failure (Figure 4.13). Splitting of the concrete did not occur in the other specimens in which the duct was embedded the same distance as the bar, 18N14 and 08N08.



Figure 4.13: Concrete splitting: 18S04

4.3.3 Long-Embedment Length Tests

In the long-embedment length tests, the forces were relatively large, but damage to the concrete test specimen was light. Duct movement at peak load was less than 0.05 in. Concrete surface movements did not exceed 0.01 in. at the peak load. The top surface of the concrete had some radial cracks. These tests involved higher loads and were performed closer to the surface of the test specimens than the short-embedment length tests. Of the long-embedment tests, the radial cracking was most extensive in test 18N14, shown in Figure 4.14

The damaged grout in the long-embedment tests formed grout cones in the top of the embedment length similar to, but shallower than, those in the short-embedment length tests. The grout cone formed during test 18N14 was the shallowest found, less than 20 degrees from horizontal. Wedges of grout about 1-in. deep were removed from the top surface of the grout.

Tests 18N06, 18N08, 10N06, 10N08, and 14N08 ended in grout failure. Below the grout cone, the bars sheared through the grout along a cylinder defined by the transverse lugs, just as it did in the short-embedment length tests. Test 18N14 ended in rupture of the bar. After the peak load of 420 kips was reached, the bar lost significant load to necking before fracturing. The fractured bar is shown in Figure 4.14.

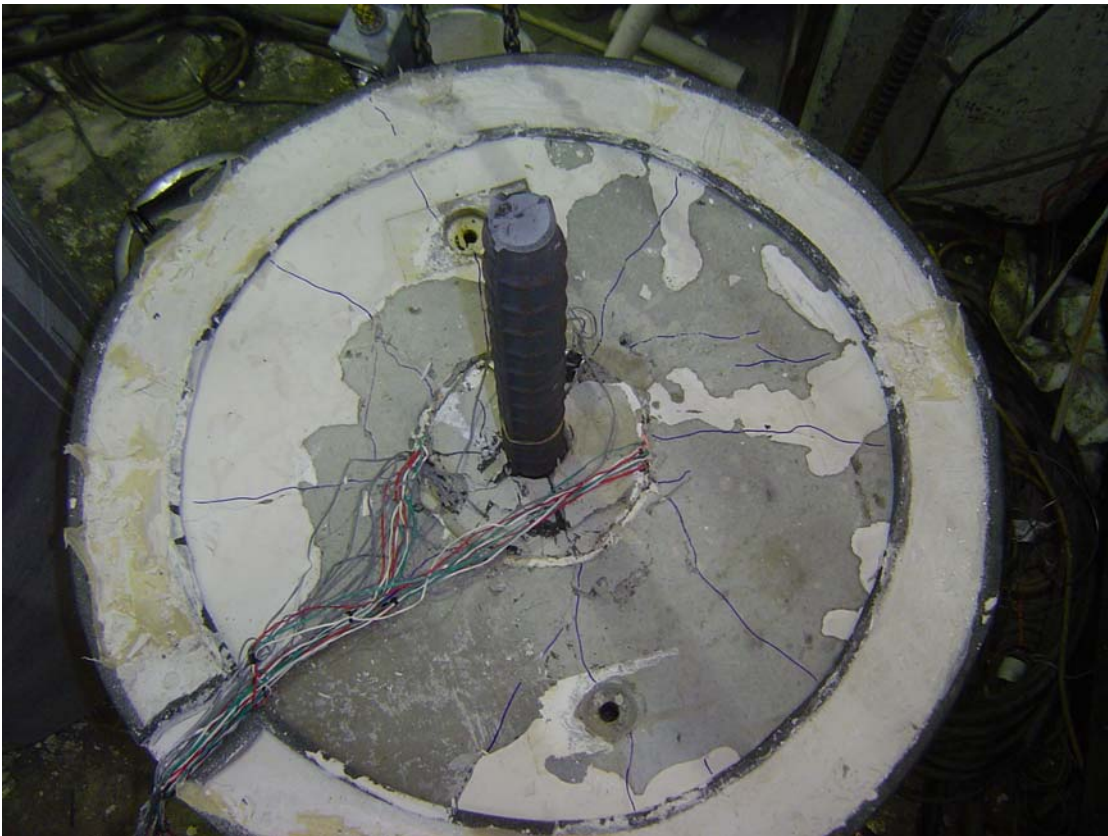


Figure 4.14: Fractured bar: 18N14

4.3.4 Scaled Tests

The bar in test 08C08 was embedded directly in concrete. The failure was by formation of a large concrete cone that extended from the bottom of the embedded bar to the outer surface of the concrete, shown in Figure 4.15. Like some of the grout cones in other specimens, the concrete cone was composed of more than one layer of conical cracking.



Figure 4.15: Concrete damage: 08C08

Test 08N08 exhibited grout failure along several surfaces. In the top 2 in. nearest to the surface, a plug of grout pulled out along the duct surface, shown in Figure 4.16. Below this, a 30-degree cone brought the failure surface to the bar. Below the cone, the bar pulled out along a shearing cylinder similar to that of other tests.



Figure 4.16: Grout damage: 08N08

The concrete surface of the test specimen was also damaged. Several radial cracks formed in the concrete, and the concrete surface was displaced upwards in some locations. The extent of damage was similar to that seen in 18N14.

CHAPTER 5: DISCUSSION OF FINDINGS

This chapter discusses the experimental results. Failure mechanisms are discussed in Section 5.1. The effects of variable grout strength, presence of fibers, and bar size are discussed in sections 5.2 through 5.4. The effect of yielding the reinforcing bar is discussed in Section 5.5. The results of this research are compared to previous research and the building codes in Section 5.6.

5.1 GROUT FAILURE MECHANISMS

Two distinct failure mechanisms of the grout were shown in Figure 4.10. Near the surface, a cone of grout formed. Below this cone, a cylinder consisting of the reinforcing bar and grout between the lugs slid through the remaining grout in the specimen. The difference between the two mechanisms was the result of the difference in confinement provided by the duct and surrounding concrete. This effect has been seen in pullout tests performed in confined concrete specimens (Viwathantepa 1979).

The confinement provided by the duct and concrete was ineffective near the grout surface because of the mechanism that transfers load from the bar through the grout to the duct. Before cracking, bond stresses were carried as shear stresses in the grout. When the tensile capacity of the grout was exceeded, the grout cracked along a plane normal to the principal tensile stress. The shear stress is inversely related to the distance from the axis of the bar, and was thus highest next to the bar and lowest next to the duct. This resulted in steep cracking near the bar and shallower cracking close to the duct, with a curved surface in between.

After cracking, the axisymmetric strut-and-tie model shown in Figure 5.1 developed in the grouted region. Angled struts formed to carry the applied load, and horizontal equilibrium was provided by the hoop stresses in the steel duct and surrounding concrete. Close to the front end of the bar, struts would have to have been very shallow in order to connect to the duct. These shallow struts could not carry as much vertical load as deeper struts.

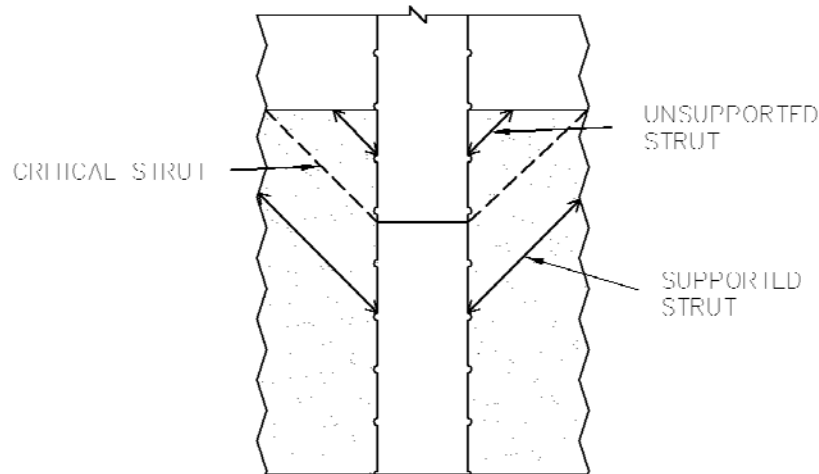


Figure 5.1: Struts in grout

Struts near the grout surface could not maintain horizontal equilibrium, and the cracked grout was free to separate. This grout formed the cone that was observed at angles from about 20 to 45 degrees in various tests. This angle was related to the overall dimensions of the cone, since the cracked surface was usually irregular and curved as mentioned above. The cone in test 18N14 was the shallowest observed because the full bond capacity was not mobilized before the bar fractured.

In the confined regions of grout, the individual struts were strong. Before the struts crushed or the ducts exceeded their capacity to confine the grout, another failure mechanism controlled the local bond strength. This failure mechanism was the shearing cylinder observed in tests with more than 4.5 in. of embedment length. The bar and grout formed a relatively smooth cylinder that passed through the confined grout, which remained in the specimen. Shear friction and aggregate interlock provided the remaining resistance to sliding after failure.

The shear cylinder mechanism provided higher bond stresses than the cone mechanism. In the shortest tests (18N02 and 18F02), the cone region took up nearly the full embedded length, and no shear cylinder formed. These tests also developed much lower than average bond stresses, as shown in Figure 5.2.

5.2 EFFECT OF GROUT STRENGTH

The grout strength was not systematically varied among the tests in this experimental program, but some variation was observed. The grout strength on test day ranged from 6.8 ksi to 10.3 ksi. A relationship is presumed to exist between the grout strength and the maximum bond stress that can be achieved. The peak average bond stress is plotted against the grout strength in Figure 5.2.

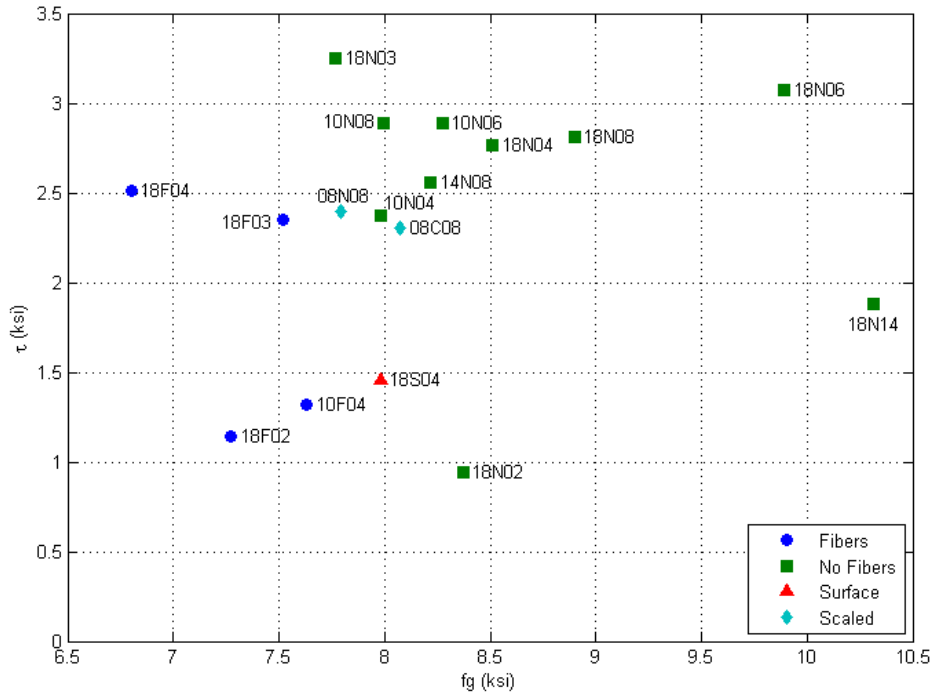


Figure 5.2: τ_{avg} vs grout strength

Two tests, 18N14 and 18S04, did not fail by bond failure. The peak τ_{avg} values were thus not related to the available bond capacity. In the shortest embedment length tests (18N02 and 18F02), failure was controlled by cone mechanism, which also resulted in low peak τ_{avg} values.

Researchers have taken the peak bond stress to be a function of concrete or grout strength in a number of ways. Raynor and pre-1963 ACI codes assumed that the peak bond stress varies linearly with the grout compressive strength, f'_g . Other research and current code expressions relate τ_{avg} to $\sqrt{f'_g}$ (Eligehausen 1983, Viwathantepa 1979,

Martin 2006). From Figure 5.2 it is not clear which form is more appropriate for normalization, both because of the limited range of grout strength used and because other factors, including the embedded length, influenced the bond stress. The following discussion compares the scatter of the data when they were normalized by each method.

Figure 5.3 shows the peak average bond stress plotted against the embedment length. Peak values for the majority of tests are between 2.25 and 3 ksi. The coefficient of variation for all tests except the five with bond stresses of less than 2 ksi is 11.1 percent.

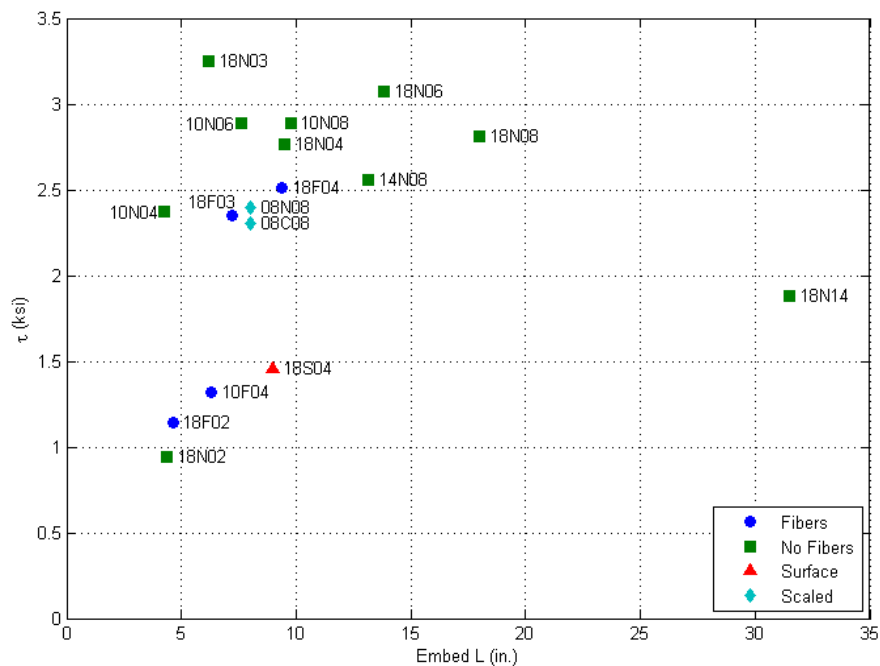


Figure 5.3: τ_{avg} vs L_e

Figure 5.4 shows the peak average bond stress normalized by the grout strength plotted against the embedment length. Here, the data cluster more closely around $0.3f_g$. Except for the same five tests listed above, the coefficient of variation is 10.9 percent. This form of normalization makes the most sense if the failure mode is related to crushing of the grout.

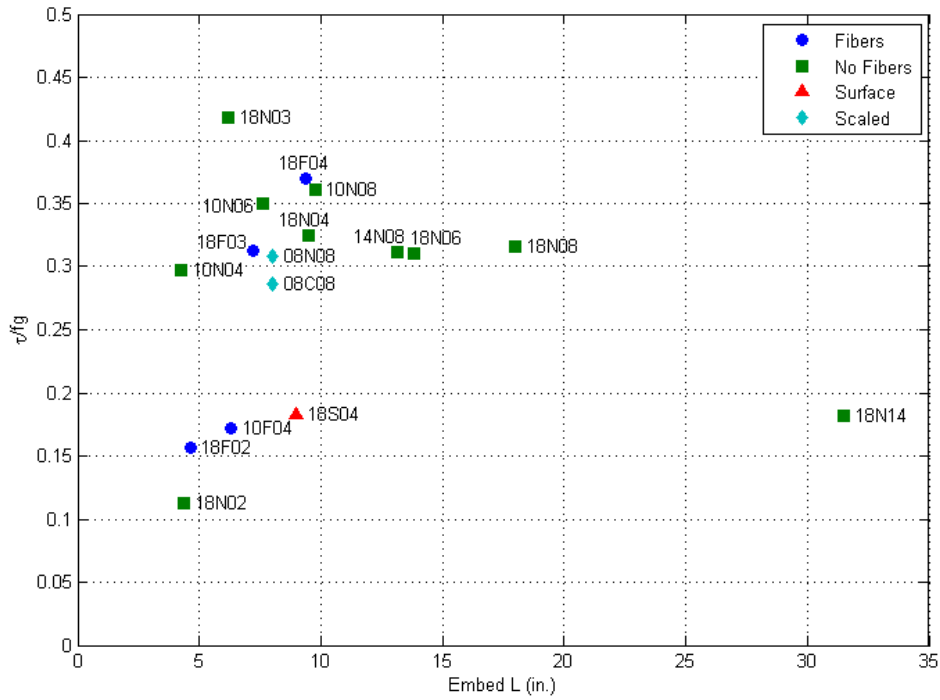


Figure 5.4: τ_{avg}/f'_g vs l_e

Figure 5.5 shows the peak average bond stress normalized by the square root of the grout strength plotted against the embedment length. Except for the same five tests listed above, the coefficient of variation is 10.0 percent. This form of normalization makes the most sense if the failure mechanism is related to splitting of the grout.

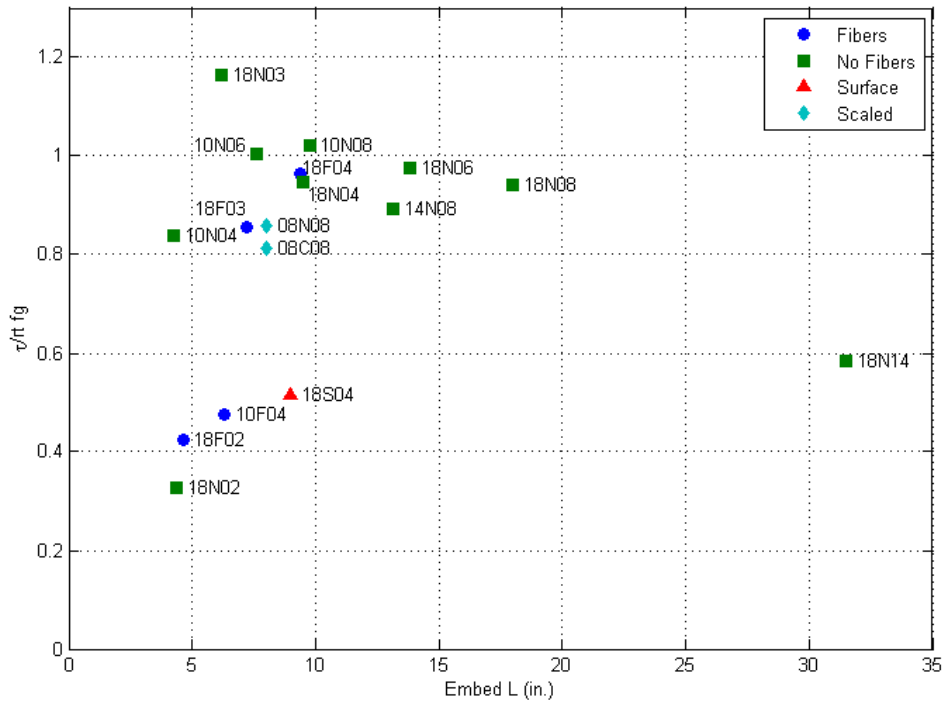


Figure 5.5: $\tau_{avg}/\sqrt{f'_g}$ vs l_e

Normalizing the peak average bond stress slightly reduced the variation among the tests. Because the range of tested grout strengths was relatively small, it is difficult to determine the best form of normalization for a bond model. For further calculations, bond stresses were normalized by $\sqrt{f'_g}$.

5.3 EFFECT OF FIBERS

Previous research (Raynor 2000, Nakaki 1999) used fiber-reinforced grout to grout bars and gaps between precast elements. The same type of polypropylene fibers used by Raynor was used for the four “F” tests in this research (18F02, 18F03, 18F04, and 10F04). Each of the fiber-reinforced tests had a corresponding non-fiber-reinforced test (18N02, 18N03, 18N04, and 10N04).

The presence of fiber reinforcement in the grout for the pullout tests did not provide any beneficial effect. With one exception (18N02 and 18F02), the peak loads reached in the fiber-reinforced specimens were lower than those achieved in the non-

fiber-reinforced specimens. Because of the lower grout strength, normalized bond stresses were higher than those of the corresponding unreinforced specimen in tests 18F02 and 18F04, but lower than those in tests 18F03 and 10F04.

Figure 5.6 compares the τ_{avg} -displacement behavior of tests 18N03, 18F03, 18N04, and 18F04. The normalized bond resistance is used to provide a comparison between the different embedded lengths. The ascending branches of the bond-slip relationships are shown in Figure 5.7.

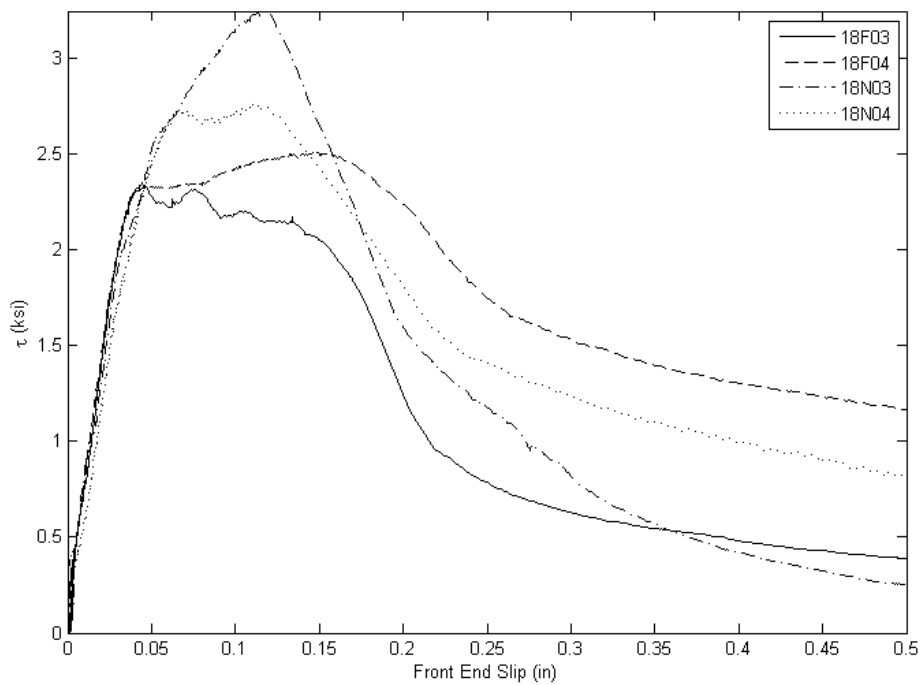


Figure 5.6: Fiber and no fiber bond stress-displacement comparison

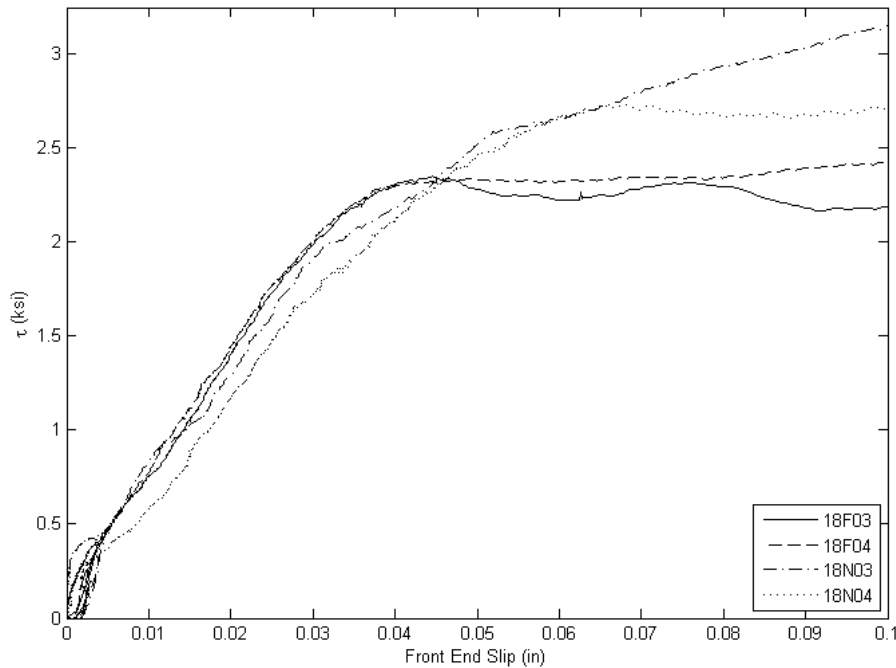


Figure 5.7: Ascending branch of bond-slip histories

The fibers had been expected to improve post-peak behavior by bridging cracks in the grout. However, no improvement to post-peak behavior was observed. The ability for cracked grout to hold together may be important for pads between precast elements but does not appear to improve bond characteristics.

Note that fiber reinforcement may provide benefits during cyclic loading that did not become apparent during the monotonic pullout tests described here.

5.4 EFFECT OF BAR SIZE AND GEOMETRY

Bars from #10 to #18 were tested in the full-scale, 8-in. ducts. This research was conducted largely to find whether large-diameter bars can develop bond stresses similar to those of small-diameter bars. Previous research (Eligehausen 1977, Raynor 2000) has found little evidence for a bar size effect but has been conducted over much smaller ranges of bar size. Tests were also conducted to confirm that the ducts and bars were scaled appropriately for the column-to-beam connection testing.

5.4.1 Full-Scale Tests

Bond models have been presented that relate the local bond stress to a normalized slip, s/d_b (Martin 2006). Normalizing the front-end displacements by the bar diameter allows for stress-displacement behavior to be compared among bar sizes.

Figure 5.8 shows stress-normalized displacement relationships for the three tests with embedment lengths of eight bar diameters conducted in the full-scale ducts.

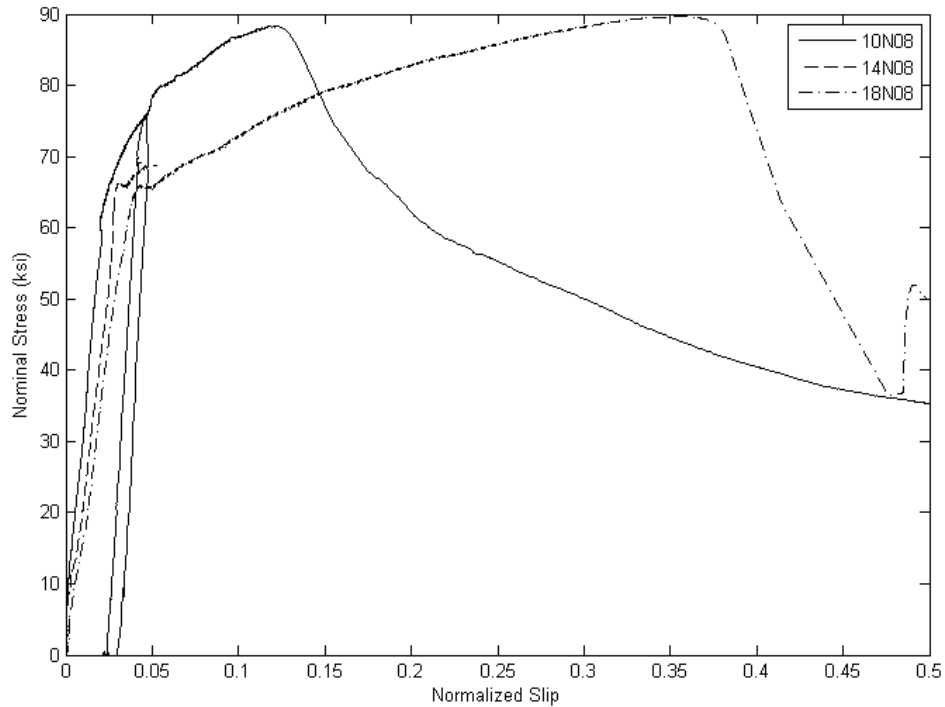


Figure 5.8: Eight-db embedment length tests (Note: displacements for 14N08 became unreliable before the peak stress was reached.)

The peak bar stress in test 14N08 was slightly lower than those in tests 18N08 or 10N08, but there is no evidence of a significant bar size effect. Tests on the #10 and #18 bars recorded sudden drops in the load not long after the peak load was reached, although these drops occurred at different displacements. Although the displacements were normalized by the bar diameter, the smaller bars showed stiffer ascending branch behavior. This suggests that this normalized displacement may not capture the variation in behavior among the range of bar sizes, although it is more accurate than the absolute displacement.

Figure 5.9 shows four tests conducted with nominal embedment lengths of four bar diameters. These tests were all conducted in the 8-in. CMP duct. The tests on the #10 bars reached lower peak loads than the tests on the #18 bars. The absolute, as opposed to normalized, embedment lengths were shorter for the #10 bars. Because the unconfined region of the grout was related to the duct size, more of the embedment length of the #10 bar lay in the unconfined region than that of the #18 bars.

Unlike the longer eight- d_b tests, the response of the smaller bars was less stiff than that of the large bars (see figures 5.9 and 5.10). Like the decreased peak load, this effect is likely related to the relatively longer section of bar that is in the unconfined, cone region of embedment.

Variations in other geometric properties of the bar (e.g. R_r) were not systematically varied among the tests and were not used as predictors of performance.

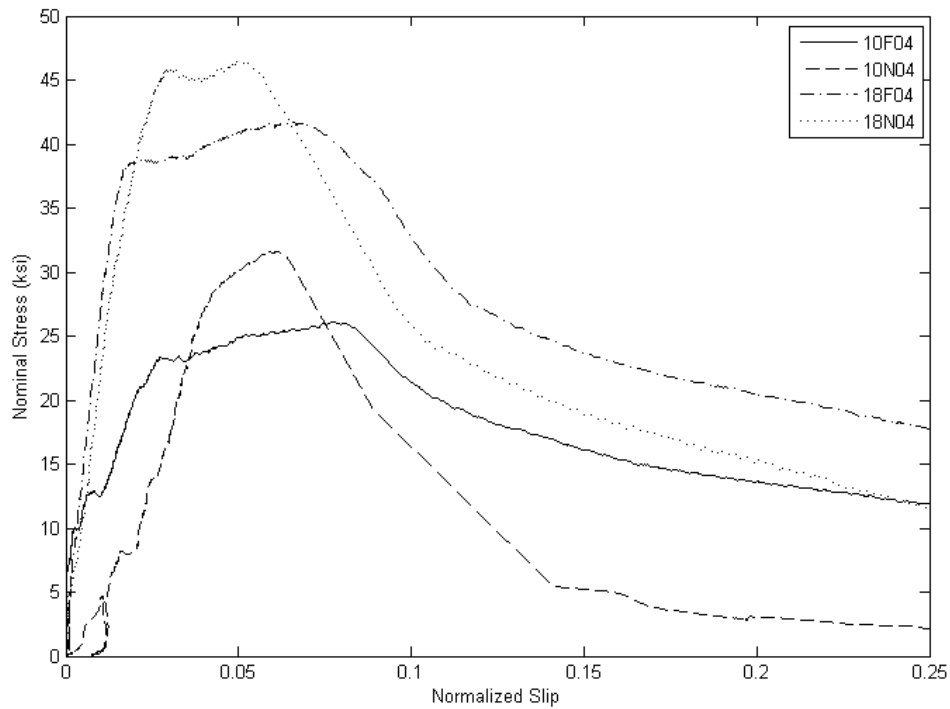


Figure 5.9: Four-db embedment length tests

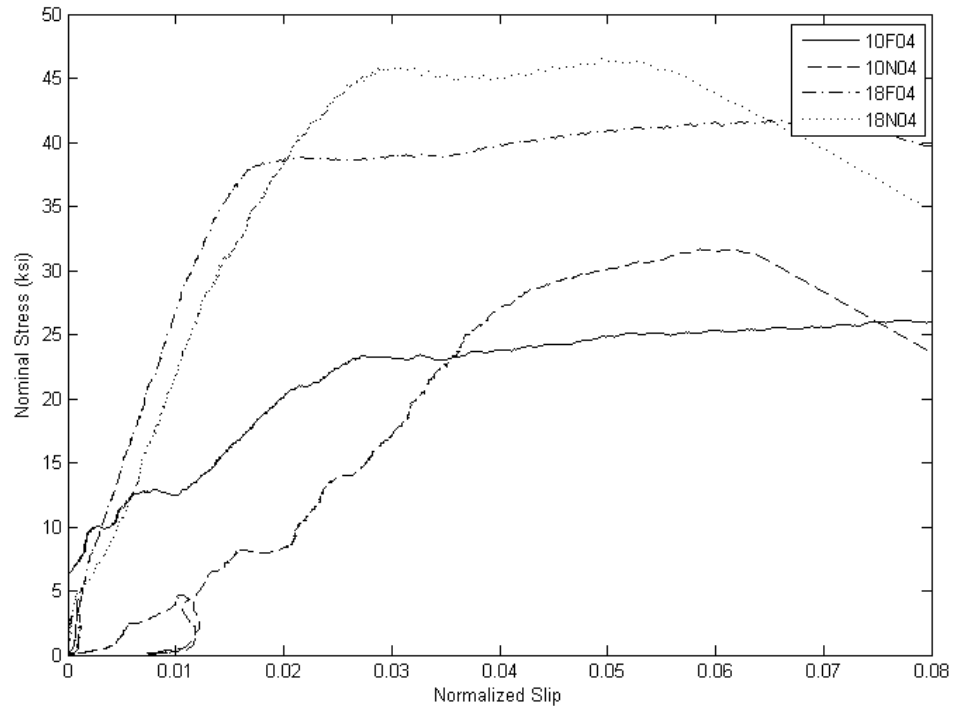


Figure 5.10: Initial response of four- d_b embedment length tests

5.4.2 Scaling for Joint Tests

Test 08N08 was a scaled version of test 18N08. The bar and duct used for 08N08 were used in the pseudostatic column-to-cap beam joint testing. The force-displacement behavior in these two tests, expressed here as the nominal bar stress and normalized slip, is shown in Figure 5.11.

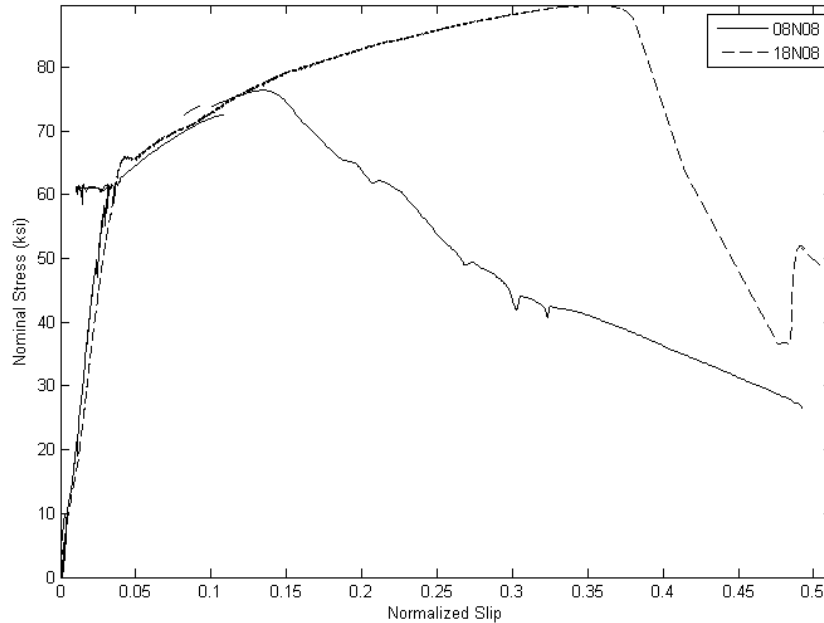


Figure 5.11: Scaling comparison

The two tests had similar stiffnesses up to yield. When the bar in test 08N08 yielded, the displacement measurements showed backwards movement of the bar. This effect was an artifact of the procedure used to convert the measured quantities to slip at the surface of the grout, and was more pronounced in smaller bars.

Test 18N08 reached a higher bar stress than 08N08. Both bars began to strain harden before pulling through the grout. The similarity of the response showed that this scaling was appropriate for use in the joint tests.

5.5 EFFECT OF YIELDING

When the reinforcing bar yields, two effects reduce local bond stresses. First, the large strains associated with yielding cause deformations that increase slip of the bar. This increased slip can locally exceed the displacement for peak bond stress, reducing the bond. Second, plastic deformation reduces the area of the bar. At strains of approximately 20 percent, the bar area is reduced to the extent that the lugs disengage from the grout, destroying the bond (Raynor 2000). These two effects are independent in principle but were strongly linked in these tests.

Section 5.1 introduced the idea of a shearing cylinder. If this cylinder has already formed, the reduction in area required to reduce the aggregate interlock across the sliding interface should be small, especially for a grout with only fine aggregate. It is difficult to distinguish between these effects in the data. Although it is reasonable to assume that yielding the reinforcing bar reduces bond independent of the increased slips, and tests by Raynor showed this effect, the effect cannot be quantified from these data.

However, the peak bond stress did not appear to be negatively affected by yielding for the specimens that failed by pullout. In fact, the peak average bond stress reached in tests 10N08, 18N08, and 18N06, which yielded the bars, was higher than the peak average bond stress reached in tests 18N04 and 10N04, which did not.

5.6 COMPARISON TO CODES AND PREVIOUS RESEARCH

Figure 5.12 shows the peak stress from each test plotted against the normalized embedment length. If τ_{avg} were constant among the tests, then the points would fall along a line. The figure also shows the bar stresses implied by the ACI and AASHTO code development length equations and by Raynor's development length equation.

The bar stresses implied by the code equations are very low in comparison to the values reached during the tests. This confirms the expectation that the code equations are excessively conservative for the development of bars in grouted ducts. Many of the tests on which the code development lengths were based were conducted on splices of bars embedded in concrete (Orangun 1977). Such splices tend to fail through splitting of the concrete, but in the tests described here, that mode of failure was suppressed by the duct and large concrete specimen.

Raynor's development-length equation is unconservative when applied to these tests.

Within each test series, neither Raynor's tests nor this research showed a significant effect due to bar size. This suggests that the difference in results was due to the test setup itself. Raynor's tests were conducted on a section of reinforcing bar grouted into a duct that was embedded in a concrete block. Most of the reinforcing bar was debonded from the grout by a PVC pipe, thereby eliminating the possibility of a cone forming. The entire bonded region could form struts through the grout to the

confinement provided by the concrete and duct. Some of these struts passed through sections of the grout that were not part of the bonded length of the bar.

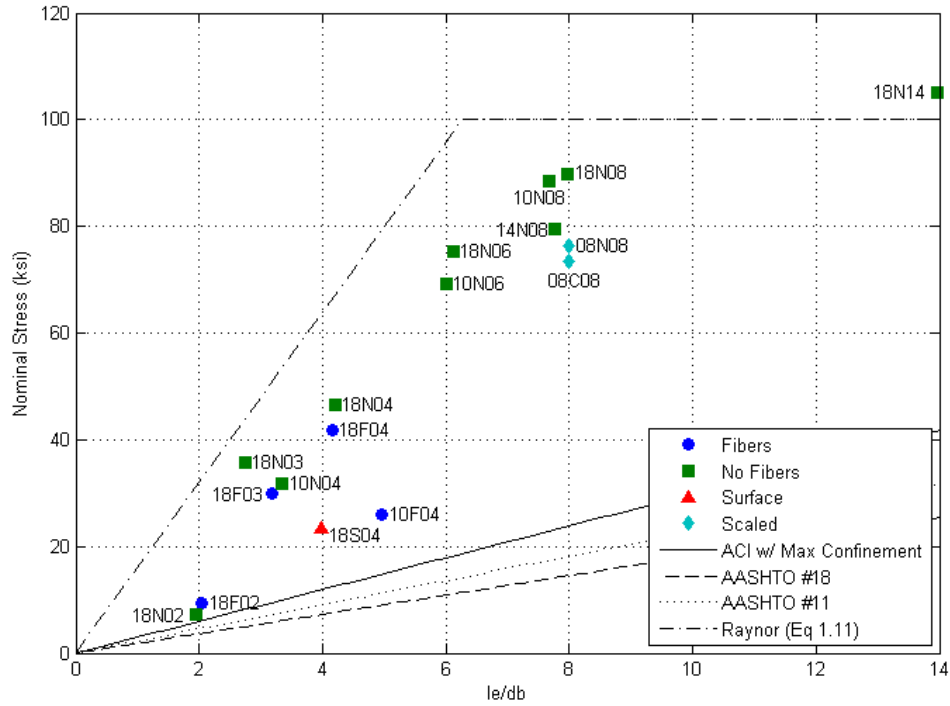


Figure 5.12: Stress vs l_e/d_b with predictions

CHAPTER 6: LINEAR AND NONLINEAR MODELING

In general, the bond-slip and the steel constitutive relationships are nonlinear, and the bar bond problem cannot be solved in closed form. Simplifying these relationships to linear conditions allowed a closed-form model to be developed. This model, presented in Section 6.1, is applicable to the initial, linear response of the specimens, and it provides insight into the general behavior of the specimens. The remainder of this chapter discusses a nonlinear finite element model that can be used to analyze the behavior of the specimens beyond the initial, linear region.

6.1 LINEAR MODEL

The closed-form model presented here was developed by Raynor (Raynor 2000).

6.1.1 Model Form

The closed-form model assumes linear bond-slip and steel stress-strain responses.

That is,

$$\tau(x) = k \cdot u(x) \quad 6.1$$

and

$$\sigma(x) = E \cdot u'(x) \quad 6.2$$

Equilibrium requires

$$A \frac{d\sigma}{dx} = \Pi \cdot \tau(x) \quad 6.3$$

where A is the cross-sectional area of the bar and Π is its perimeter.

By combining equations 6.1 through 6.3, one obtains the following differential equation,

$$A \cdot \frac{d}{dx} [E \cdot u'(x)] = \Pi \cdot k \cdot u(x) \quad 6.4$$

For these equations, x is measured from 0 at the front end of the bar to L_e at the back end of the bar. The boundary conditions are

$$\sigma(L_e) = E \cdot u'(L_e) = 0 \quad 6.5$$

and

$$\sigma(0) = E \cdot u'(0) = \sigma_o \quad 6.6$$

Solving the differential equation, the slip at any location in the embedded length is given by Equation 6.7,

$$u(x) = \frac{\sigma_o}{E\lambda} \frac{\cosh \lambda(L_e - x)}{\sinh \lambda L_e} \quad 6.7$$

where λ is given by Equation 6.8, L_e is the embedded length of the bar, x is the distance from the front end of the bar, and λ is given by

$$\lambda = \sqrt{\frac{k\Pi}{EA}} \quad 6.8$$

The tension stiffness of the bar relative to the shear stiffness of the interface grout, expressed by the dimensionless term λL_e , is important to the overall behavior of the model. The slip distribution will vary from nearly linear to highly nonlinear as the value of λL_e increases. A comparison of the slip distributions for three values of λL_e is shown in Figure 6.1.

For large values of λL_e , (i.e., the grout is stiff in comparison to the bar), the bond and slip distributions in the embedded length are highly nonlinear. For small values of λL_e (i.e., the bar is stiff in comparison to the grout), the bond stress and slip distributions are nearly constant, and the bar stress and strain distributions are nearly linear throughout the embedded length.

The linear slip equations can be used to calculate to a parameter, β , which represents the fraction of the front-end slip that results from rigid-body motion of the bar. The remainder of the front-end slip results from deformation of the embedded bar. This slip fraction calculated by Equation 6.9 is only accurate when the bar and grout respond linearly. Nonetheless, the following equation provides a simple parameter for evaluating the response of a specimen.

$$\beta = \frac{u(L)}{u(0)} = \frac{1}{\cosh \lambda L_e} \quad 6.9$$

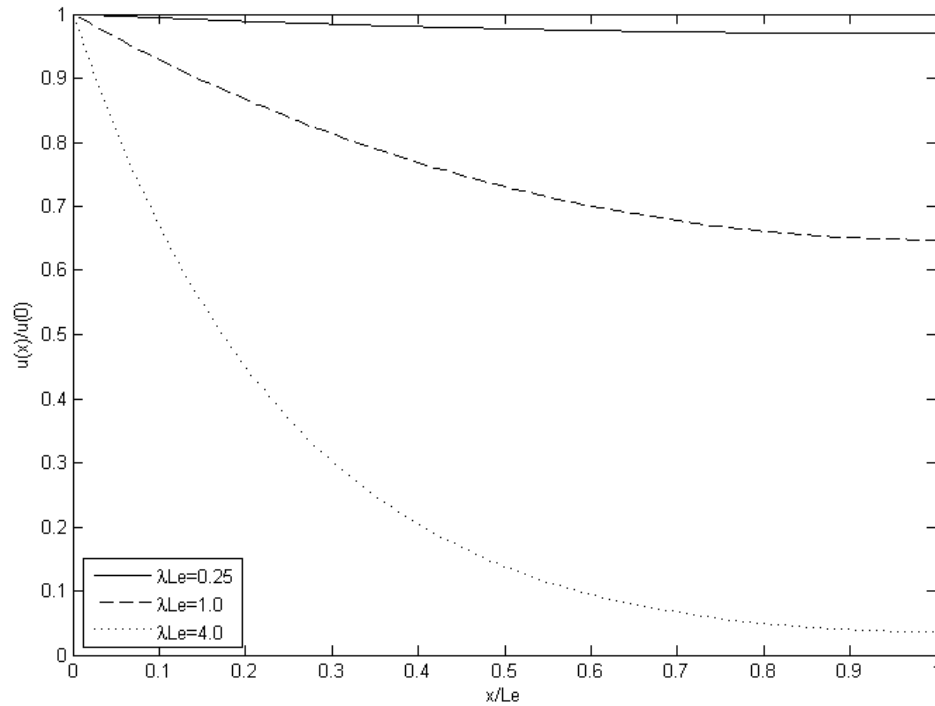


Figure 6.1: Slip distributions for varying λL_e values

6.1.2 Model Calibration

Most of the terms in Raynor’s linear equations are easily determined from the bar properties, but the bond stiffness, k , must be determined from experimental evidence.

The average bond-slip response was nearly linear for most specimens until near the peak load. Two points on the bond-slip plot were selected, and the stiffness between these points was calculated, as shown in Figure 6.2.

$$K = \frac{\Delta \tau_{avg}}{\Delta u(0)} \quad 6.10$$

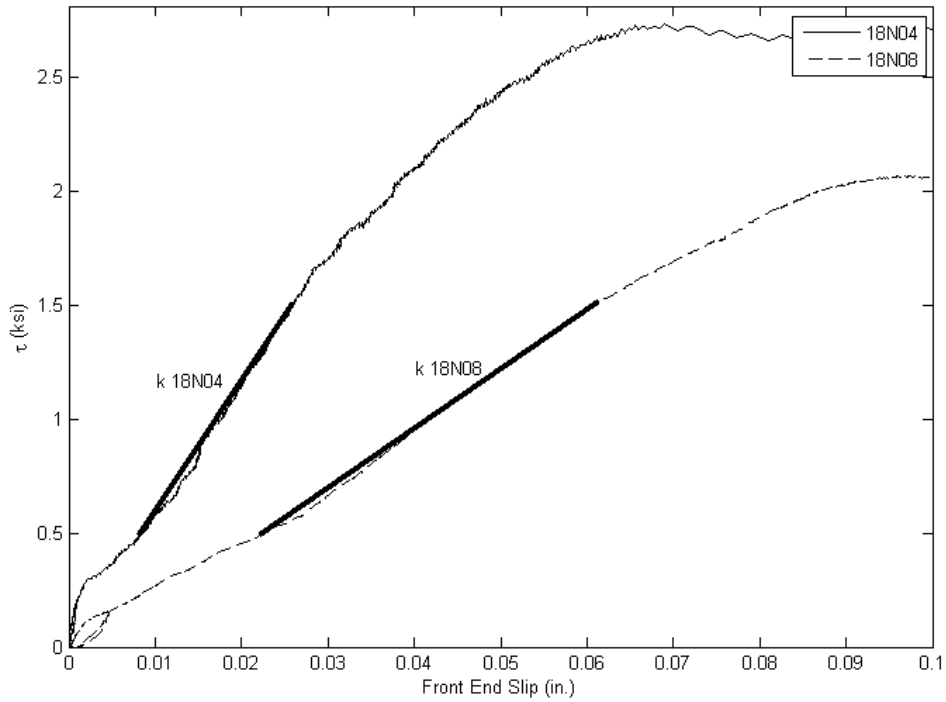


Figure 6.2: Bond stiffness calculation

The average bond stiffness, K , was calculated for the response between 0.5 ksi and 1.5 ksi, except for 18N02 and 18F02, which were calculated in the range of 0.5 ksi to 1.0 ksi. Bond stiffnesses ranged from about 20 ksi/in. for the shortest embedment length tests to about 75 ksi/in. for specimen 18F04. The average bond stiffness for each of the #18 tests is shown in Table 6.1.

The local bond stiffness can be calculated from the average bond stiffness. The average bond stress is given by

$$\tau_{avg} = \frac{\sigma_o A}{\Pi L_e} \quad 6.11$$

and the front-end slip is given by

$$u(0) = \frac{\sigma_o}{E\lambda} \cdot \frac{\cosh(\lambda L_e)}{\sinh(\lambda L_e)} \quad 6.12$$

These equations can be combined to give

$$K = k \frac{\tanh(\lambda L_e)}{\lambda L_e} \quad 6.13$$

This equation can be solved to find the local bond stress, k . The calculated values are shown in Table 6.1 and Figure 6.3

Table 6.1: Average and local bond stiffness

Test	K (ksi/in.)	k (ksi/in.)
18F02	24.0	24.3
18F03	62.0	66.8
18F04	66.2	76.0
18N02	21.0	21.2
18N03	56.5	59.4
18N04	57.8	65.4
18N06	53.4	68.3
18N08	27.1	33.5
18N14	17.5	27.1
18S04	45.3	49.3

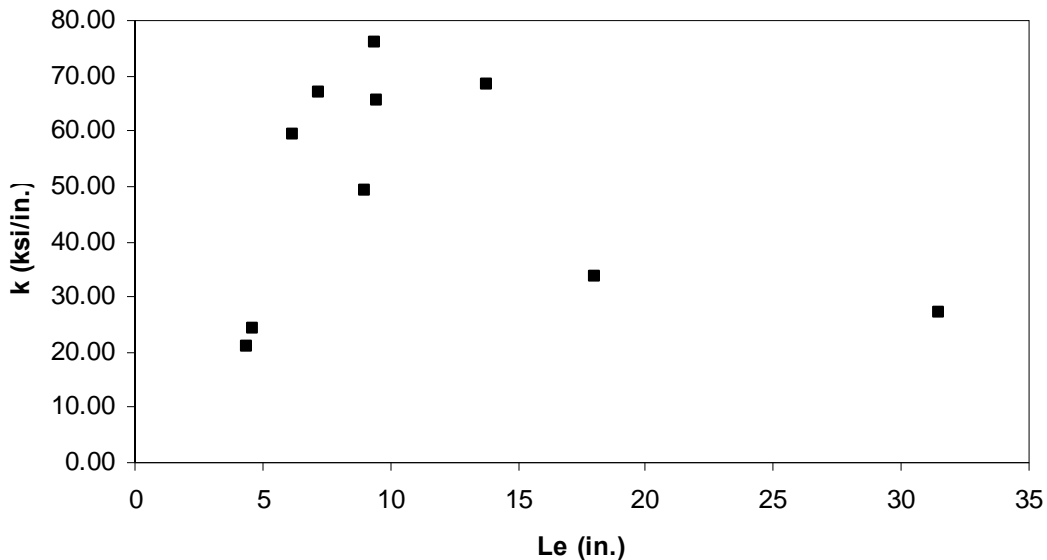


Figure 6.3: Local bond stiffnesses

The bond stiffness of very short-embedment length tests was low because the unconfined region appears to have been less stiff than the confined region, probably because of micro-cracks in the grout. The longest two tests also had much lower bond stiffnesses. While the length of the test should have been accounted for in the conversion from the average stiffness (K) to the calculated local stiffness (k), the low stiffnesses for these two tests may have been due to nonlinearities not expressed in the linear model.

From the remaining tests, the bond stiffness of a #18 bar was taken as 65 ksi/in. The bond models discussed below assumed that the bond stiffness is linearly related to the bar diameter. Because the perimeter is also linearly related to the bar diameter, the λ value for any size bar is the same.

Table 6.2 gives the λ , λL_e , and β values for each of the tested specimens, given the assumed bond stiffness of 65 ksi/in.

Table 6.2: Bond stiffnesses and slip fractions

Test	λ (1/in.)	λL_e	β
08C08	0.063	0.50	0.89
08N08	0.063	0.50	0.89
10F04	0.063	0.40	0.93
10N04	0.063	0.27	0.97
10N06	0.063	0.48	0.89
10N08	0.063	0.61	0.84
14N08	0.063	0.83	0.73
18F02	0.063	0.29	0.96
18F03	0.063	0.45	0.91
18F04	0.063	0.59	0.85
18N02	0.063	0.28	0.96
18N03	0.063	0.39	0.93
18N04	0.063	0.60	0.84
18N06	0.063	0.87	0.71
18N08	0.063	1.13	0.58
18N14	0.063	1.99	0.27
18S04	0.063	0.57	0.86

The linear model predicted that even the longer embedment length tests would have relatively large β values, implying that the slip and the bond stress were relatively constant along the embedded length. For example, specimen 18N08 had a β of 58 percent. The back-end slip can be estimated by multiplying the calculated slip fraction by the front-end slip. For test 18N08, this calculated back-end slip, based on a bond stiffness of 65 ksi/in., was compared with the measured back-end slip in Figure 6.4.

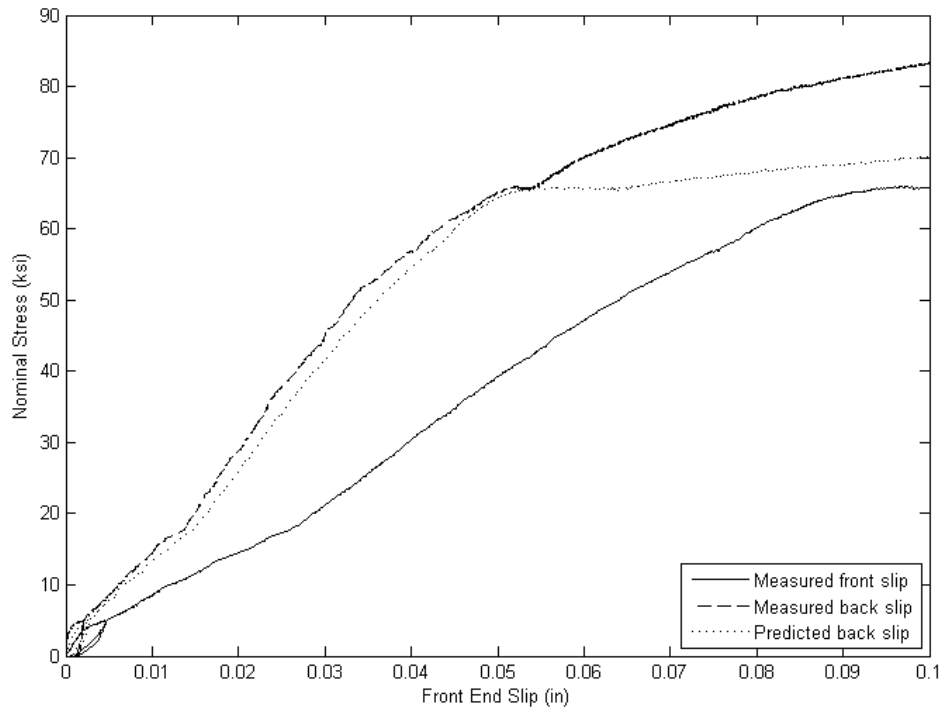


Figure 6.4: Back-end slip for test 18N08

The predicted slip at any given stress was somewhat higher than measured, suggesting that the grout was stiffer than 65 ksi/in. The close agreement of the back-end slip in the elastic range suggests that the bond stiffness value is appropriate for use in specimens with long embedment lengths. However, after yield, the predicted back slips become much too high, since the stiffness of the bar decreases relative to the grout stiffness, increasing the fraction of the slip due to bar deformation and reducing the fraction due to rigid body motion. Note that while this procedure accurately predicts the ratio between the measured front-end and back-end slips, it is less accurate at predicting the absolute values of these quantities.

6.2 NONLINEAR BOND MODEL

Nonlinear bond-slip constitutive models for both the unconfined and confined regions of the embedment length were developed for use in the numerical modeling of the system.

6.2.1 Key Variables

Several variables and system properties interact to determine the local bond stress at a point on the bar. System properties that may affect the bond stress include grout strength and bar geometry. Possible variables that can change along the length of the bar include slip and bar strain.

As noted in Section 5.4, variations in geometric properties, such as bar size and relative rib area, did not affect the test results sufficiently to determine a specific relationship between these quantities and the local bond stress. Although the grout strength did not vary significantly among the tests, the unconfined and confined bond models were normalized by the square root of the grout strength in ksi.

As discussed in Section 5.5, the effect of yielding independent of the increased slip could not be determined. The local bar strain was therefore not included in the bond model. The remaining local variable was slip. The average bond stress and the slip at the center of the bonded region were used to develop the bond model, as further discussed below. Slips were normalized by the bar diameter, as done explicitly by some researchers (Martin 2006) and implicitly by others (Eligehausen 1983).

The form of the bond models is then:

$$\tau(x) = f \left(\frac{\text{slip}}{d_b} \right) \cdot \sqrt{f'_g} \quad 6.14$$

6.2.2 Unconfined Model

The bond-slip model for the unconfined region was taken from the response of test 18N02, shown in Figure 6.5. Nearly the full embedded length in test 18N02 was within the 45-degree unconfined region. The remaining length was smooth steel without lugs and so did not form the grout-and-bar shearing cylinder that was characteristic of the confined region.

The slip for the model was taken as the slip at the center of the embedded length. This slip was calculated by assuming a linear strain distribution in the embedded length. The strain was known at the front end from the strain gages and was zero at the back end. The strain at the center of the bar could be estimated with Equation 6.15:

$$u_{mid} = u_{surface} - \frac{\epsilon_{cone} + \epsilon_{surface}}{2} L_{unconfined} \quad 6.15$$

where

$$\varepsilon_{cone} = \varepsilon_{surface} - \frac{P_{unconfined}}{EA} \quad 6.16$$

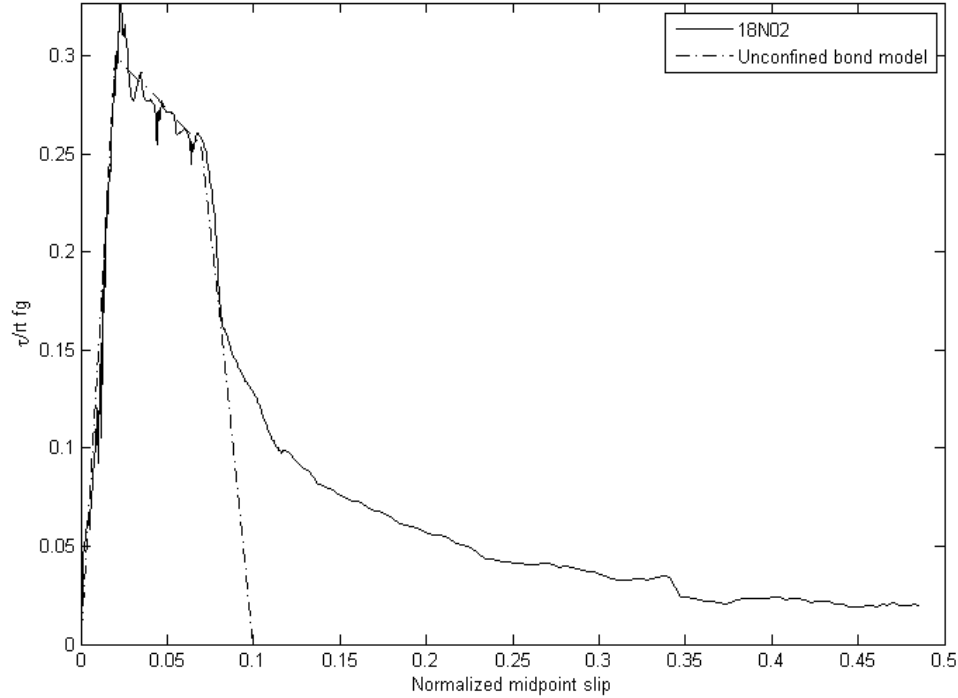


Figure 6.5: Unconfined bond model

The piecewise linear function that defines this bond model is given in Appendix D. The model is shown in comparison to test 18N02 in Figure 6.7.

The constitutive model differs from the measured values in that the model has been smoothed near the peak load, and the bond stress at large slips has been set to zero.

6.2.3 Confined Model

Determining the bond-slip relationship for the confined region was complicated by the fact that no test included only a confined region. Instead, the embedded length and measured force had to be reduced by the length and force accounted for by the unconfined region.

$$\tau_{confined} = \frac{P - P_{unconfined}}{\Pi(L_e - L_{unconfined})} \quad 6.17$$

The length of the unconfined region was assumed to be defined by a cone extending from the duct to the bar, as shown in Figure 5.1. The unconfined length was given by Equation 6.18.

$$L_{unconfined} = \frac{(d_{duct} - d_b)}{2} \tan(\theta) \quad 6.18$$

The location of the lugs strongly influenced the cone angle in any particular test, and 45 degrees was chosen as a rough average of the observed cone angle. More accurate analysis of the cone length was not warranted because of the inherent variability of cracking among and within the test specimens.

The force accounted for by the unconfined region was taken as the force on specimen 18N02 at the same slip. By subtracting this force, only the force resisted by the confined region was counted for calculating the confined bond stress.

$$P_{unconfined}(u) = P_{18N02}(u) \quad 6.19$$

Just as the slip at the center of the embedded length was used for the unconfined model, the slip at the center of the confined region was calculated for use in the confined bond model. The assumed strain and slip distributions are shown in Figure 6.6. Although the strain distribution through the cone was unknown, a bar force at the base of the cone was calculated as above. This bar force was converted to a bar strain, and a linear strain profile was assumed through the unconfined region. From this strain at the base of the cone, a second linear strain profile was assumed to exist through the confined region. The modified slip is given by Equation 6.20.

$$u_{confined} = u_{surface} - \frac{(\varepsilon_{air} + \varepsilon_{cone})}{2} L_{unconfined} - \frac{3}{8} \varepsilon_{cone} (L_e - L_{unconfined}) \quad 6.20$$

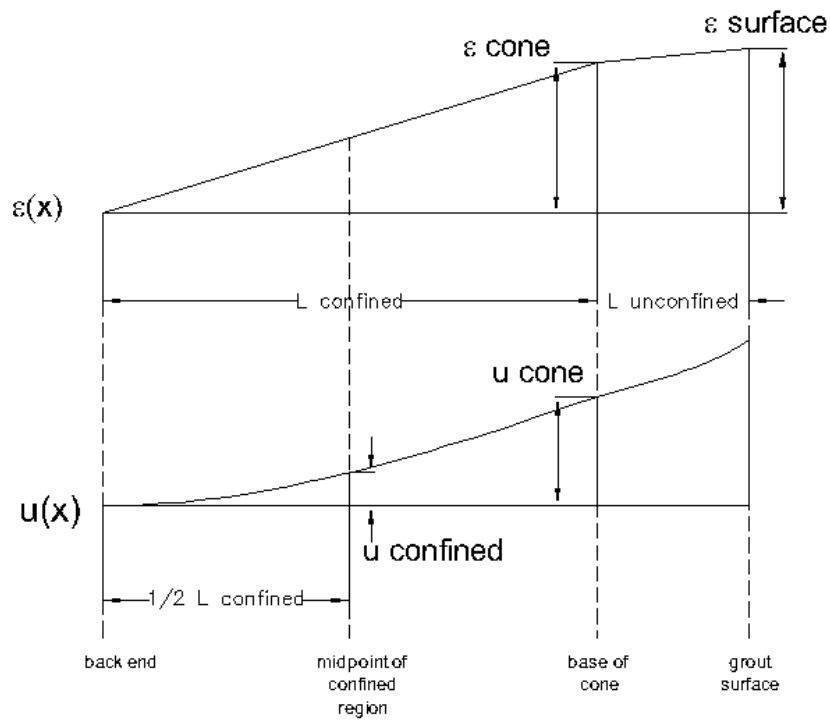


Figure 6.6: Assumed strain and slip distributions

The confined bond model, shown in Figure 6.7, was based on the response of specimen 18N04. This specimen had several desirable characteristics: elastic steel response, relatively long confined region, and unreinforced grout. The model is represented as a piecewise function given in Appendix D.

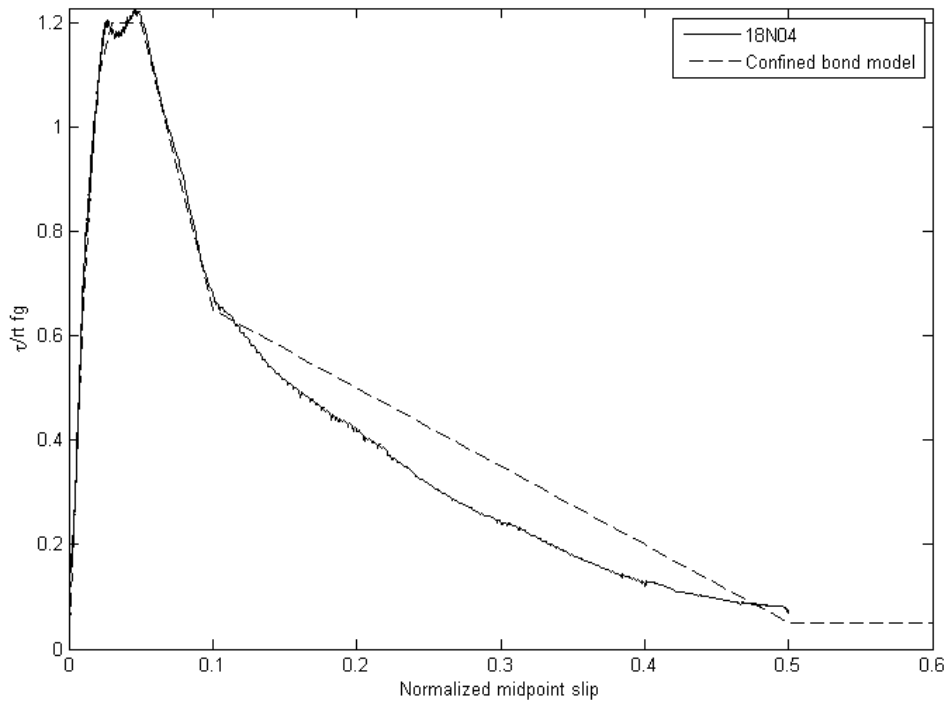


Figure 6.7: Confined bond model

6.2.4 Comparison to Other Bond Models

Figure 6.8 compares the bond model developed here with bond models developed by other researchers. Each model is shown for a #18 bar in 8-ksi grout to allow comparison of models with different forms. The overall shape is similar to the bond model presented by Eligehausen for bars embedded in concrete, although the stresses obtained are higher (Eligehausen 1983). The proposed bond models do not reach the very high stresses achieved by Raynor's model, which was developed for #8 bars in high-strength grout (Raynor 2000).

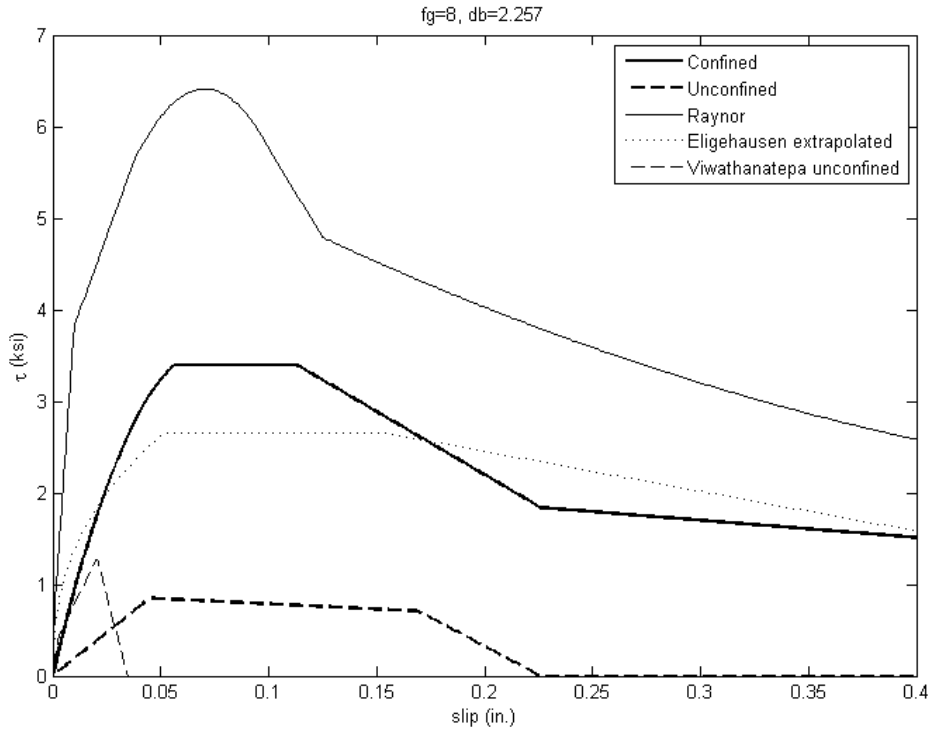


Figure 6.8: Bond model comparison

In Figure 6.8, Eligehausen's model has been extrapolated from his original model, on the basis of #8 bars in 4350-psi concrete, to the larger bar size and stronger compressive strengths utilized in this series of tests. The increase in bar size increases the slip values by 30 percent, the maximum suggested by Eligehausen, and the increase in grout strength increases the bond stress values as $\sqrt{f'_g}$ (Eligehausen 1983).

6.3 NONLINEAR ANALYSIS METHOD

A finite element analysis was needed to simulate the response of a test specimen. The model consists of a series of nonlinear 1-D bar elements attached to nonlinear bond springs, as shown in Figure 6.9. The bond springs in the confined region were defined by the nonlinear confined bond-slip model in Figure 6.7, and the bond springs in the unconfined region were defined by the nonlinear unconfined bond-slip model in Figure 6.5.

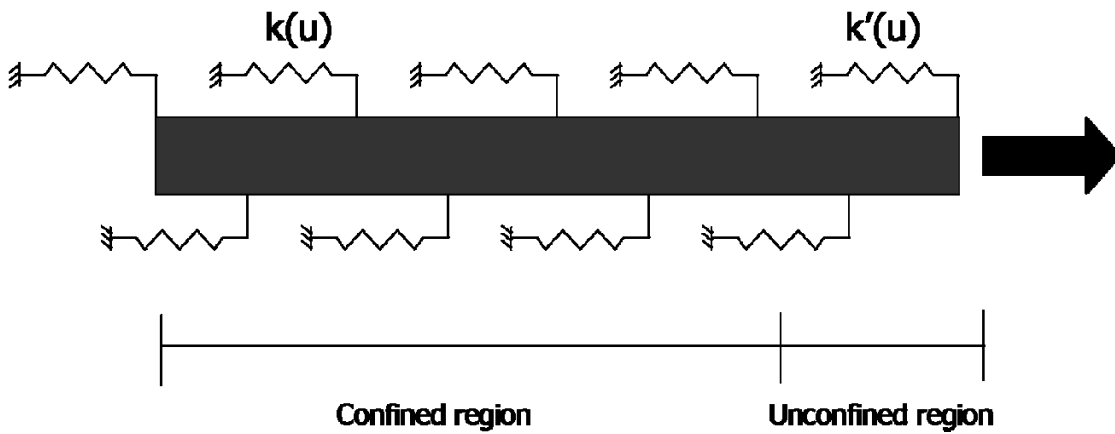


Figure 6.9: Schematic of the nonlinear model

The steel constitutive model is shown in Figure 6.10. The model is based on the model developed by Raynor, and the code is included in Appendix D. Nominal bar dimensions were used to calibrate the constitutive models and run the analyses.

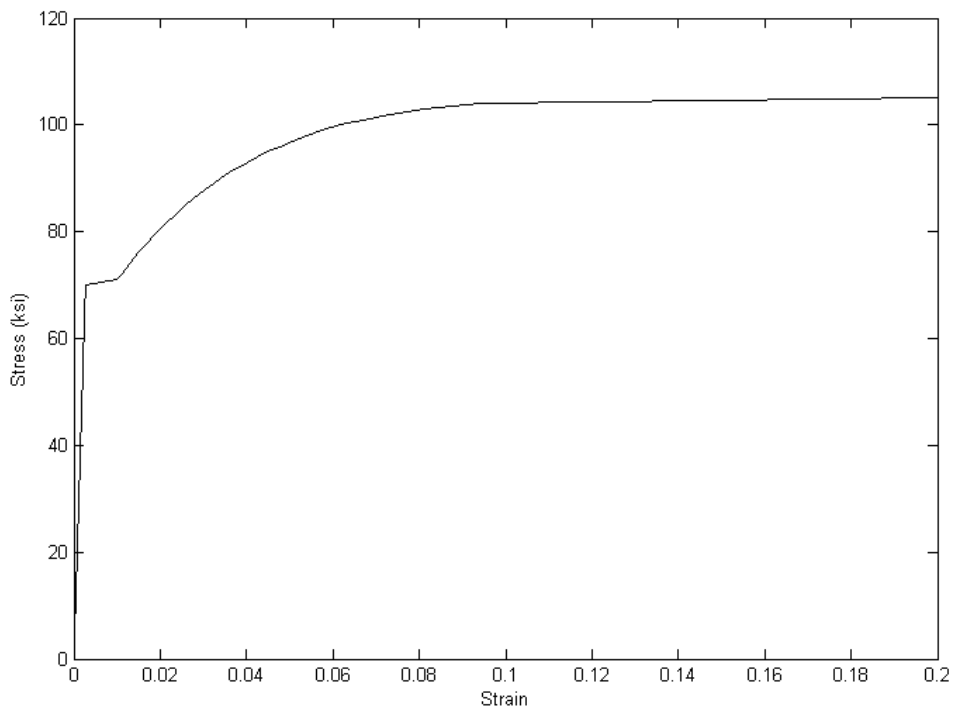


Figure 6.10: Steel constitutive model

The chain configuration allows for a special method of solution to be used for the analysis. For any given back-end slip, the bond stresses, bar stresses, and bar strains can be calculated by working forward. This will result in a force at the front end of the bar, as well as distributions of stresses and strains along the bar. By incrementing the back-end slip, the full force-displacement curve can be computed. Specific loads can be taken from this curve by interpolation or can be computed by iteration.

Taking the back-end slip as the incremented variable greatly simplifies the solution procedure. With the back-end slip assumed, the stress, strain, and slip of the bar are known at this location. Given these quantities, the bond stress over the next element can be calculated from the bond model. Next, the bar stress in the element is calculated from equilibrium. From the bar stress, the bar strain is calculated by using a one-sided cyclic steel model. The bar strain is then used to calculate the slip at the next node. This procedure progresses until the surface of the grout is reached, and the front-end slip and stress are calculated. The code for this procedure is given in Appendix D.

6.4 RESULTS OF THE NONLINEAR MODEL

The nonlinear model was used to estimate the peak load for each specimen and to simulate the force-displacement behavior of each specimen. Results for both estimates are provided below.

6.4.1 Peak Loads by Test

Figure 6.11 compares the peak load, expressed as a nominal bar stress, predicted by the model with the peak bar stress achieved in the test. The 1:1 line is shown for reference. Values to the right of this line were overpredicted by the model, values to the left were underpredicted.

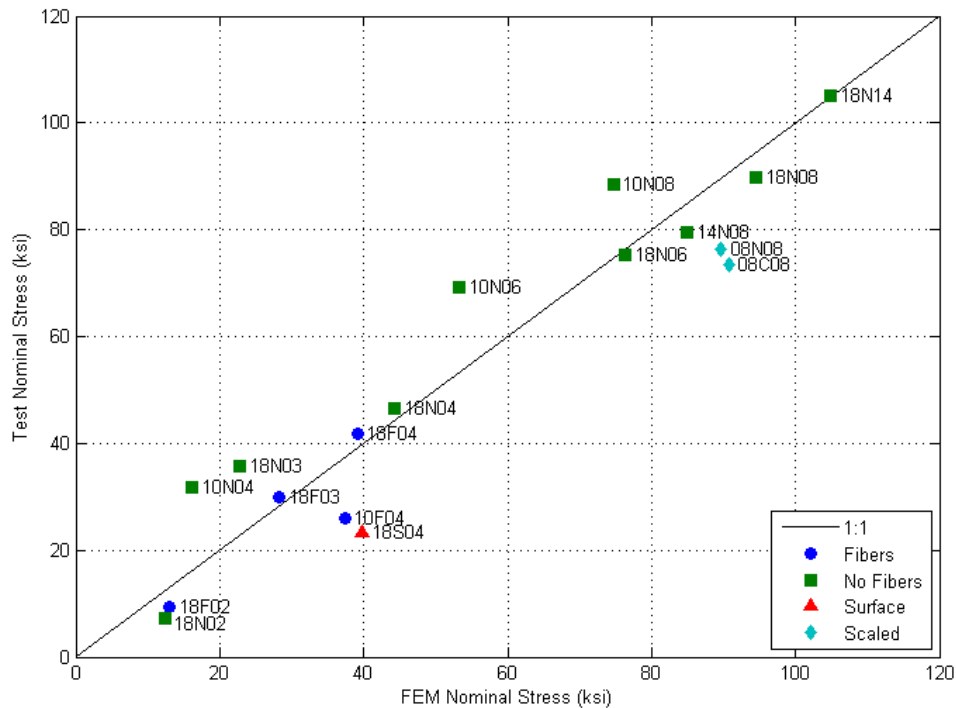


Figure 6.11: Peak loads from FEM and experiments

Overall, the model accurately predicted the bar stresses reached during the test. The root mean squared error of the peak load for all tests was 8.8 ksi, or 13 percent of the yield strength. This value does not include tests 18S04 and 08C08. These tests failed by concrete splitting, which was not included in the model. The root mean squared error of the peak load for the #18 tests was 5.2 ksi, or 7.4 percent of the yield strength.

The predicted peak values for the shortest tests, 18N02 and 18F02, were overpredicted even though the unconfined model was determined directly from test 18N02. This anomaly resulted from the configuration of the lugs in the actual tests. In each test, a section of the embedded bar below the cone did not have any lugs. This section without lugs was unlikely to develop significant stress in the actual test. However, because the location of the lugs was not included in the model, the model assigned bond stresses from the confined model to the section.

The model underestimated the maximum stress for most of the tests on #10 bars. In contrast, test 10F04 was overpredicted; the peak average bond stress reached during the test was lower than typical, which suggests that the test result was unusual. The

prediction for the single test on a #14 bar was slightly larger than the test value. The evidence for a bar size effect on the bond model is thus mixed. Further testing may be needed to determine the effect, if any, of bar size on local bond stress.

6.4.2 Force-Displacement Behavior

Simulating the force-displacement behavior of the test specimens was more challenging than simulating the peak load alone. The short-embedment length tests resulted in a predicted force-displacement curve that mimicked the bond model itself. Very long embedment lengths, including test 18N14, primarily depended on the steel model. More interesting results came from simulating the moderately long-embedment length tests. The estimated stress-displacement curve for specimen 18N06 is shown along with the test result in Figure 6.12. Comparisons for each test are shown in Appendix E.

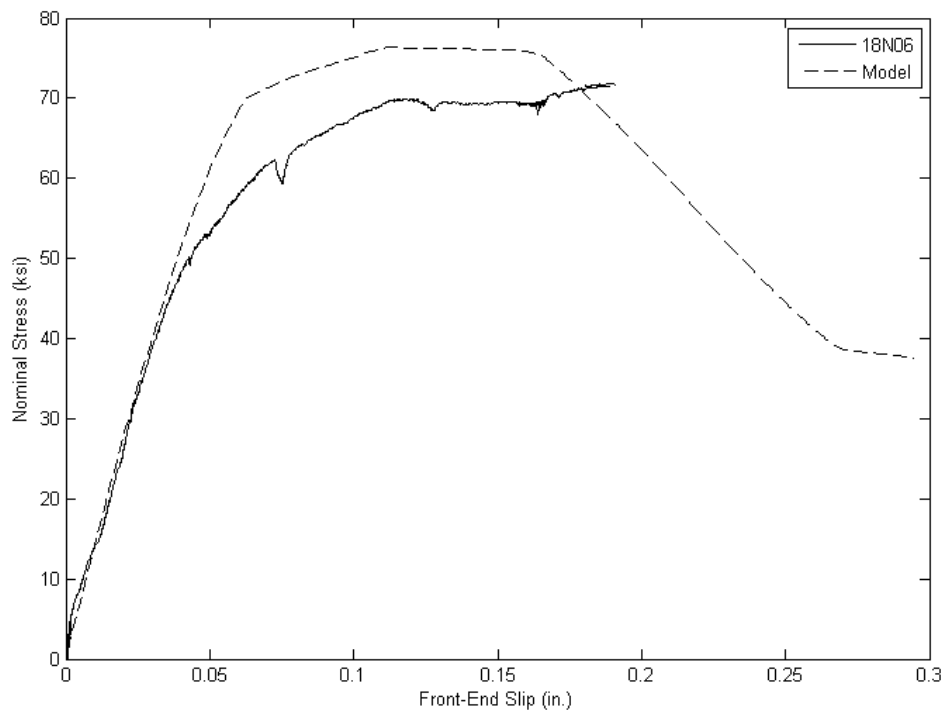


Figure 6.12: Test and FEM force-displacement comparison

In Figure 6.12, the initial stiffness of the model and test agree well, but the test produced an increase in displacement before yield that is not shown in the model. The peak force is well predicted, although the displacement measurements for test 18N06 became unreliable before the peak load was reached.

6.4.3 Bond Stress Distribution

For each test, the bond stress distribution at the peak load was computed by using the nonlinear model. For the short-embedment length tests, the bond stress is uniform through the confined region at the peak load. The entire length of the confined region was on the plateau of maximum bond stress. For the longer embedment length tests, other distributions formed. The bond stress distributions at the peak load for tests 18N04, 18N08 and 18N14 are shown in Figure 6.13. The location axis runs from the front end of the bar at zero to the back end of the bar at 9, 18 and 31.5 in., respectively.

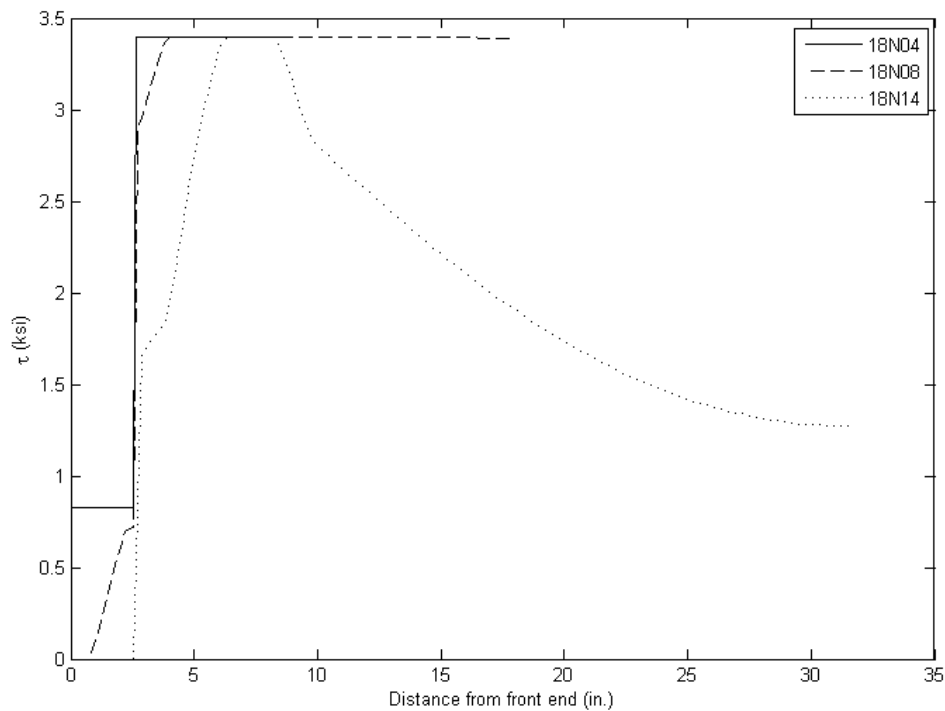


Figure 6.13: Bond stress distributions

In Figure 6.13, the difference between the confined and unconfined bond models is apparent in the sharp drop in bond stress around 3 inches of depth. In reality, this difference in bond stress does not occur discretely but is related to the location relative to the grout surface, the imposed slip, and bond demand. This complex relationship was not included in the nonlinear model.

The model showed that in test 18N08 much of the bond stress at the peak load, which reached a bar stress of about 90 ksi in the test and the model, came from the back end of the bar. To develop these high bond stresses, the back end of the bar must experience slips large enough to bring the back end of the bar nearly to the plateau of maximum bond stress.

At the peak load in test 18N14, the back end of the bar moved less, resulting in lower bond stresses at the back end of the bar. From there, the bond stress increased to a peak at a point near the midpoint of the embedded length. After this peak, the increase in bar slip caused the bond stress to decrease. This process continued until the front end of the bar had moved so far through the grout that it provided little bond resistance.

The slip distributions at the peak load for tests 18N04, 18N08, and 18N14 are shown in Figure 6.14. Again, this plot shows that the slips for the short-embedment length tests did not vary greatly along the length of the bar, so that the bond stress was relatively uniform along the length. The longer embedment lengths have back-end slips on the ascending branch of the bond model, with front-end slips that have passed the peak of the bond model.

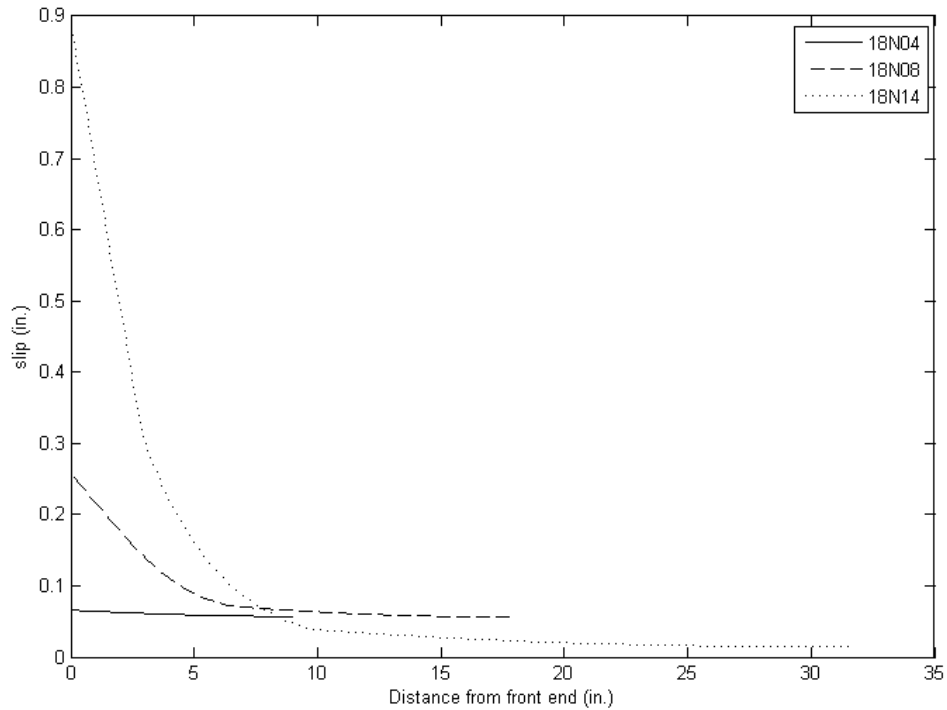


Figure 6.14: Slip distributions

6.4.4 Development Length

The FEM code was also run with the nominal bar geometry of a #18 and grout strengths of 8 ksi in order to predict the necessary embedment length for bar yield and bar fracture. The yield stress of the reinforcing bar for these analyses was assumed to be 70 ksi, representing the typical overstrength of the tested reinforcing bars. The results from this analysis are plotted in Figure 6.15. The model was implemented for embedment lengths that include an unconfined region, shown by the solid line, and for embedded bars that are entirely in the confined region, shown by the dashed line. The test results are also shown for comparison.

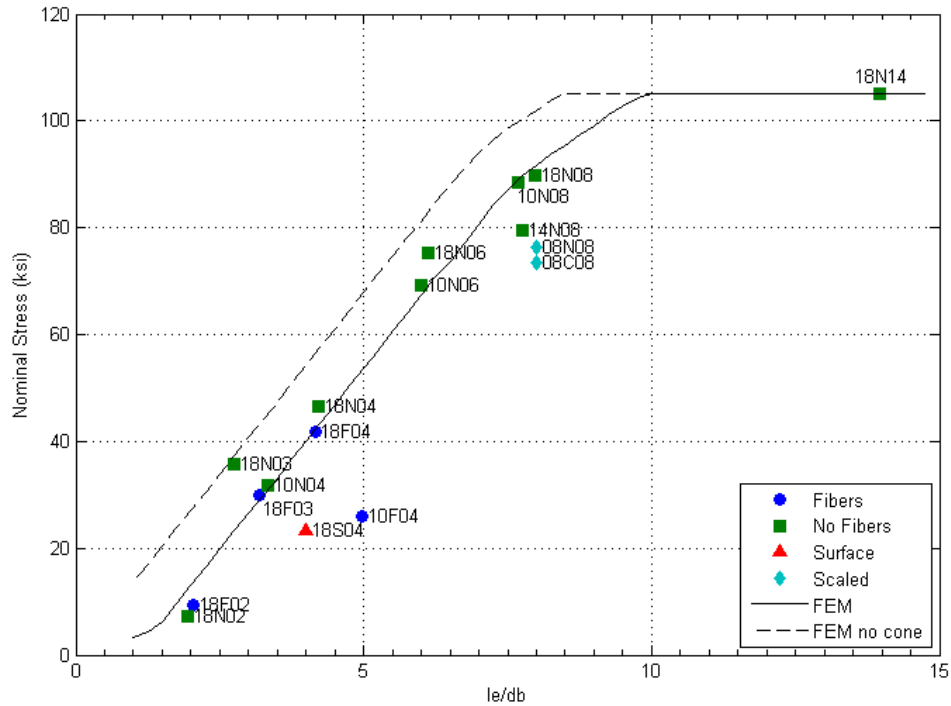


Figure 6.15: FEM development length predictions

The solid line represents the relationship between embedded length and peak bar stress when the embedded region contains an unconfined region similar in length to the cones observed in the tests. This assumes that the bar and duct size are similar to those tested here; that is #18 bars in 8-in.-diameter ducts.

For embedded lengths that include the weaker unconfined region, the model suggests that for a #18 bar in 8-ksi grout, the nominal yield stress (60 ksi) can be achieved in 5.5 bar diameters and fracture (105 ksi) in 10 bar diameters. While only valid for monotonic loading, these lengths are significantly shorter than the current development lengths given by the ACI and AASHTO codes.

The ACI code expressions are based on developing a bar stress of 125 percent of nominal yield, 75 ksi. The code appears to ensure this by finding the development length for 60 ksi and multiplying this length by 125 percent (Orangun 1977, Jirsa 1979). This method works well if the relationship between embedment length and peak stress is linear. The test results and FEM modeling appear to confirm that this relationship is nearly linear in this range, although this finding may be a result of the yield stress of the

tested bars being between 65 and 70 ksi. The model and tests show that a stress of 75 ksi can be developed in 7 bar diameters. This length includes the 45-degree unconfined region.

The dashed line would be applicable to situations without an unconfined region. An implementation that avoids the development of a cone would have a shorter development length, as the remaining bonded length would be surrounded by confined grout. This can be achieved by intentionally debonding the bar near the joint interface of a column-to-cap-beam connection, in the region that would otherwise be unconfined. Because structural performance benefits could potentially result from debonding the bar in this region, this may be advantageous. For these types of embedment, a bar stress of 75 ksi can be achieved in 6 bar diameters.

The development lengths discussed here are for static loading. Cyclic tests were not carried out because of the difficulty of cyclically loading the large bars. For smaller bars, Raynor suggested that the cyclic development length is 40 percent longer than the monotonic development length. Increasing the development lengths for the large bars by 50 percent for cyclic loading should be conservative. The ACI and AASHTO codes currently increase monotonic development lengths by 25 percent to account for cyclic loading.

CHAPTER 7: CONCLUSIONS

7.1 CONCLUSIONS

This study supports the following conclusions regarding the necessary anchorage length for bars in grouted ducts:

- Reinforcing bars up to #18 grouted into ducts can be developed to yield in 6 bar diameters and to fracture in 14 bar diameters. These lengths are shorter than the depth available in typical cap beams. Therefore, the use of large bars for grouted connections is possible.
- There was no clear relationship between bar size and peak bond stress.
- The scaled pullout tests, conducted by using the materials selected for the bars and ducts in the scaled column-to-beam tests, produced strengths and stiffnesses similar to those of the equivalent full-scale tests.
- The nonlinear model accurately predicted the peak resistance of the monotonic pullout tests. The root mean square error in the predicted bar tensile stress for all tests that resulted in bar pullout was 8.8 ksi. For the tests on #18 bars, the root mean square error was 5.2 ksi.
- Modeling showed that the #18 bars could have been developed to yield in 5.5 bar diameters and to fracture in 10 bar diameters. These models included the weaker unconfined region as part of the development length.
- Current code expressions require that a bar be loaded to 125 percent of its nominal yield stress to be considered anchored. Modeling showed that the #18 bars could be developed to 125 percent of the nominal yield stress (75 ksi) in 7 bar diameters for embedment lengths that include an unconfined region.
- The linear and nonlinear models showed that reinforcing bars developed to yield may move significantly over the entire embedded length. For example, modeling showed that about three-quarters of the slip at the live end of a bar embedded $6d_b$ in grout comes from rigid-body motion of the bar.
- High compressive strengths can be obtained from commercially available grouts at early ages. Compressive strengths of about 8 ksi were consistently reached at 5

days. The peak bond stress was not clearly related to the grout compressive stress.

- Peak bond stresses of $1.3\sqrt{f'_g}$ ksi ($41\sqrt{f'_g}$ psi) were achieved in the short-embedment length tests.
- The presence of fibers did not improve monotonic pullout resistance and decreased the compressive strength of the grout.

7.2 IMPLEMENTATION RECOMMENDATIONS

The results of this study can be applied to the implementation of the proposed precast column and cap beam system.

- The depth available in typical cap beams is much greater than the monotonic development length for #18 bars (42 in. in comparison to about 16 in.). The cap beam is sufficiently deep to accommodate a development length with a 50 percent increase for cyclic loading and an 8-bar-diameter debonded length. Debonding the reinforcing bars in the grouted duct may be beneficial because of the reduction of the strain concentration at the joint.
- The results of this study are applicable to grout strengths of at least 8 ksi. The peak bond stress was not very sensitive to the grout strength, and grout strengths from 6.5 to 8 ksi are probably acceptable.
- All tests were conducted in 8-in. corrugated steel pipes that provided confinement for the grout. The large deformations and large diameter increased resistance to duct pullout. Other ducts may need to be investigated for duct pullout. Duct pullout was studied in only three tests, and did not include group effects.

7.3 SUGGESTIONS FOR FURTHER RESEARCH

This research could be extended by studying the following areas:

- Cyclic loading. While the loading connections necessary for cyclic tests are complex, the suggested increase from the monotonic to the cyclic development length may be overly conservative.
- Early grout strengths. Very young (1 and 2 day) grout was not tested for compressive strength or bond strength. These strengths are certainly lower than

the tested values but are critical for determining the minimum time between the grouting operation and subsequent construction operation.

REFERENCES

- AASHTO (2005). "LRFD Bridge Design Specifications," 4th ed., American Association of State Highway and Transportation Officials, Washington, DC.
- ACI Committee 318 (2005). "Building Code Requirements for Structural Concrete (ACI 318-05) and Commentary (ACI 318R-05)," American Concrete Institute, Farmington Hills, MI
- ACI Committee 408 (2001). "Splice and Development Length of High Relative Rib Area Reinforcing Bars in Tension (408.3-01) and Commentary (408.3R-01)," American Concrete Institute, Farmington Hills, MI
- Brenes, F., Wood, S., and Kreger, M. (2006). "Anchorage Requirements for Grouted Vertical-Duct Connectors in Precast Bent Cap Systems: A Summary," Center For Transportation Research, Project Summary Report 0-4176, Austin, TX
- Darwin, D., and Salamizavaregh, S. (1993). "Bond Strength of Grouted Reinforcing Bars," Structural Engineering and Engineering Materials Report no. SM 32, University of Kansas Center for Research, Inc., Lawrence, KS
- Eligehausen, R., Popov, E., and Bertero, V. (1983). "Local Bond Stress-Slip Relationships of Deformed Bars Under Generalized Excitations," Earthquake Engineering Research Center, Report UCB/EERC-83/23, University of California, Berkeley, CA
- Jirsa, J., Lutz, L., and Gergely, P. (1979). "Rationale for Suggested Development, Splice, and Standard Hook Provisions for Deformed Bars in Tension," Concrete International, July 1979, p 47-61
- Martin, J. (2006). "An Experimental Investigation of Bond in Reinforced Concrete," Master's thesis, University of Washington, Seattle, WA
- Nakaki, S., Stanton, J., Sritharan, S. (1999). "Overview of the PRESSSS five-story precast test building," PCI Journal, v 44 n2, Mar-Apr 1999, p 26-39
- Orangun, C., Jirsa, J., and Breen, J. (1977). "A Reevaluation of Test Data on Development Length and Splices," ACI Journal, V. 74 n. 3, p 114-122
- Palmieri, L., Saqan, E., French, C., and Kreger, M. (1996). "Ductile Connections for Precast Concrete Frame Systems," Mete A. Sozen Symposium, ACI SP162-13, p 313-355

- Priestley, M.J.N., Sritharan, S., Conley, J., Pampanin, S. (1999). "Preliminary results and conclusions from the PRESS five-story precast concrete test building," *PCI Journal*, V. 44, n. 6, Nov 1999, p 42-67
- Raynor, D. (2000). "Bond Assessment of Hybrid Frame Continuity Reinforcement," Master's thesis, University of Washington, Seattle, WA
- Sritharan, S. (2005). "Strut-and-Tie Analysis of Bridge Tee Joints Subjected to Seismic Actions," *Journal of Structural Engineering*, 131(9) p 1321-1333
- Viwathanatepa, S., Popov, E., and Bertero, V. (1979). "Effects of Generalized Loadings on Bond of Reinforcing Bars Embedded in Confined Concrete Blocks," Earthquake Engineering Research Center, Report UCB/EERC-79/22, University of California, Berkeley, CA
- Wacker, J., Hieber, D., Stanton, J., and Eberhard, M. (2005). "Design of Precast Concrete Piers for Rapid Bridge Construction in Seismic Regions," Washington State Transportation Center Report, Seattle, WA

APPENDIX A: SYSTEM TABLE AND SCHEMATIC DRAWINGS

The tables printed here were developed by Kari Gunnarsson. Each system was evaluated on the basis of factors encompassing fabrication, construction, and structural behavior. Points were assigned, with 1 being the best and 5 being the worst. Low point totals represent preferred systems.

Table A.1: Fabrication Factors

	Forming	Steel and Duct Placement	Extra Materials	Points
Ducts	1	3 Maintain tolerances, ½ in. bars and ducts	2 Ducts	6
Large Opening	2 Circular opening. Corrugated Surfaces.	1	1 None	4
6 #18	1	2	2 #18 bars and ducts	5
Solid Column (RC)	2 Circular opening. Corrugated Surfaces.	1	1 None	4
Solid Column (PSC)	2 Circular opening. Corrugated Surfaces.	1	1 None	4
Concrete-Filled Tube	2 Tube projecting from column	1	3 Tube	6
Slotted column	4 Odd shapes / Blockouts	2 Congestion in column top	3 Bars in top of column	9

Table A.2: Construction Factors

	Speed of Construction	Temporary Erection Devices	Site Tolerance	Size of Crossbeam	Points
Ducts	3 Alignment of ducts and bars	3 Template and collar or shims	3 Col: +/- 1.5 in. Orientation of column (20 alignments).	2 6 ft x3.5 ft	11
Large Opening	3 Need fresh concrete on site	2 Collar	1 Col: +/- 1.5 in.	2 6 ft x3.5 ft	8
6 #18	1	1 Collar or shims	2 Col: +/- 1.5 in. Orientation of column (6 alignments).	1 5 ft x3.5 ft	5
Solid Column (RC)	1	2 Collar	1 Col: +/- 1.5 in.	3 6.5 ft x3.5 ft	7
Solid Column (PSC)	1	2 Collar	1 Col: +/- 1.5 in.	3 6.5 ft x3.5 ft	7
Concrete-Filled Tube	1	1 Collar or shims	1 Col: +/- 1.5 in.	1 5 ft x3.5 ft	4
Slotted column	2 Alignment of slots and bars	1 Collar or shims	2 Col: +/- 1.5 in. Orientation of column (2 alignments).	1 5 ft x3.5 ft	6

Table A.3: Structural Performance Factors

	Transfer of Vertical Load	Bar Location in Cross Beam	Ductility	Outstanding Structural Issues	Points
Ducts	1 Bearing	2 Sides (some in between ducts)	1 Similar to current bridges	1 None	5
Large Opening	2 Friction, use corrugated surfaces	2 Sides	1 Similar to current bridges	1 None	6
6 #18	1 Bearing	1 Evenly distributed	2 Splicing in inelastic region	2 Bond of #18 bars and ducts	6
Solid Column (RC)	2 Friction, use corrugated surfaces	2 Sides	1 Similar to current bridges	2 Transfer of crossbeam torsion	7
Solid Column (PSC)	2 Friction, use corrugated surfaces	2 Sides	1 Similar to or better than current bridges	3 Transfer of crossbeam torsion	8
Concrete-Filled Tube	1 Bearing	1 Sides (but more closer to middle)	3 Difficult splicing in inelastic region	3 Moment transfer. Size of tube	8
Slotted column	1 Bearing	1 Evenly distributed	2 Splicing in inelastic region	3 Group pullout bond failure	7

Table A.4: Total Points

	Fabrication	Construction	Structural	Total Points
Ducts	6	11	5	22
Large Opening	4	8	6	18
6 #18	5	5	6	16
Solid Column (RC)	4	7	7	18
Solid Column (PSC)	4	7	8	19
Concrete-Filled Tube	6	4	8	18
Slotted column	9	6	7	22

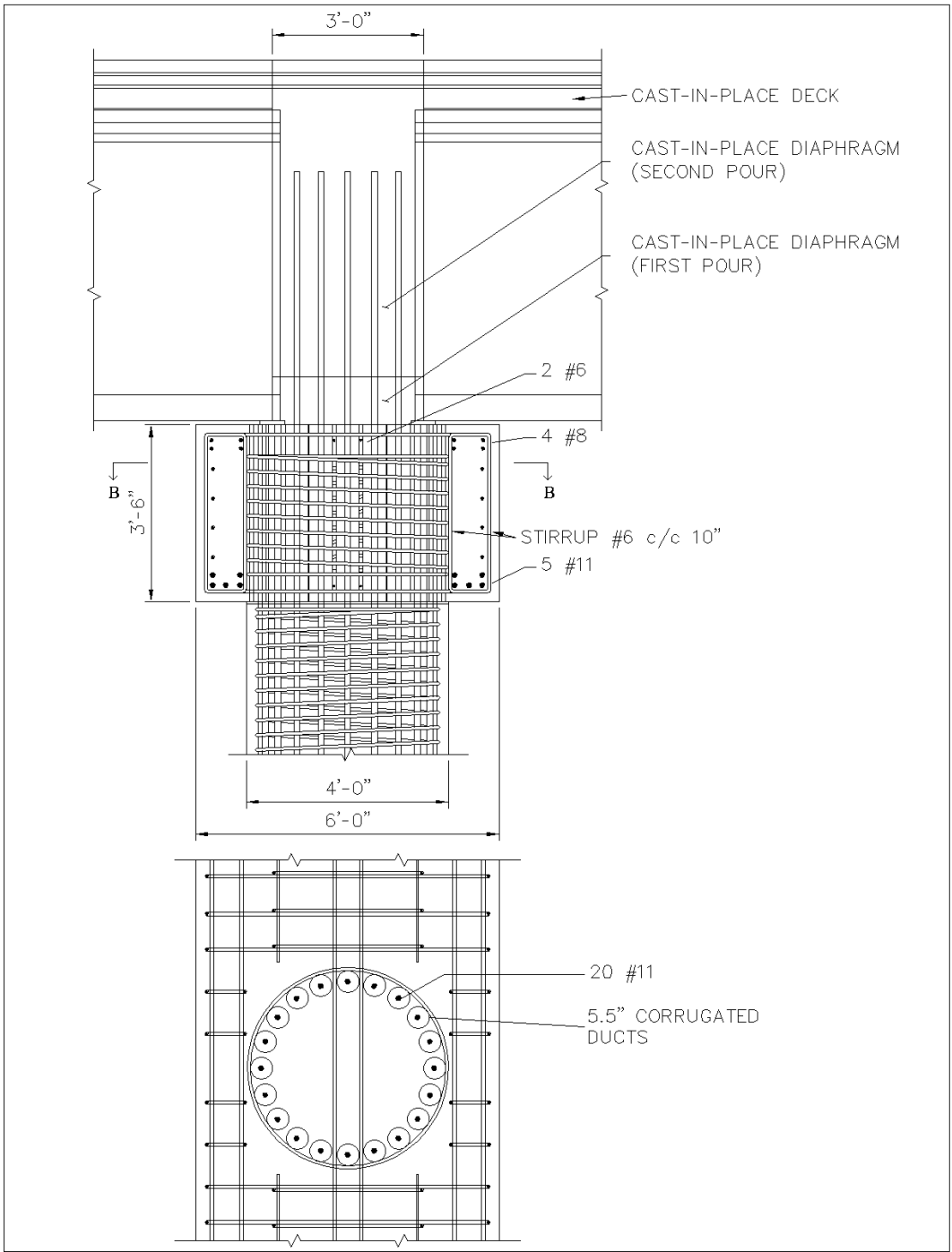


Figure A.1: Ducts system (20 #11)

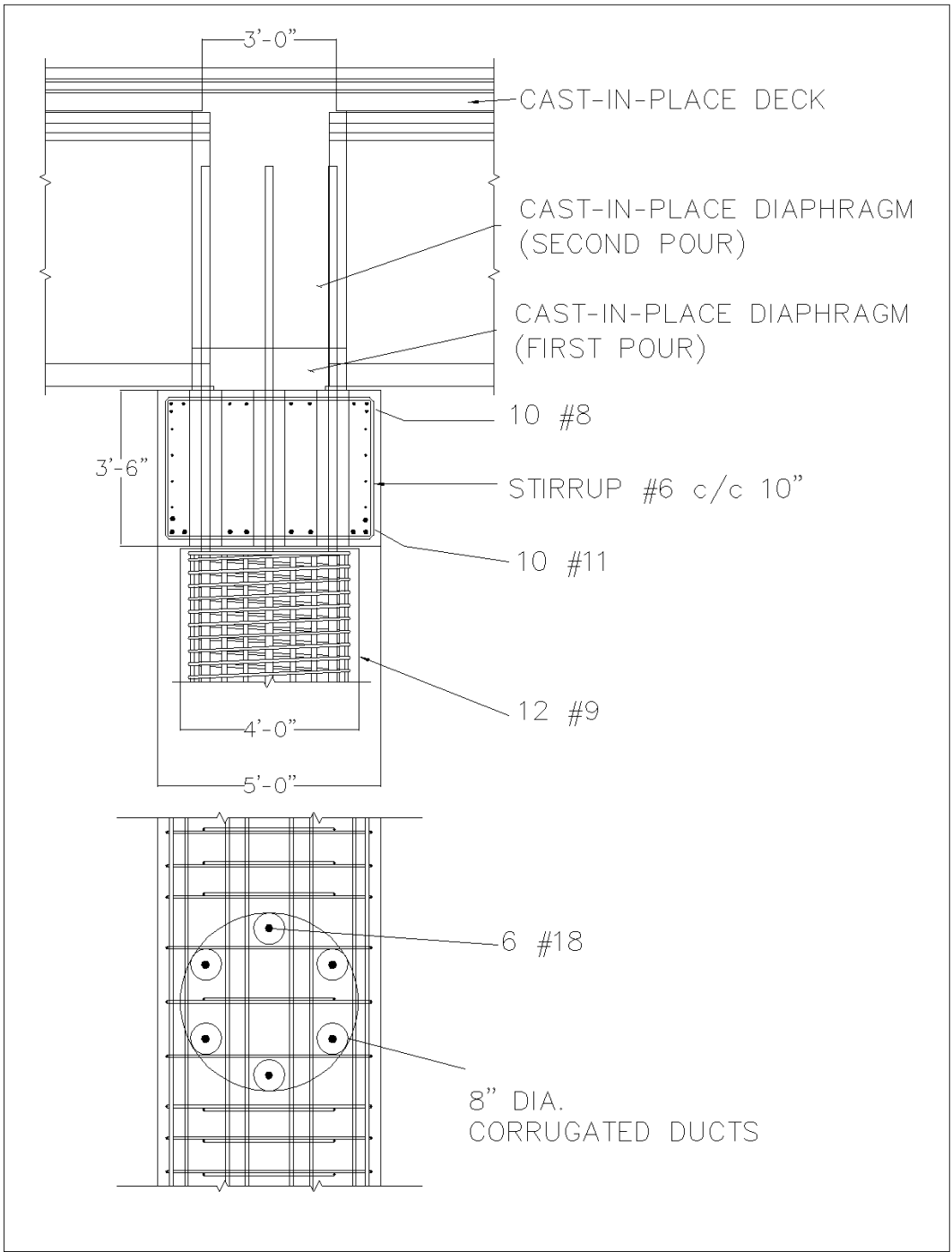


Figure A.2: Big bar system (6 #18)

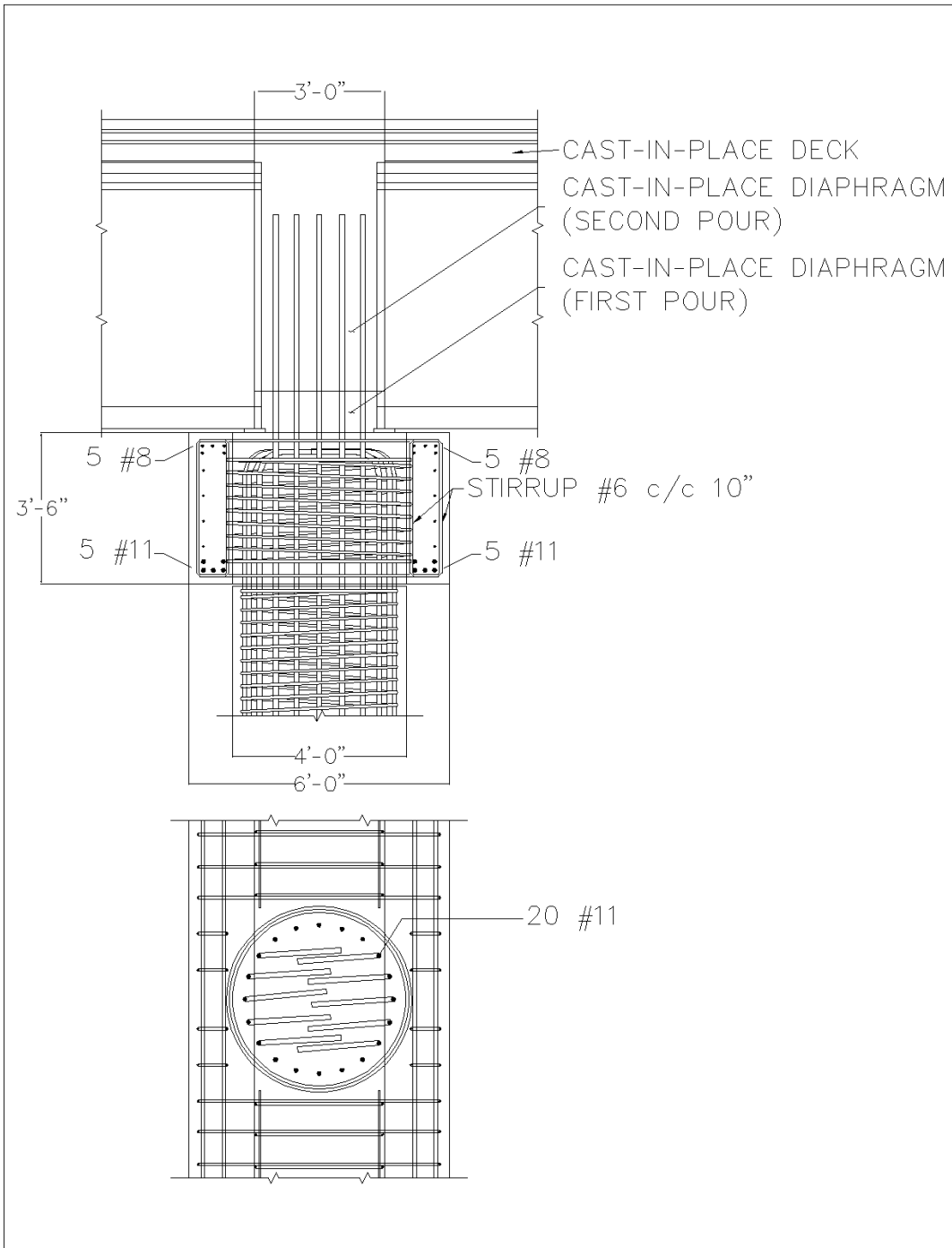


Figure A.3: Large opening system

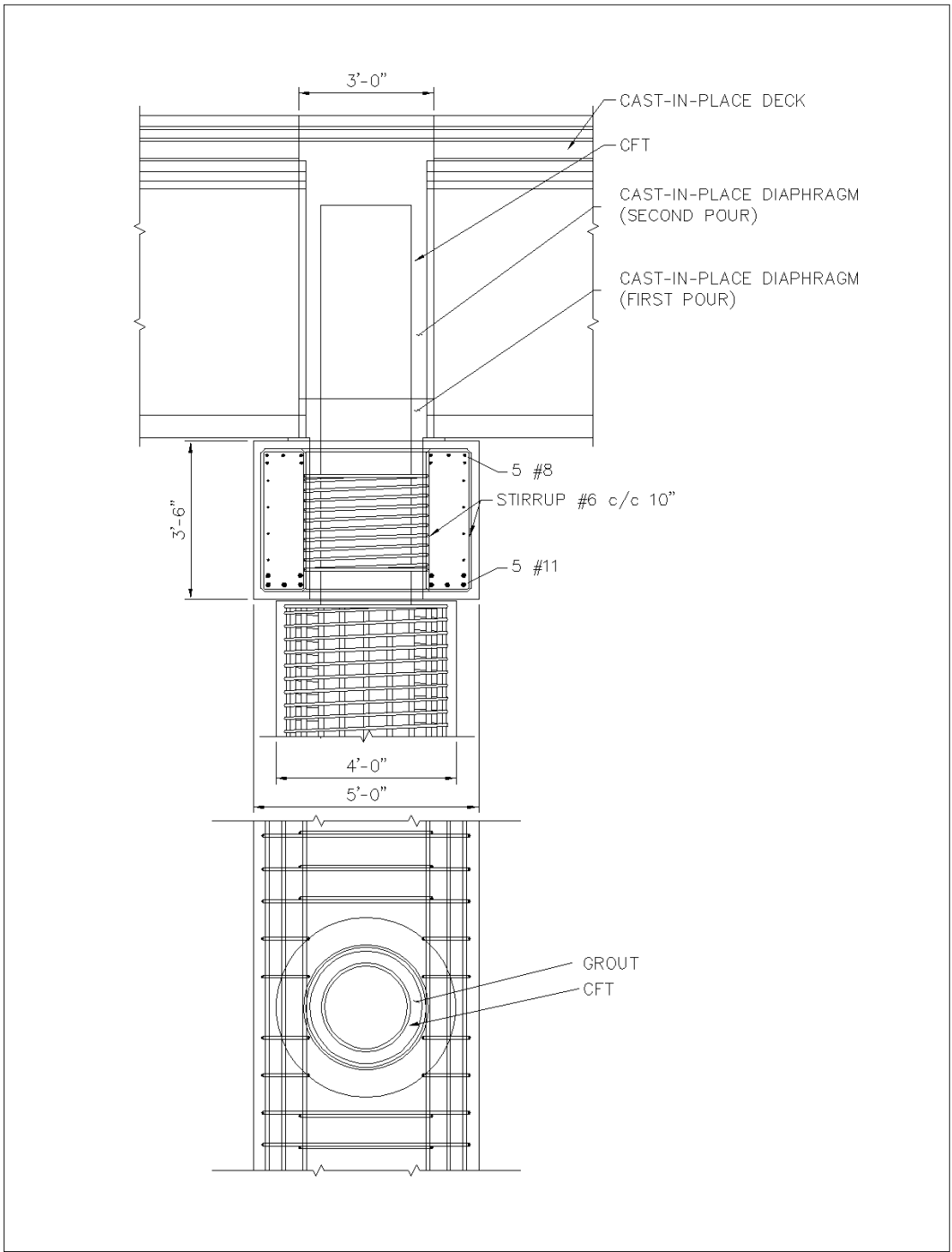


Figure A.4: Concrete filled tube system

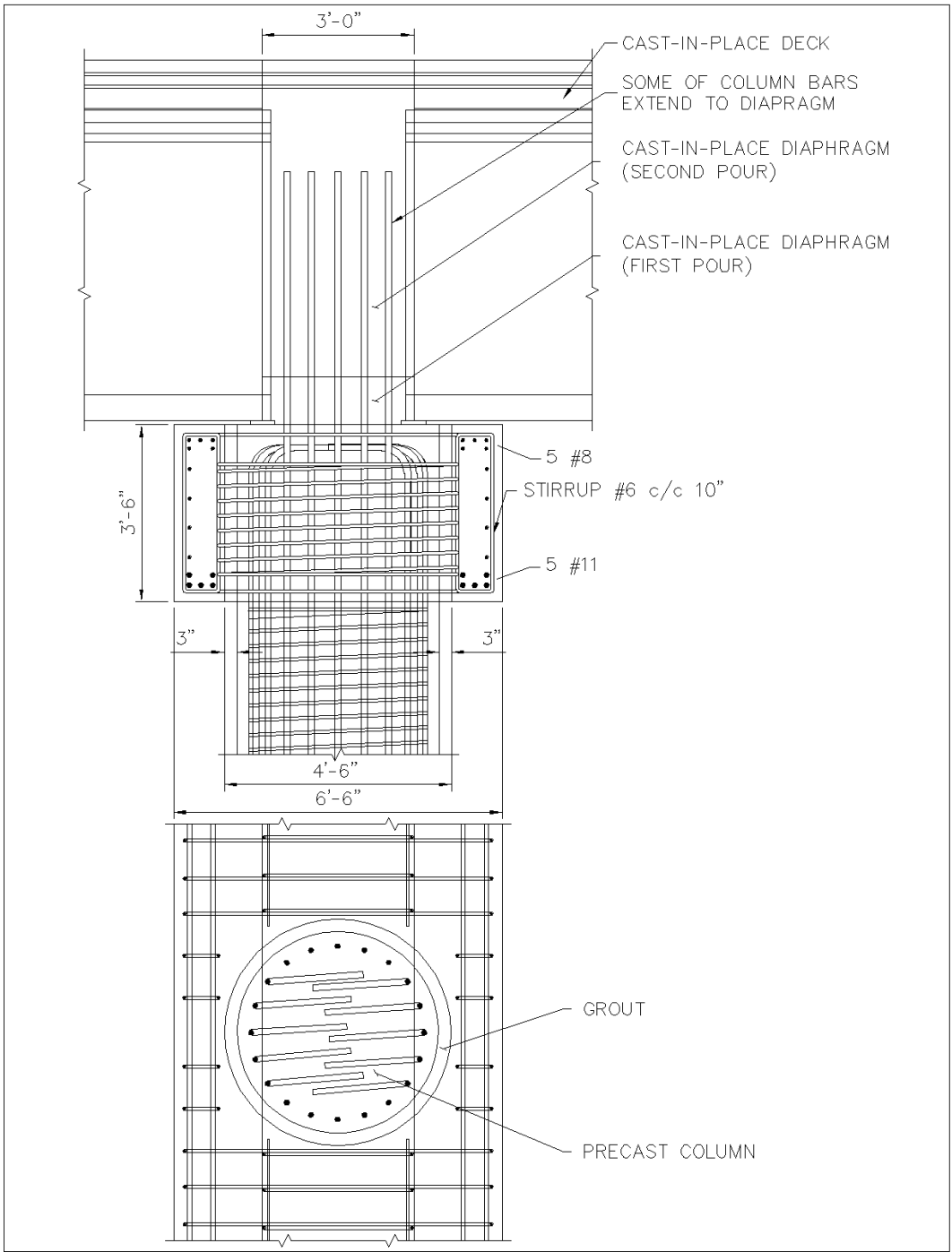


Figure A.5: Column into capbeam system (PSC or RC)

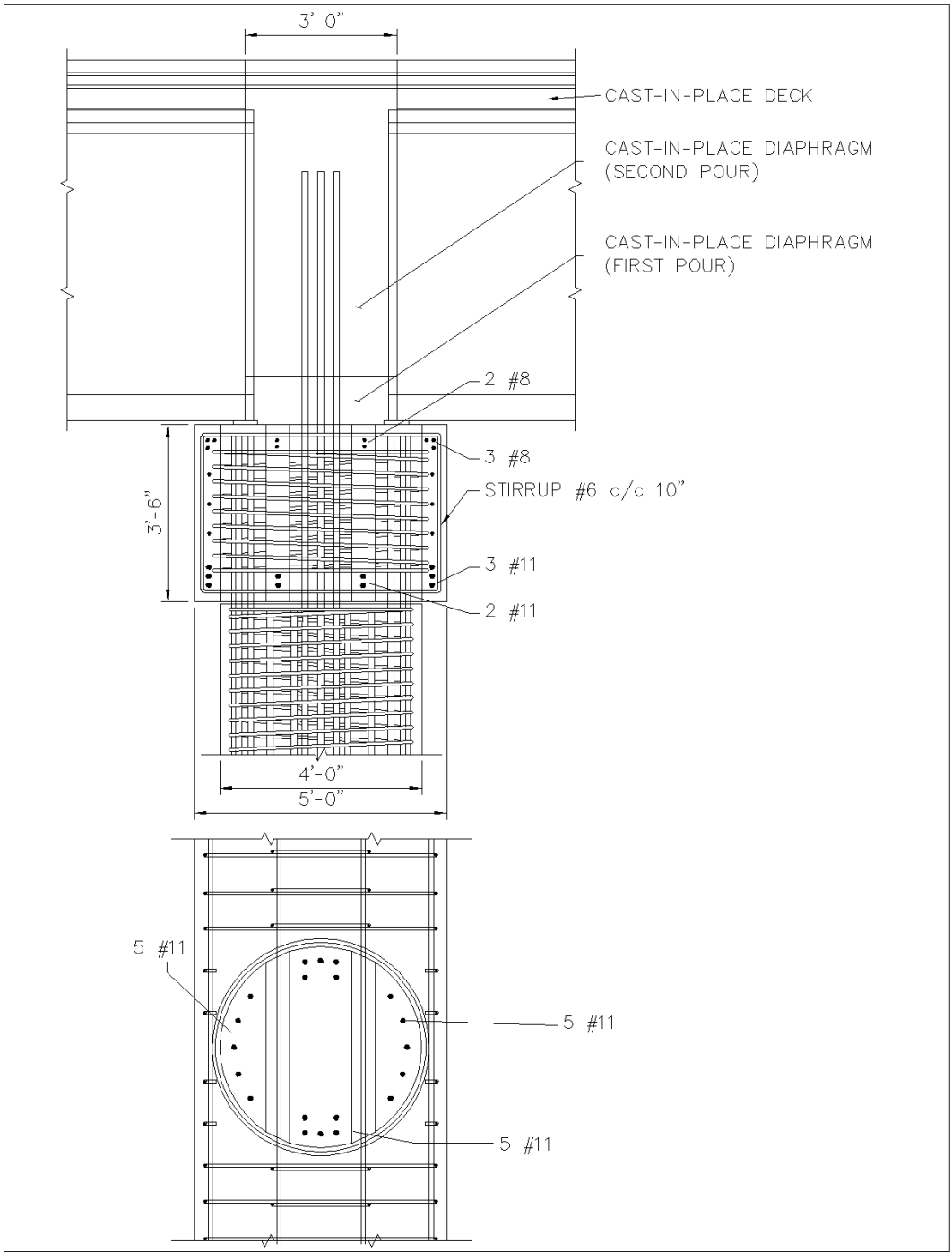


Figure A.6: Slotted column system

APPENDIX B: NET STRESS-STRAIN PLOTS

For each bar, the net stress versus strain plots are shown. A line with a slope of 29000 ksi is also shown, representing the expected value of E.

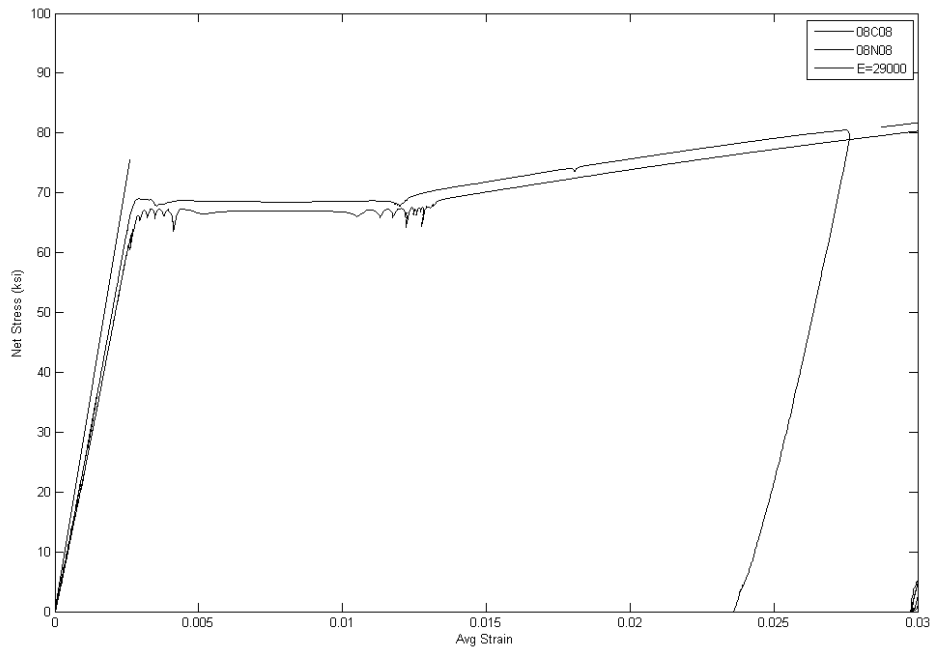


Figure B.1: #8 Bar (08N08, 08C08)

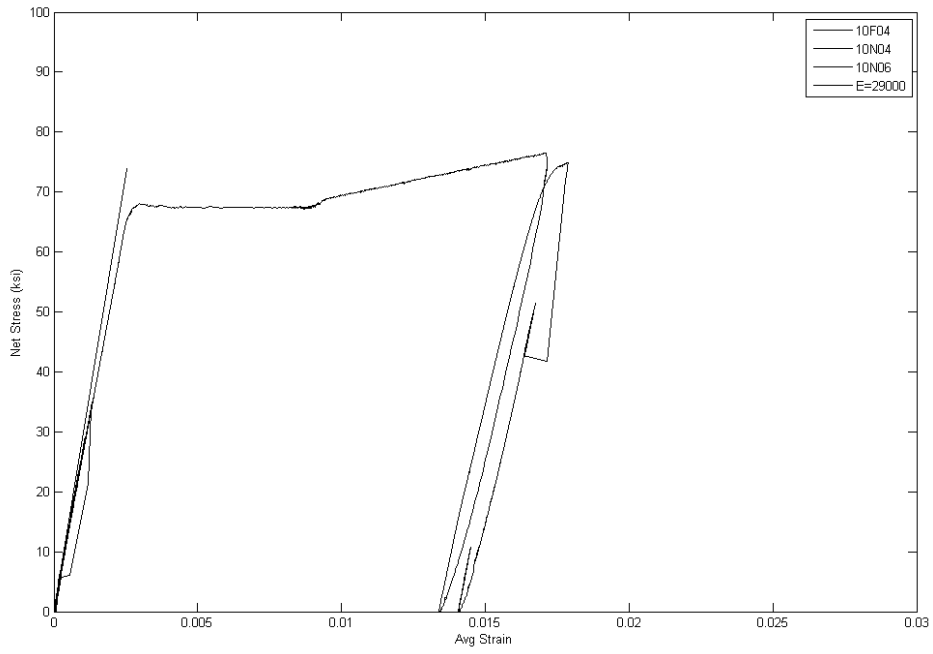


Figure B.2: #10 bar (10F04, 10N04, 10N06)

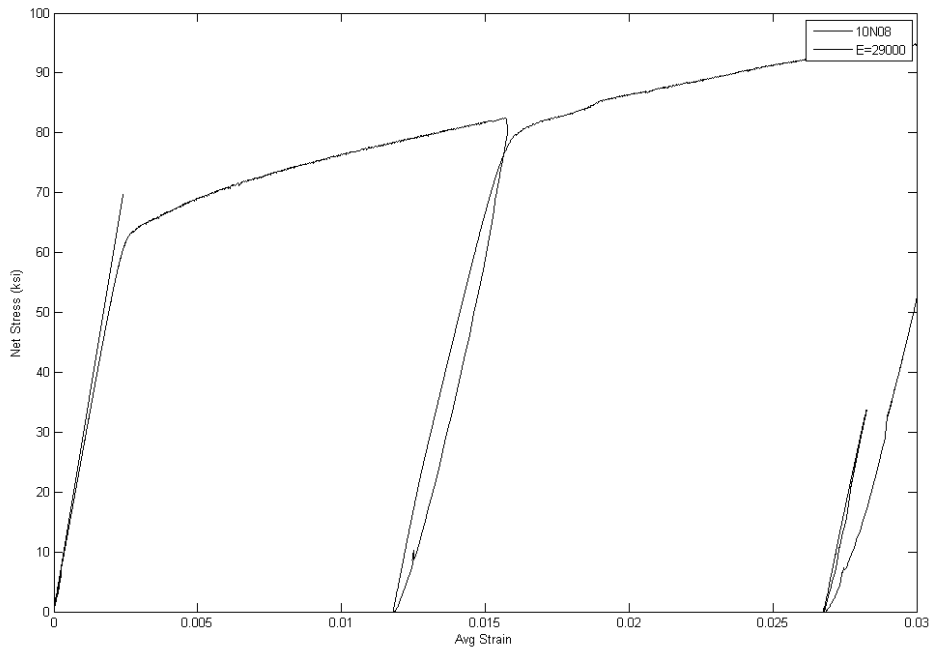


Figure B.3: #10 Bar (10N08)

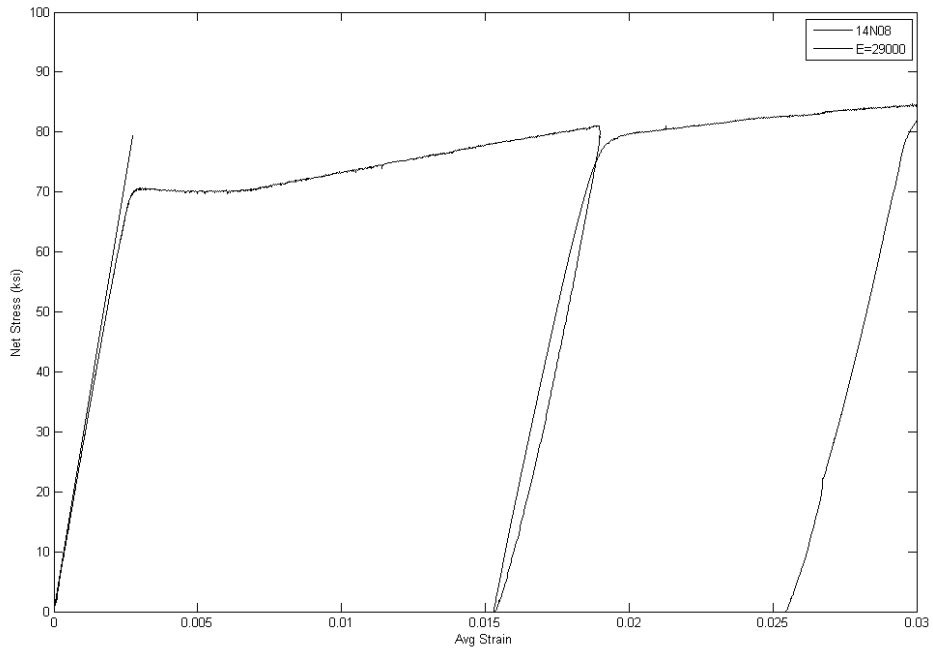


Figure B.4: #14 Bar (14N08)

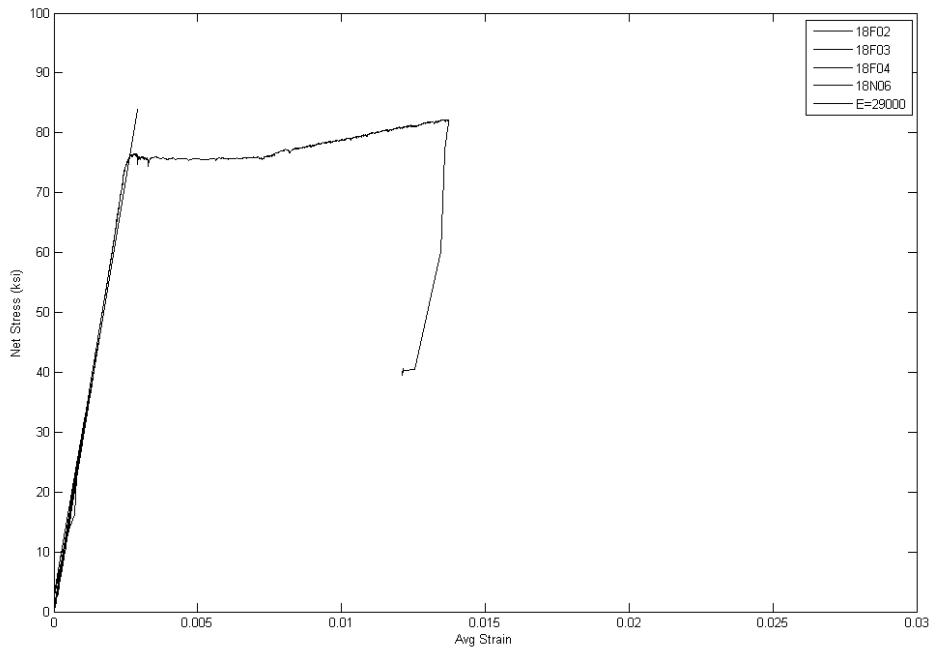


Figure B.5: #18 Bar (18F02, 18F03, 18F04, 18N06)

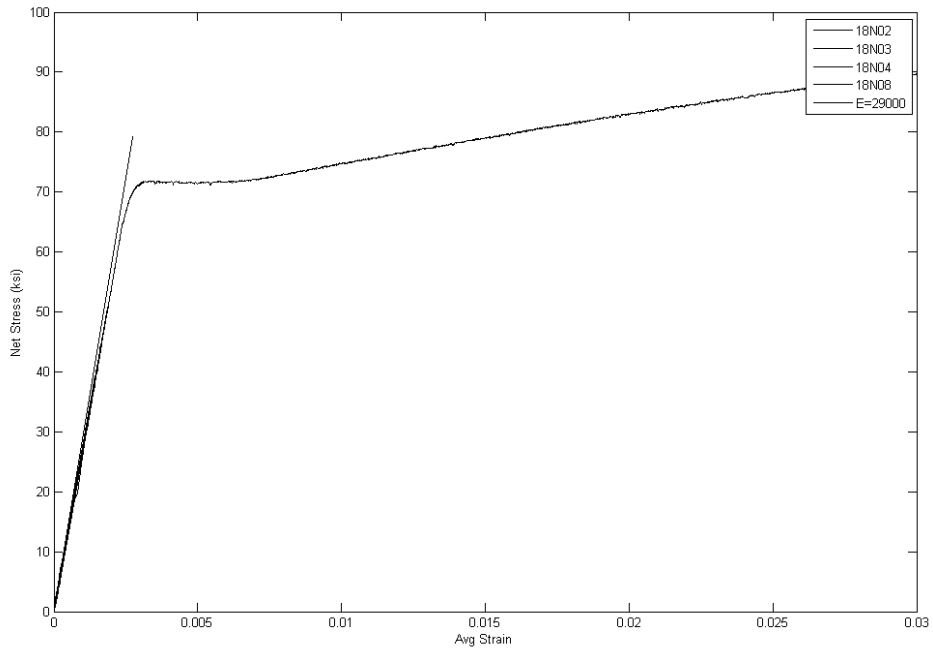


Figure B.6: #18 Bar (18N02, 18N03, 18N04, 18N08)

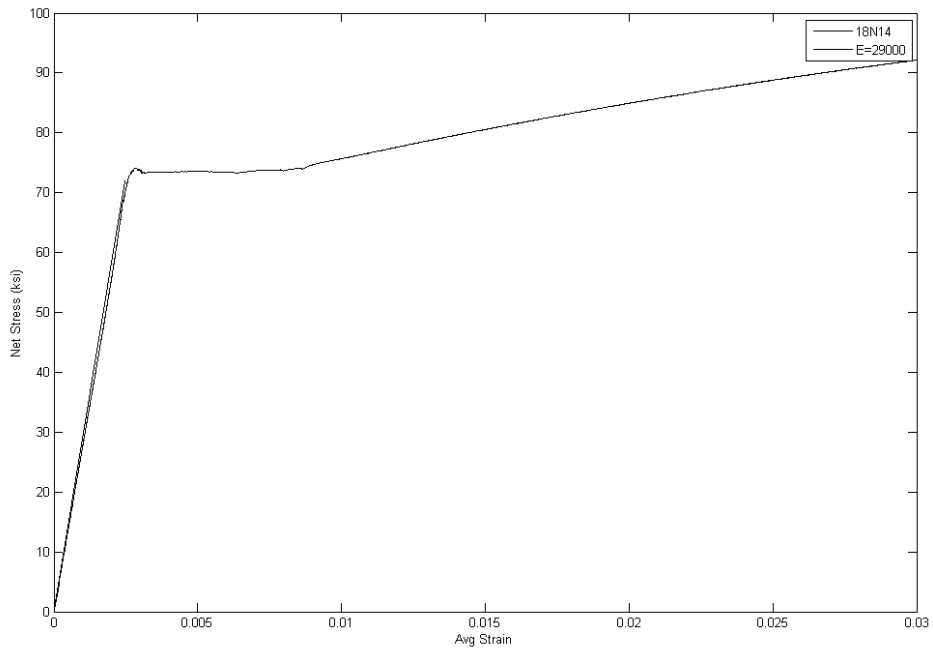


Figure B.7: #18 Bar (19N14)

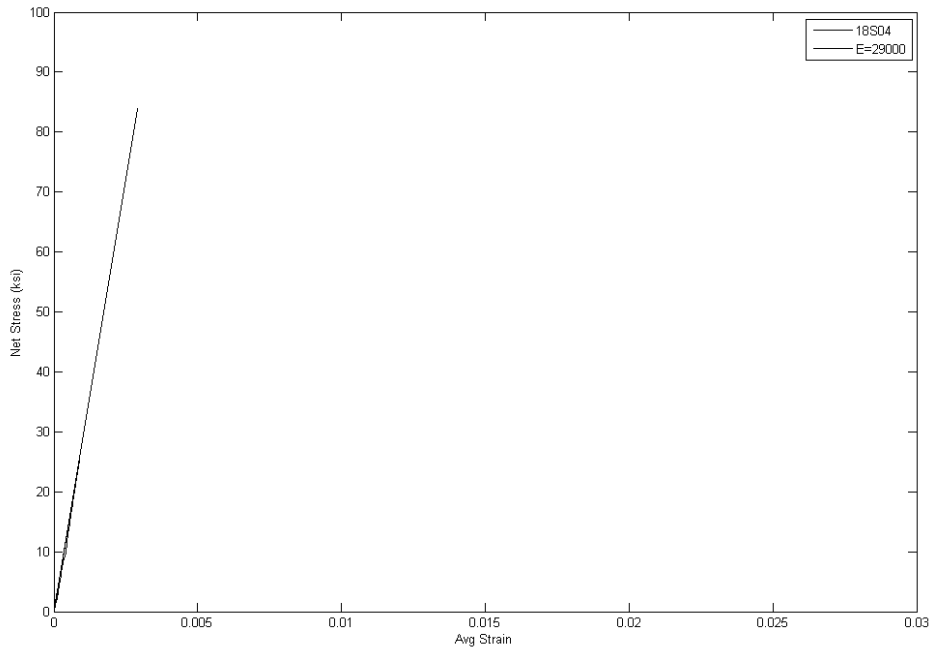


Figure B.8: #18 Bar (18S04)

APPENDIX C: FORCE-DISPLACEMENT PLOTS

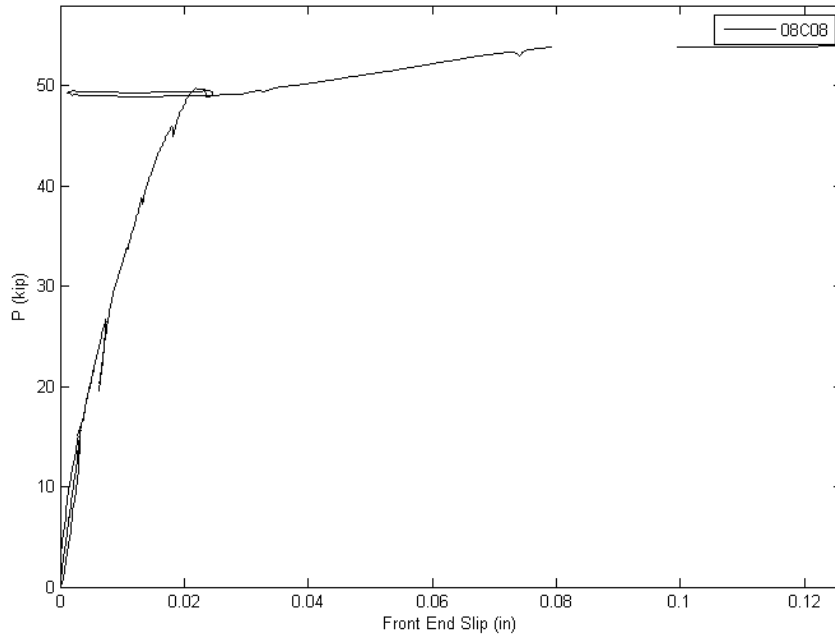


Figure C.1: 08C08

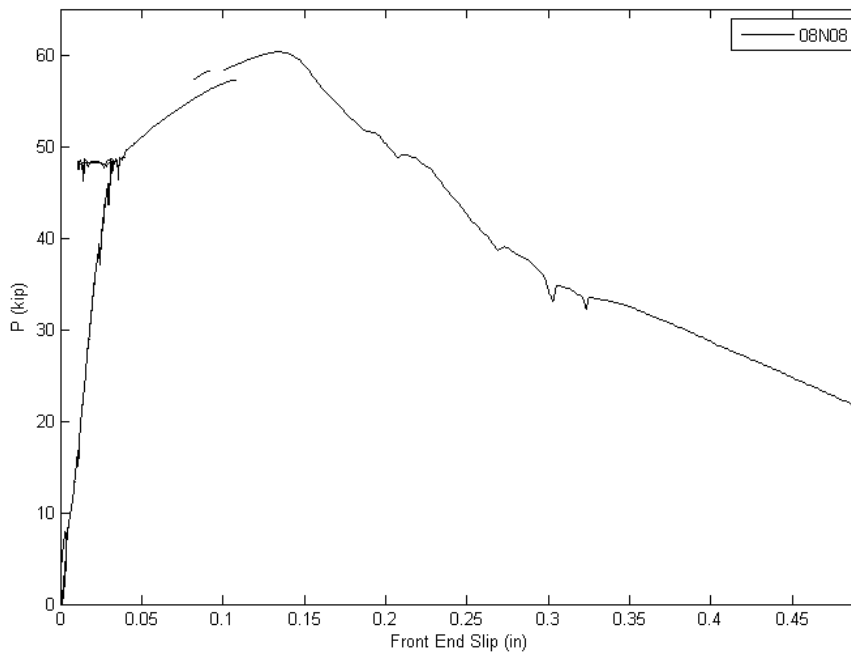


Figure C.2: 08N08

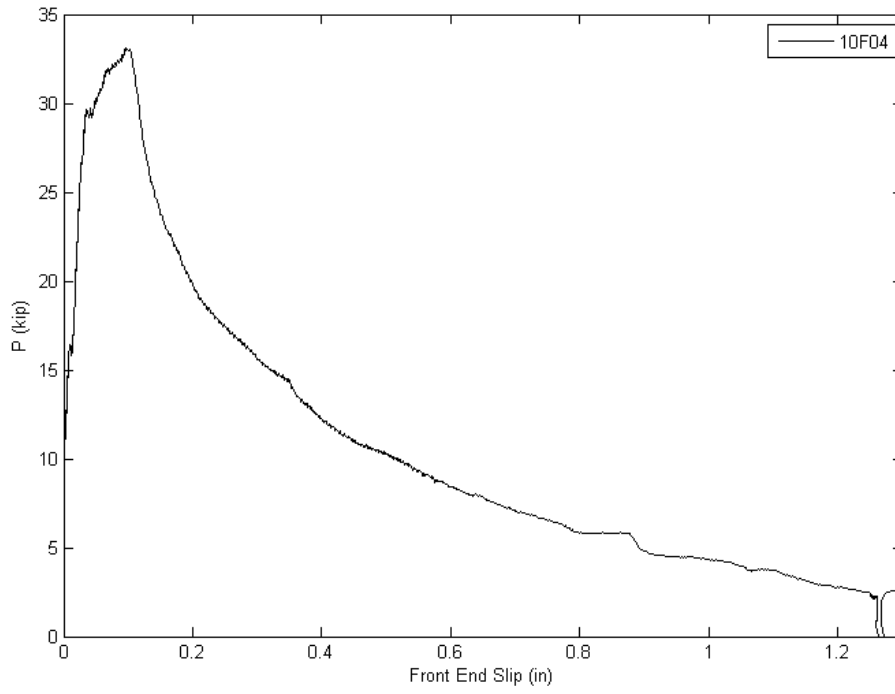


Figure C.3: 10F04

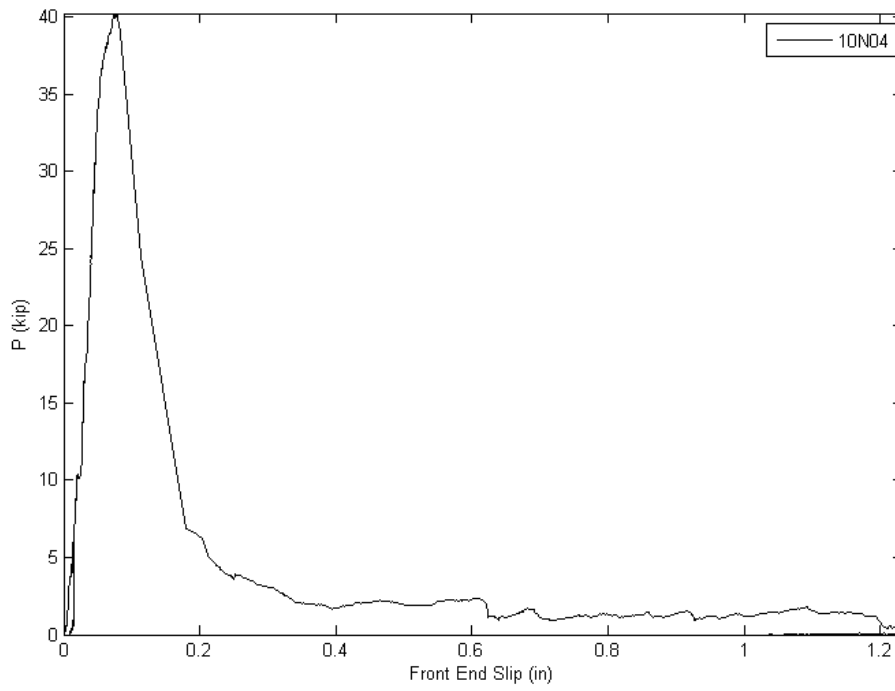


Figure C.4: 10N04

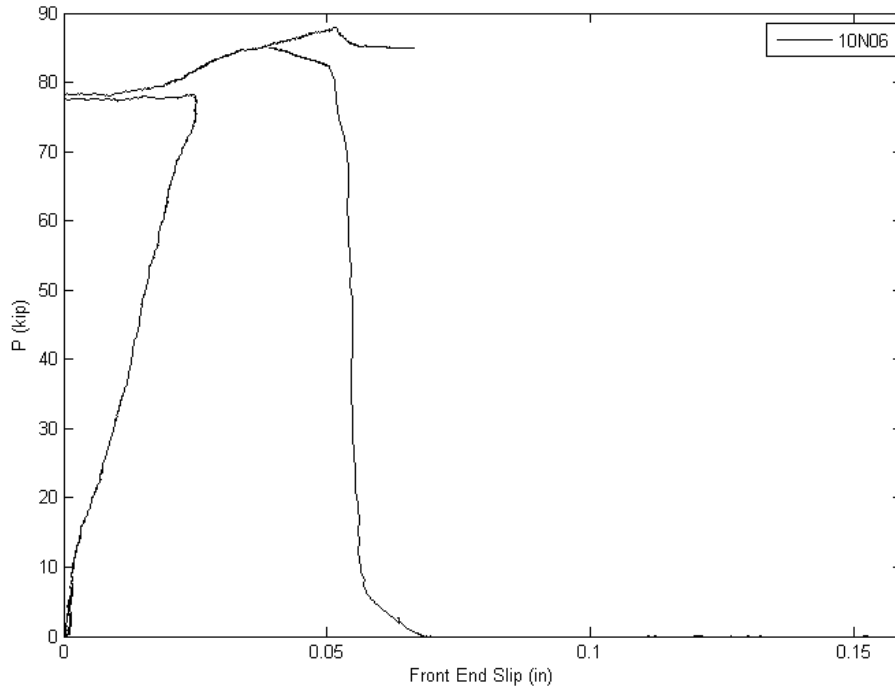


Figure C.5: 10N06

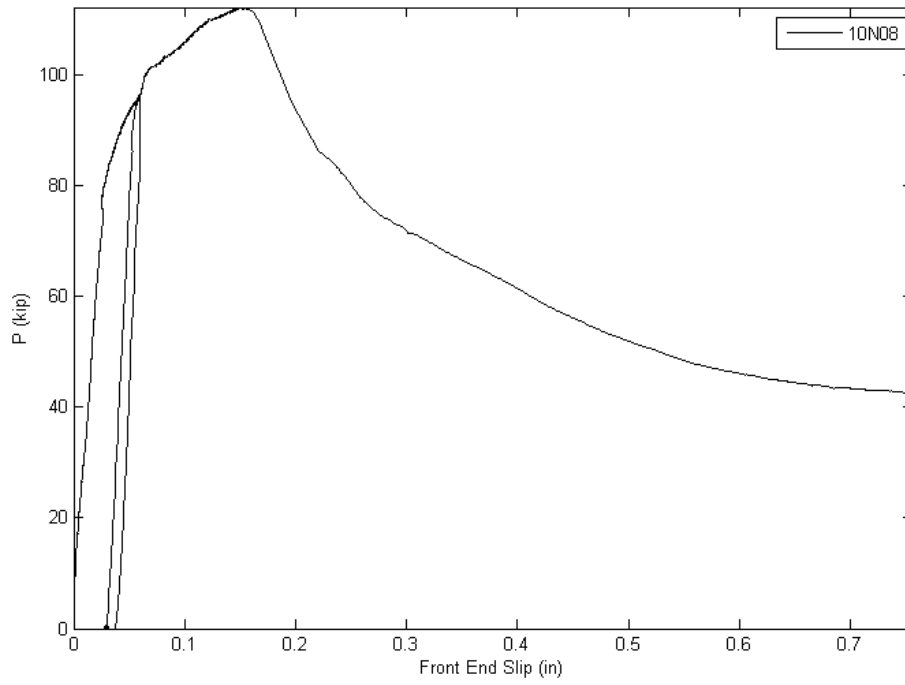


Figure C.6: 10N08

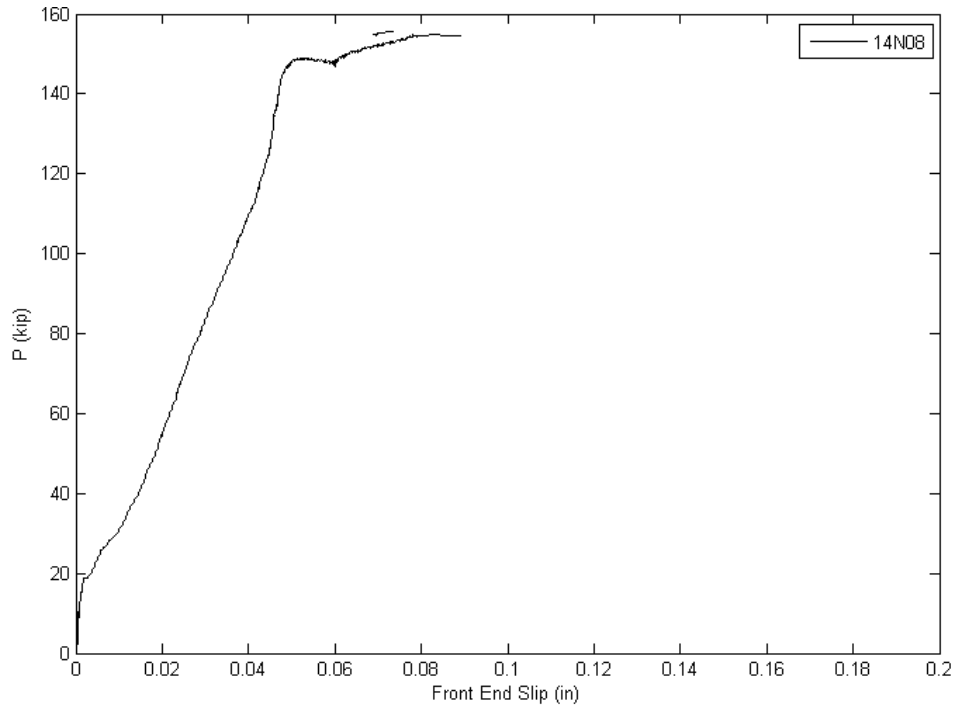


Figure C.7: 14N08 (Note: Displacement measurements became unreliable before peak load reached)

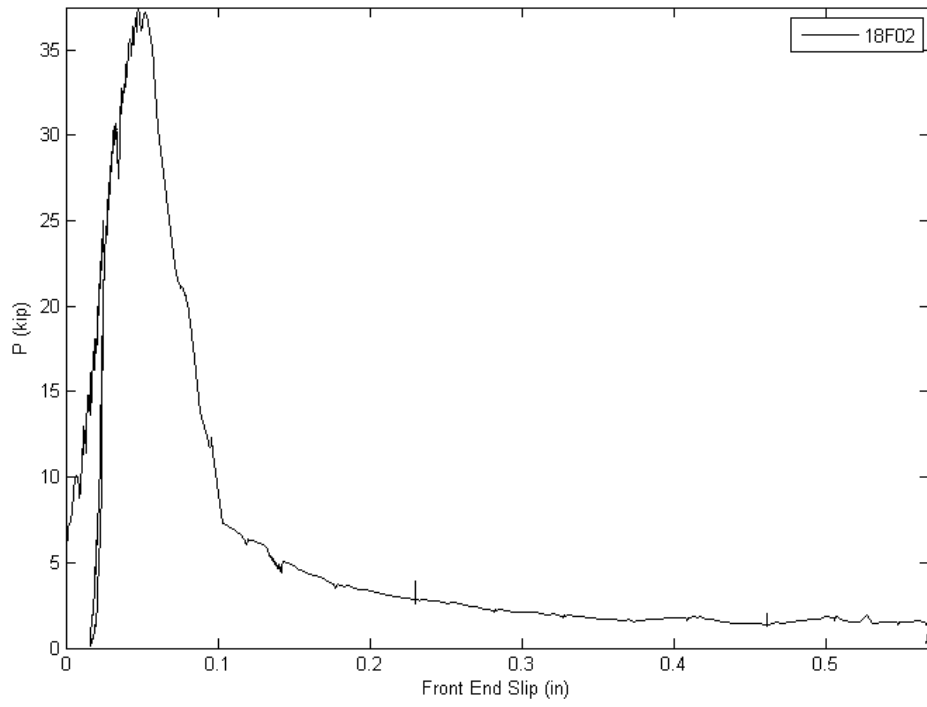


Figure C.8: 18F02

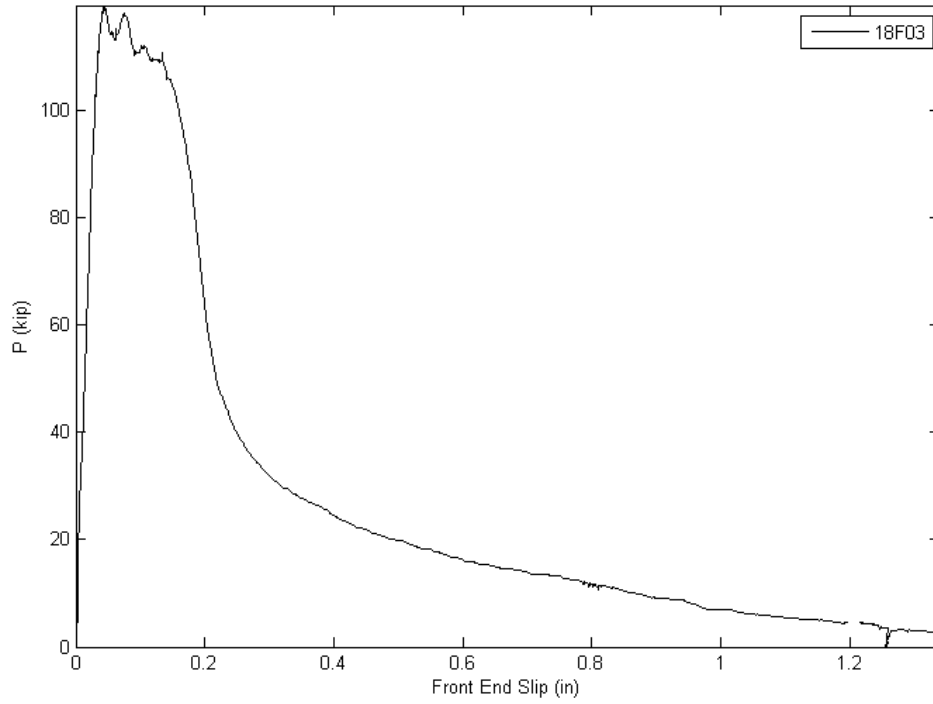


Figure C.9: 18F03

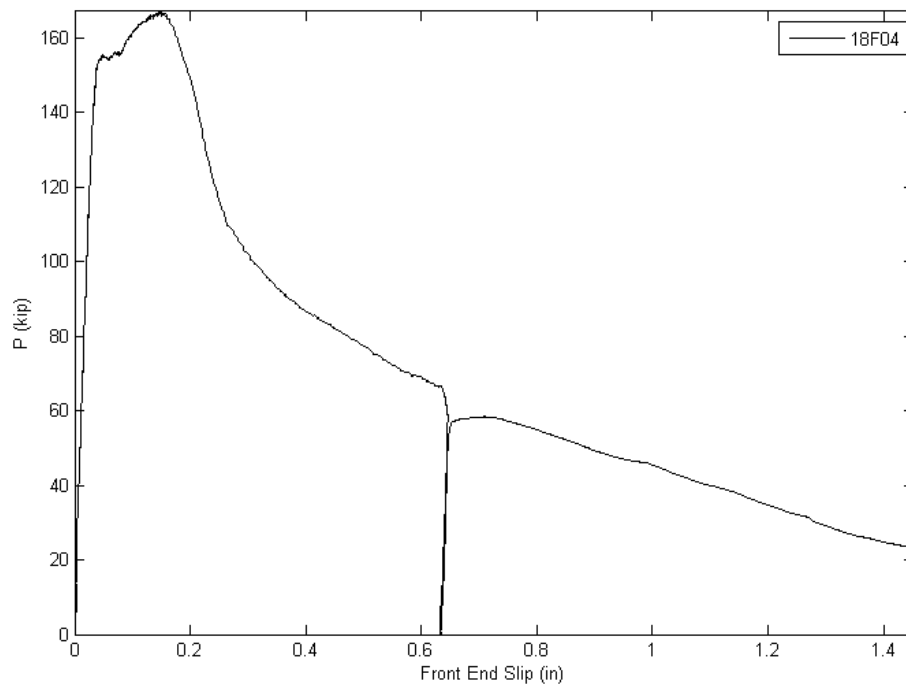


Figure C.10: 18F04

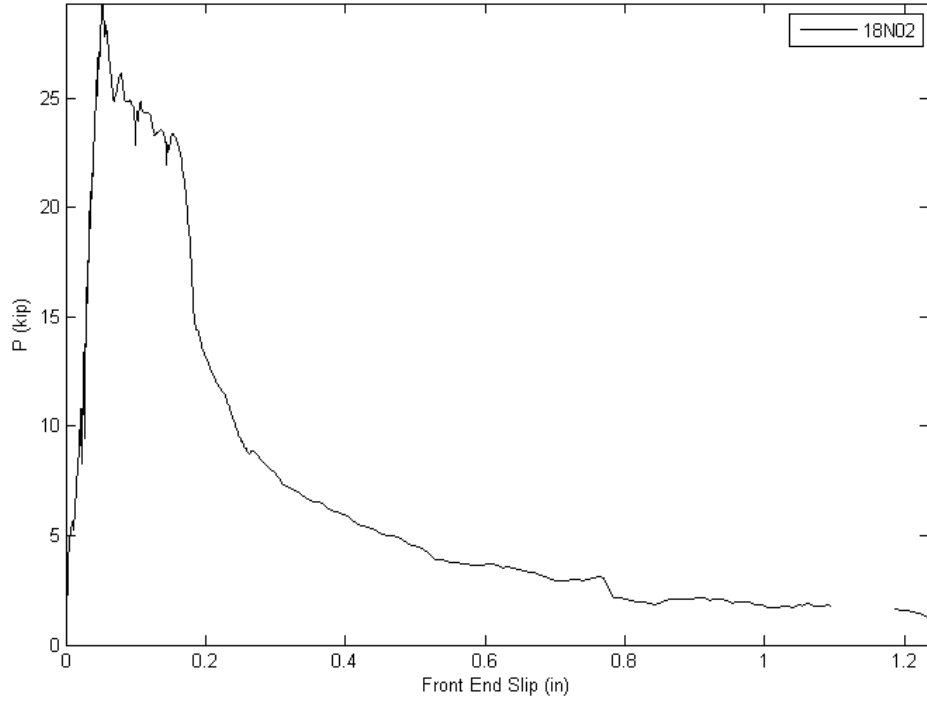


Figure C.11: 18N02

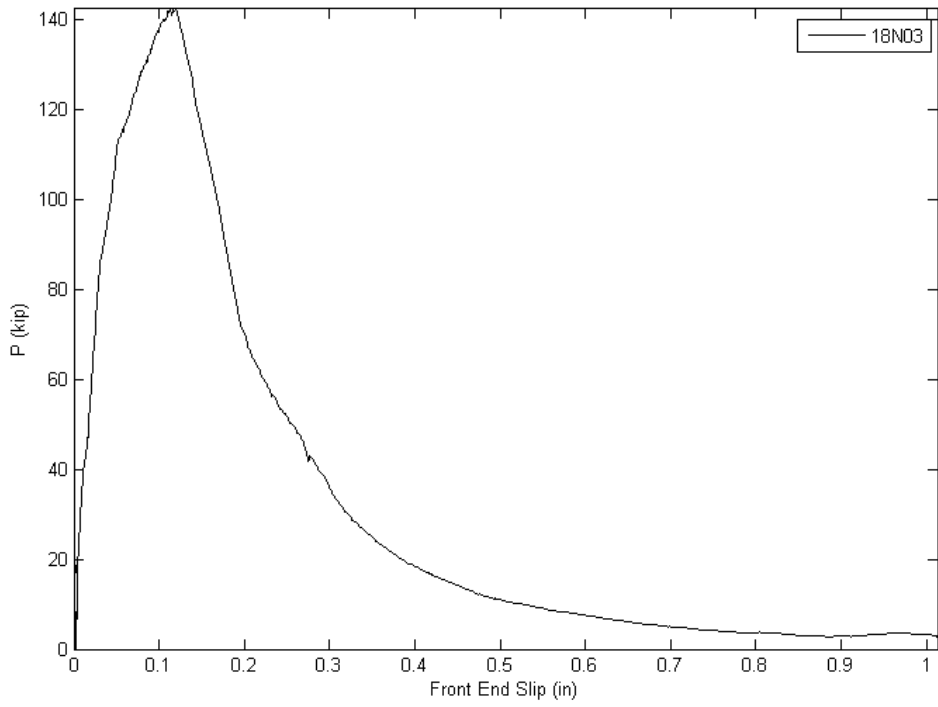


Figure C.12: 18N03

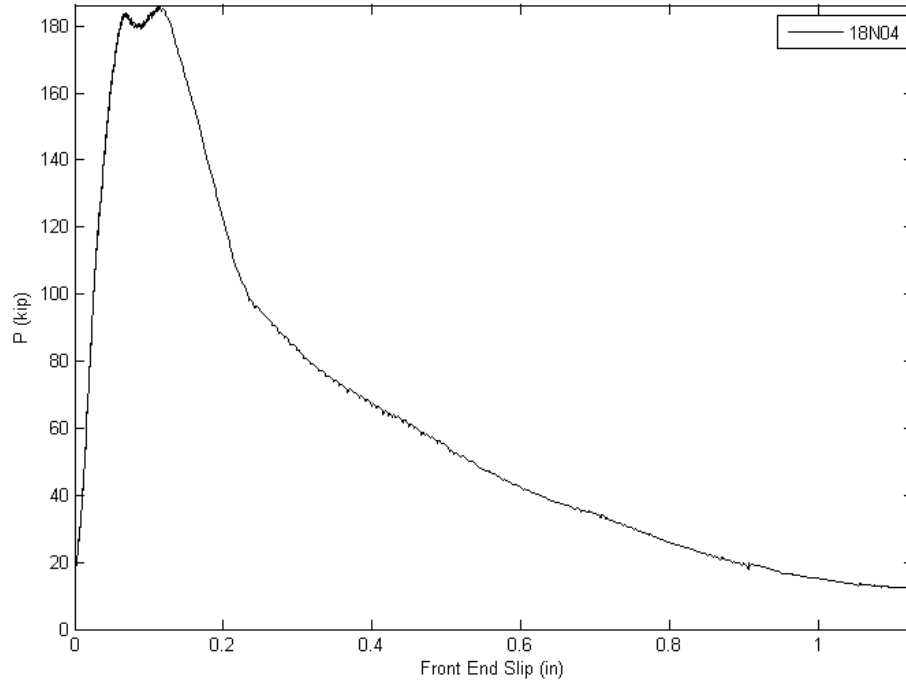


Figure C.13:18N04

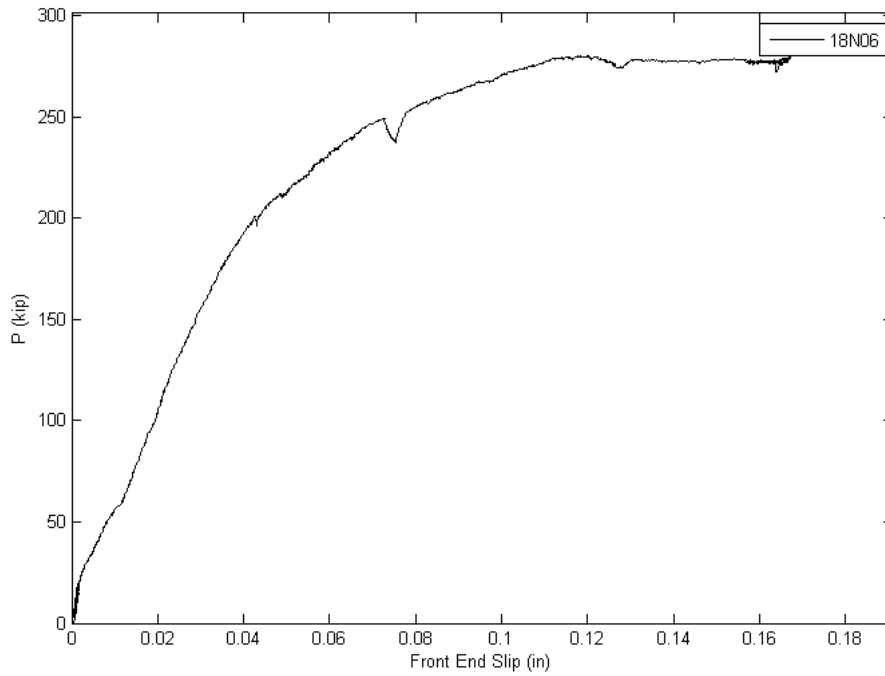


Figure C.14:18N06 (Note: Displacement measurements became unreliable before peak load reached)

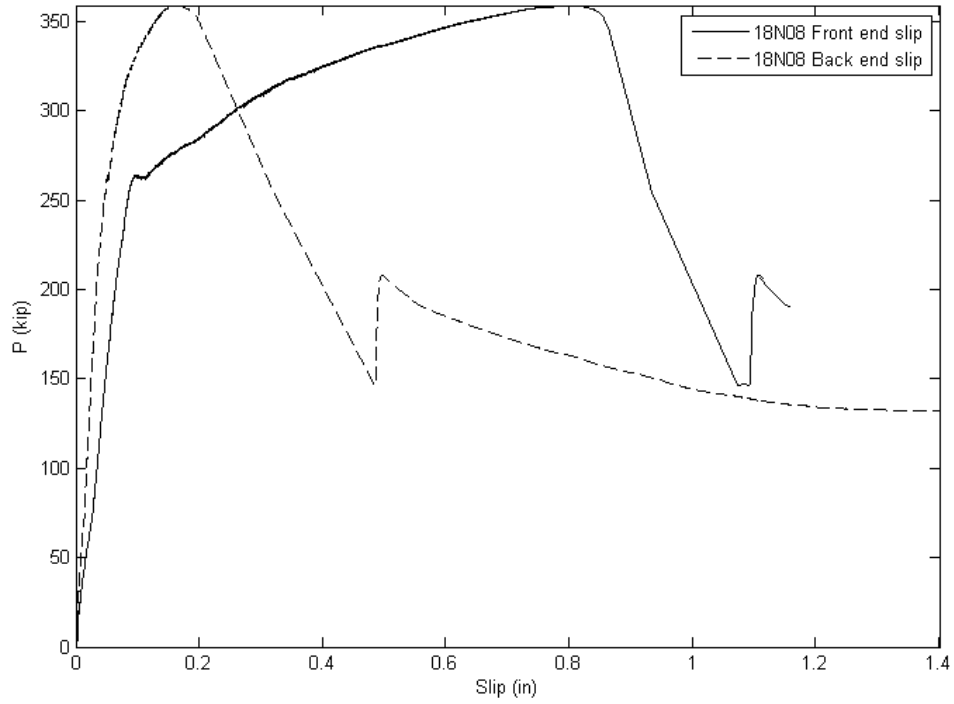


Figure C.15: 18N08

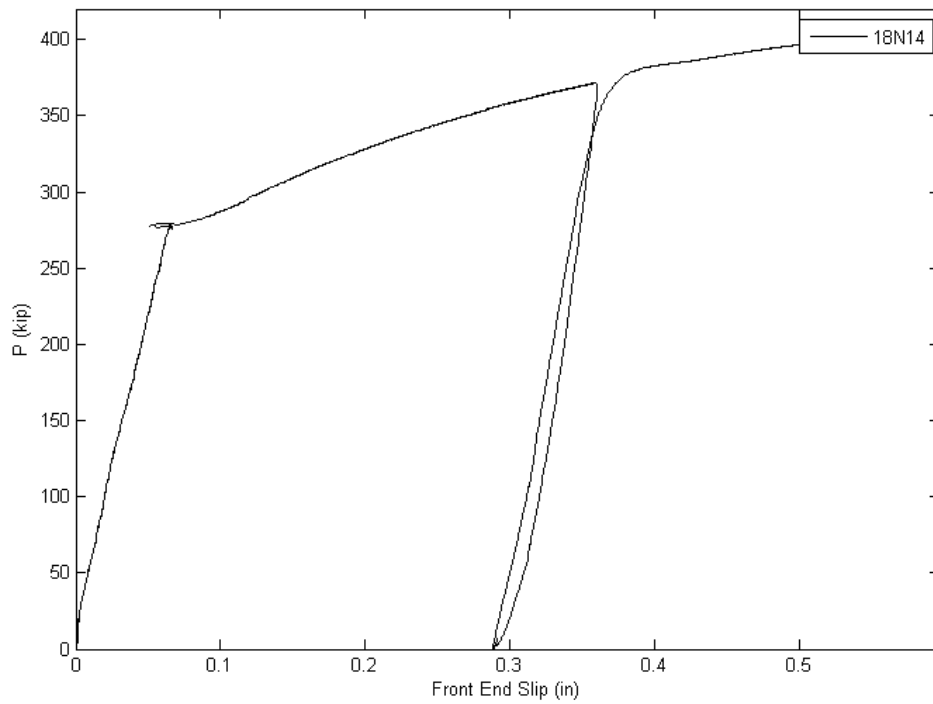


Figure C.16: 18N14 (Note: Displacement measurements became unreliable before peak load reached)

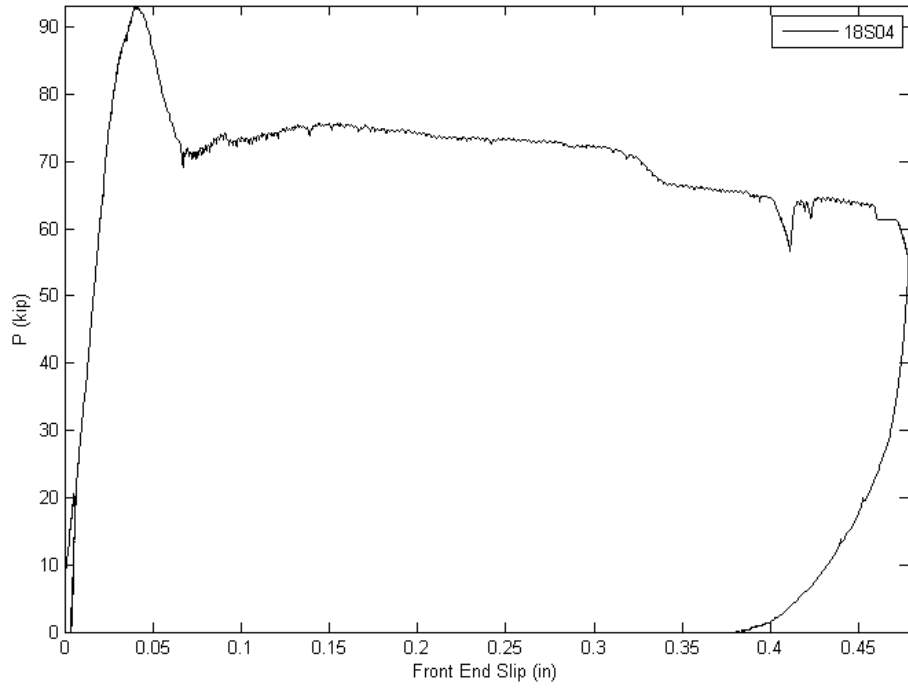


Figure C.17:18S04

APPENDIX D: FEM CODE

The nonlinear FEM was implemented in Matlab. The following code consists of five functions. *Testsim*, given the embedded length, bar properties, grout properties, assumed cone length, and choice of bond model, simulates a test. The function increments the back-end slip and finds the front-end slip and front-end stress for each increment. The function also locates the maximum bar stress and stores the distribution of bar stress, bond stress, slip, and strain along the length of the bar for this state.

Barpull finds the distribution of bar stress, bond stress, slip, and strain along the embedded length for a given back-end slip. *Barpull* calls *stressstrain* for the steel constitutive model and *monomodels* for the bond constitutive model.

Stressstrain is a simple function that finds the strain given a particular stress and allows for unloading after yielding. It calls *monostressstrain* for the backbone steel stress-strain curve.

testsim

```
function [SlipVec StressVec BackSlipVec] = testsim(L, db, ab, fg,
cone, plotflag)
% simulates a run through a test by incrementing the backend slip

nL = 1; % number of length increments to run (runs
nL+1)
le = L/2; % initial length
Linc = (L - le) / nL;

backendslip = 0.0001; % initial back end slip
nSlip = 250; % # of slip increments
maxslip = 0.25; % largest back end slip
Slipinc = (maxslip - backendslip)/nSlip;

% initialize variables
StressVec = 0;
SlipVec = 0;
BackSlipVec = 0;
MaxStress = 0;

% run once w/ L=le/2
ValueMap = barpull(le, backendslip, db, ab, fg, cone, 0);
StressVec = [StressVec ValueMap(size(ValueMap,1),3)];
SlipVec = [SlipVec ValueMap(size(ValueMap,1),2)];
BackSlipVec = [BackSlipVec ValueMap(1,2)];
le = le + Linc;
```

```

if ValueMap(size(ValueMap,1),3) > MaxStress;
    MaxValues = ValueMap;
    MaxStress = ValueMap(size(ValueMap,1),3);
end

LocalStressMax = zeros(size(ValueMap,1),1);

while backendslip < maxslip
    ValueMap = barpull(L, backendslip, db, ab, fg, cone,
LocalStressMax);
    StressVec = [StressVec ValueMap(size(ValueMap,1),3)];
    SlipVec = [SlipVec ValueMap(size(ValueMap,1),2)];
    BackSlipVec = [BackSlipVec ValueMap(1,2)];
    backendslip = backendslip + Slipinc;
    LocalStressMax=max(LocalStressMax,ValueMap(:,3));
    if ValueMap(size(ValueMap,1),3) > MaxStress;
        MaxValues = ValueMap;
        MaxStress = ValueMap(size(ValueMap,1),3);
    end
end %endwhile

if plotflag==true
figure(1)
plot(SlipVec, StressVec,BackSlipVec, StressVec);
xlabel('Front End Slip');
ylabel('Stress');

figure(2)
plot(MaxValues(:,1),MaxValues(:,2));
xlabel('Location');
ylabel('Slip');

figure(3)
plot(MaxValues(:,1),MaxValues(:,5));
xlabel('Location');
ylabel('Tau');

figure(4)
plot(MaxValues(:,1),MaxValues(:,3));
xlabel('Location');
ylabel('Stress');

figure(5)
plot(MaxValues(:,1),MaxValues(:,4));
xlabel('Location');
ylabel('Strain');
end

barpull
function [output] = barpull(L, s0, db, Ab, fg, cone, stressmax)

% Finds state given one back end slip and bar props
nNode = 100;

```

```

x = zeros(nNode,1);
slip = zeros(nNode,1);
stress = zeros(nNode,1);
strain = zeros(nNode,1);
tau = zeros(nNode,1);
if stressmax==0
    stressmax=zeros(nNode,1);
end

for i = 1:nNode
    x(i) = (i-1)*L/(nNode-1);
end

%i=1
slip(1) = s0;
tau(1) = monomodels(slip(1),fg, db, L-x(1),cone);
if tau(1)>10
    pause
end
P = tau(1) * x(2)/2 * pi * db;
stress(1) = P/Ab;
strain(1) = strainstress(stress(1),stressmax(1));
slip(2) = slip(1) + strain(1)*x(2);

for i = 2:nNode    %nodal loop
    tau(i) = monomodels(slip(i),fg,db, L-x(i),cone);
    if i~=nNode
        P = tau(i) * (x(i+1)-x(i-1))/2 * pi * db;
    else
        P = tau(i) * (x(i)-x(i-1))/2 *pi *db;
    end
    stress(i) = stress(i-1) + P/Ab;

    if stress(i)>=105
        break;    % correction for bar fracture
    end

    strain(i) = strainstress(stress(i),stressmax(i));
    if i~=nNode
        slip(i+1) = slip(i) + strain(i)*(x(i+1) - x(i));
    end
end %nodal loop

output = [x slip stress strain tau];

```

monomodels

```

function bond=monomodels(s,fg,db,x,cone)
%Monotonic bond model
% x - distance from live end

slip = s/db; %correction to #18 slip
if x < cone

```

```

    if slip <= .02
        bond = 15 * slip;
    elseif slip <= 0.075
        bond = -10/11 * slip + 7/22;
    elseif slip <= 0.1
        bond = -10 * slip + 1;
    else
        bond = 0;
    end

else
    if slip <=.025
        bond = -1280*slip^2 + 80*slip;
    elseif slip <=0.05
        bond = 1.2;
    elseif slip <= .1
        bond = -11*slip + 1.75;
    elseif slip <= 0.5
        bond = -1.5*slip +.8;
    else
        bond = 0.05;
    end
end
bond = bond * sqrt(fg);

```

stressstrain

```

function strain=strainstress(stress, maxstress);
%Allows unloading on Multilinear steel stress-strain

strain = monostrainstress(stress);
maxstrain = monostrainstress(maxstress);

if strain < maxstrain
    strain = maxstrain - (maxstress-stress)/26000;
end

```

monostressstrain

```

function strain=monostrainstress(stress);
%Monotonic, multilinear steel stress-strain
% Developed by Raynor, constants taken from test results with
nominal area
% Includes shallow yield plateau, polynomial strain hardening

ord=6;

stress1 = 70;           % yield
stress2 = 70.1;        % end of yield plateau
stress3 = 105;         % ultimate
E1 = 26000;            % Young's modulus
eps1 = stress1/E1;     % yield
eps2 = 0.009;         % end of yield plateau
eps3 = 0.2;           % ultimate

```

```
if stress <= stress1
    strain = stress / E1 ;
elseif stress <= stress2
    E2 = (stress2 - stress1)/(eps2 - eps1);
    strain = eps1 + (stress-stress1)/E2;
elseif stress <= stress3
    k = (stress2 - stress3)/(eps2 - eps3).^ord;
    strain = eps3 - ((stress - stress3)/k).^(1/ord);
else
    strain = eps3;
end
```


APPENDIX E: MODEL RESULTS

Table E.1: Peak bar stress comparison

Test	Peak nominal bar stress (ksi)	
	Model	Test
08C08	90.7	73.4
08N08	89.6	76.3
10F04	37.4	26.1
10N04	16.1	31.7
10N06	53.2	69.3
10N08	74.7	88.4
14N08	85.0	79.4
18F02	13.1	9.4
18F03	28.3	29.9
18F04	39.1	41.8
18N02	12.5	7.3
18N03	22.8	35.6
18N04	44.3	46.6
18N06	76.3	75.2
18N08	94.6	89.7
18N14	105.0	105.0
18S04	39.8	23.3

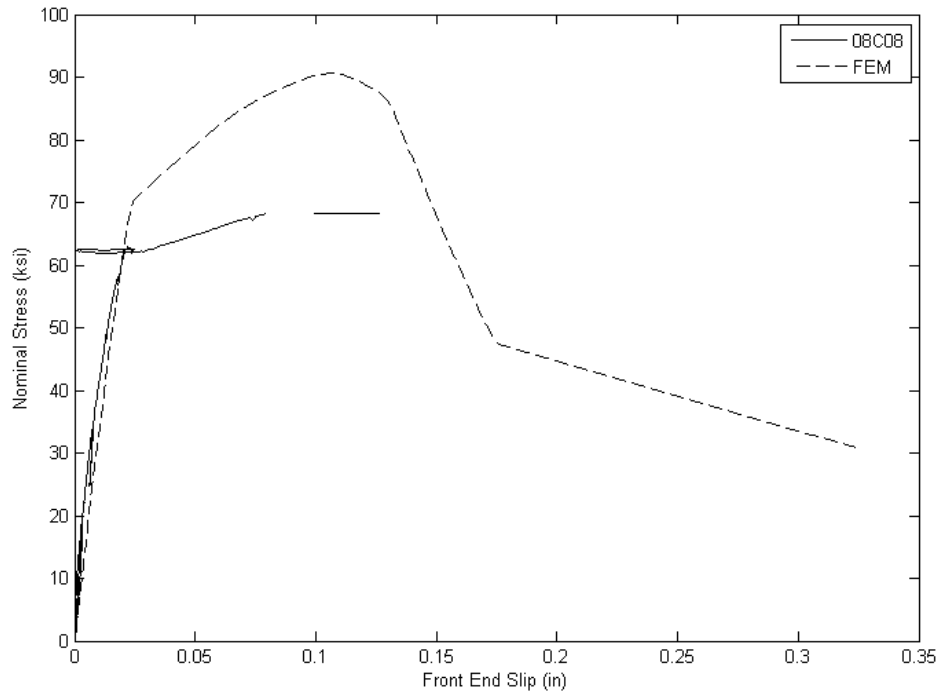


Figure E.1: 08C08 (Note: concrete splitting mode not included in model)

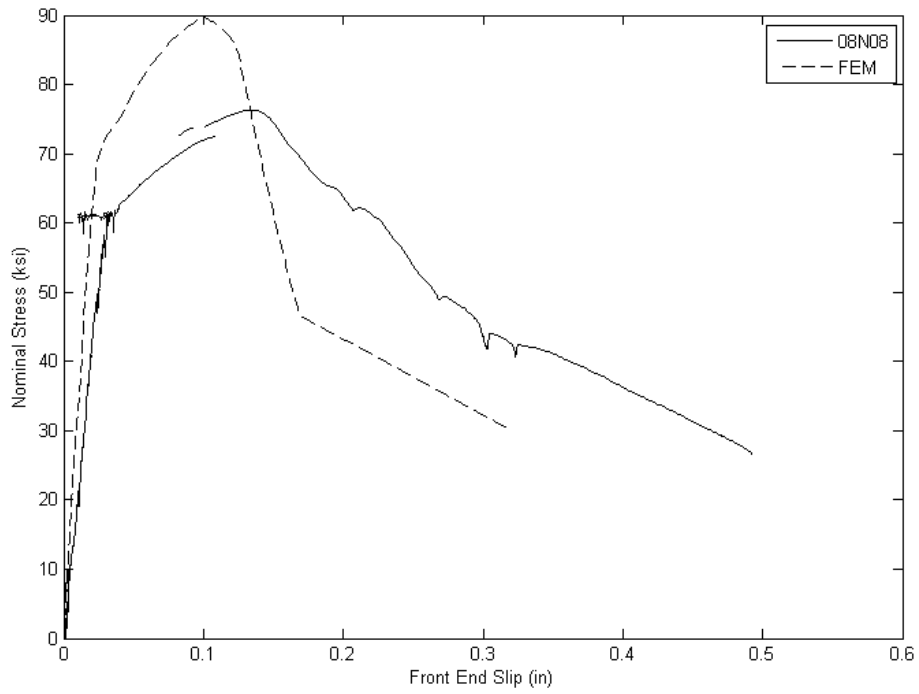


Figure E.2: 08N08

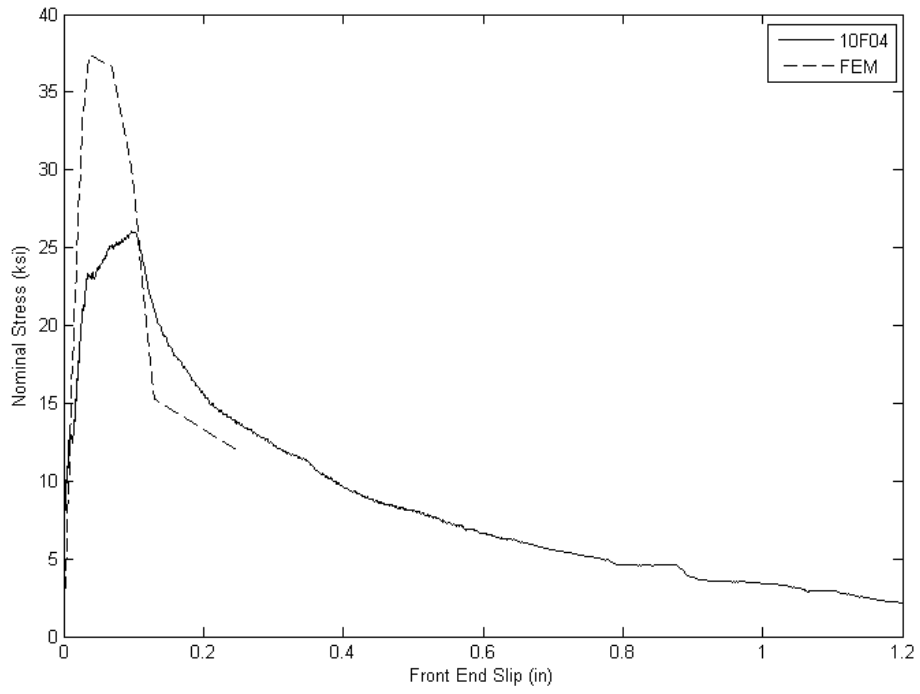


Figure E.3: 10F04

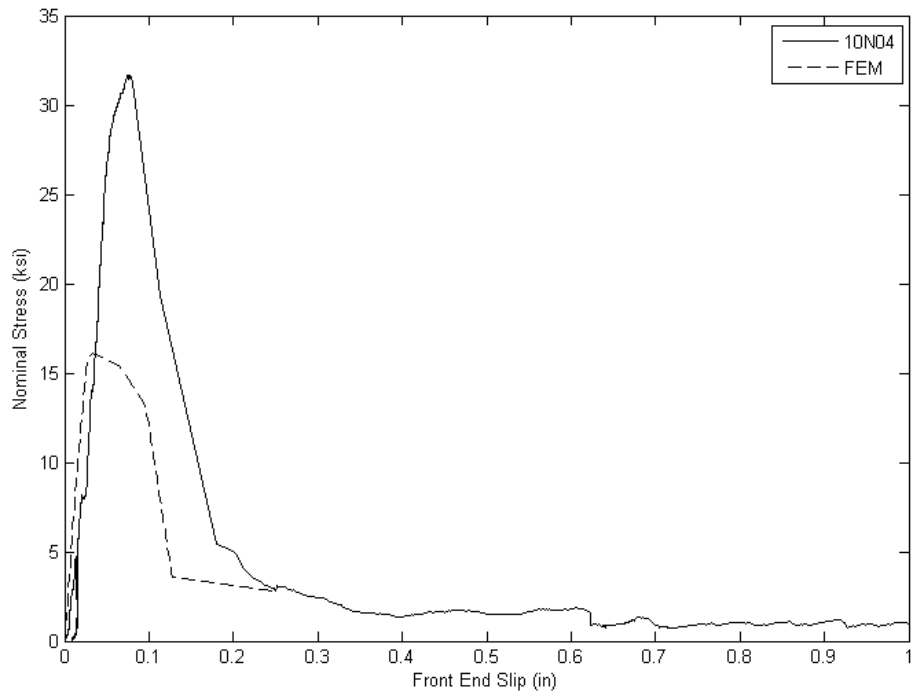


Figure E.4: 10N04

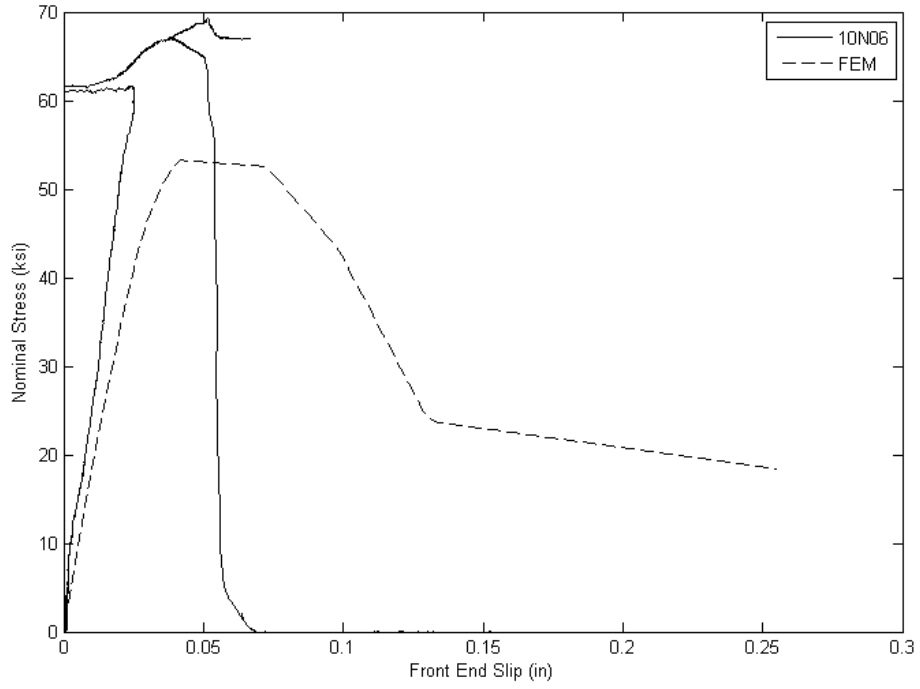


Figure E.5: 10N06

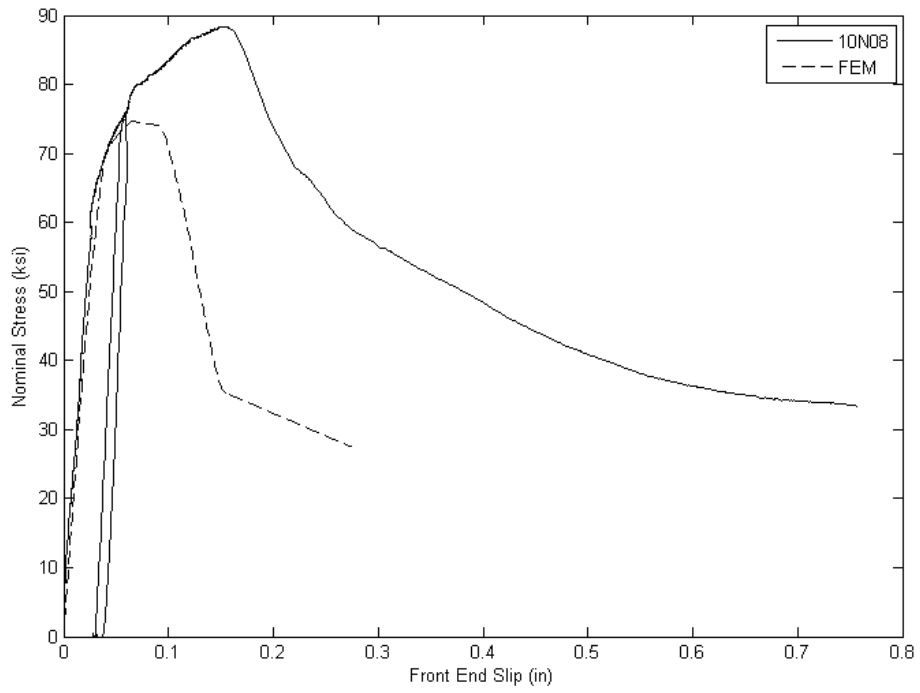


Figure E.6: 10N08

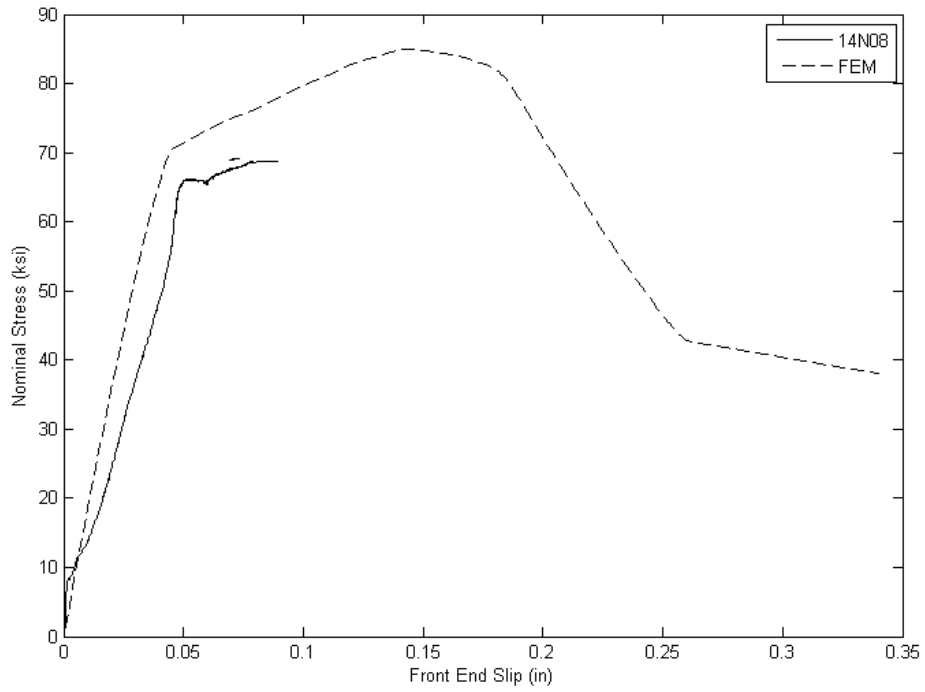


Figure E.7: 14N08 (Note: Displacement measurements became unreliable before peak load reached.)

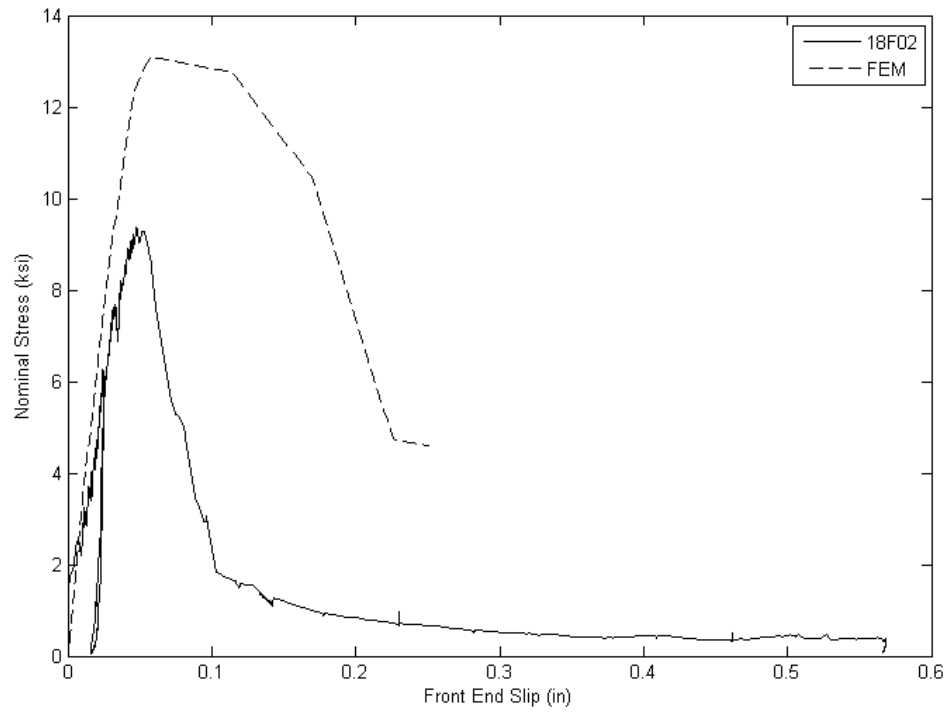


Figure E.8: 18F02

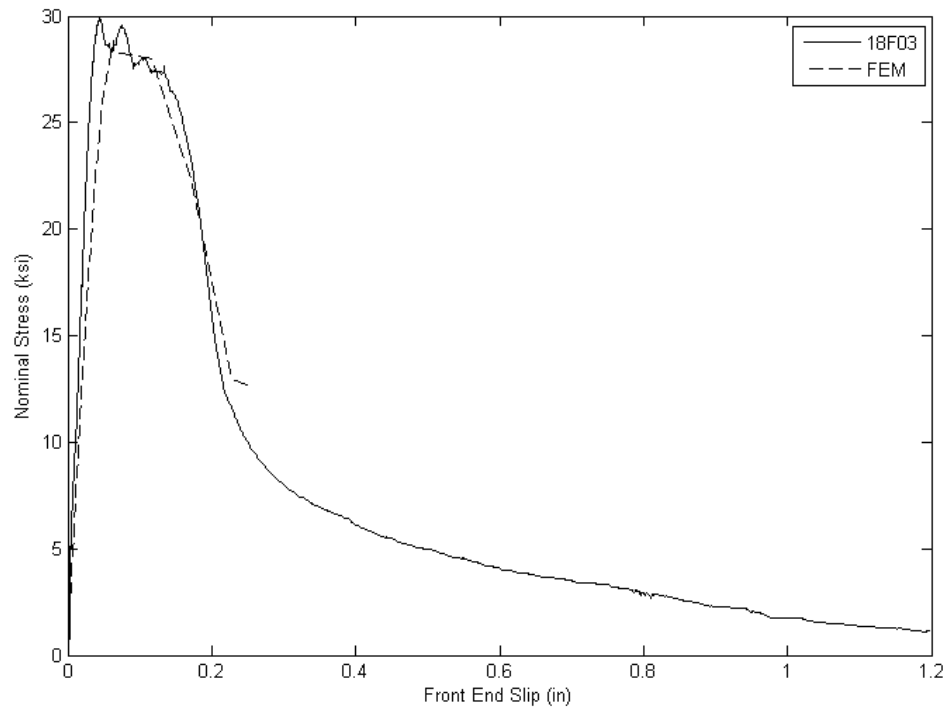


Figure E.9: 18F03

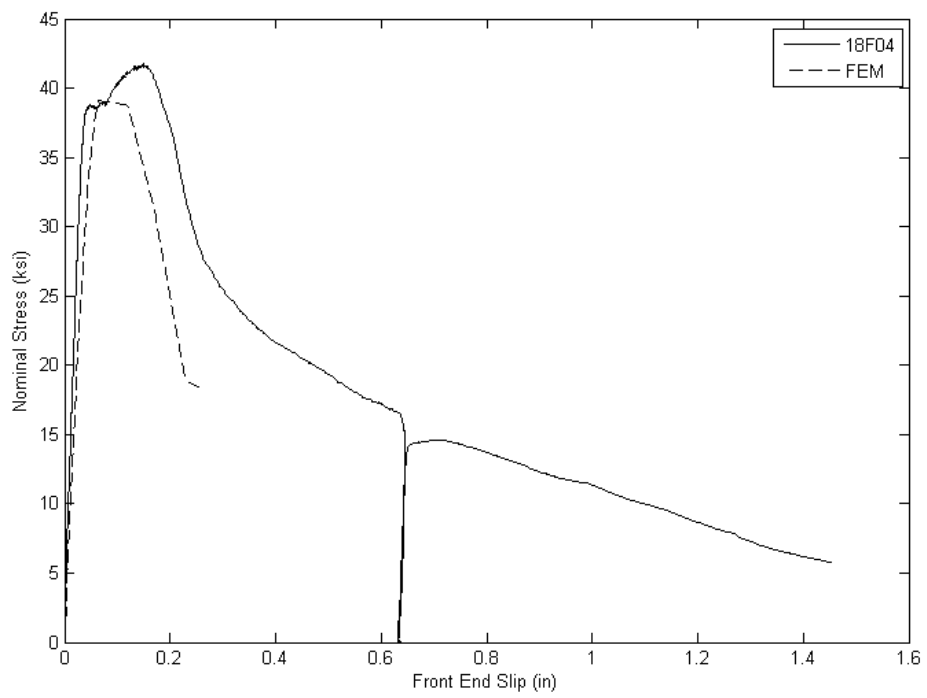


Figure E.10: 18F04

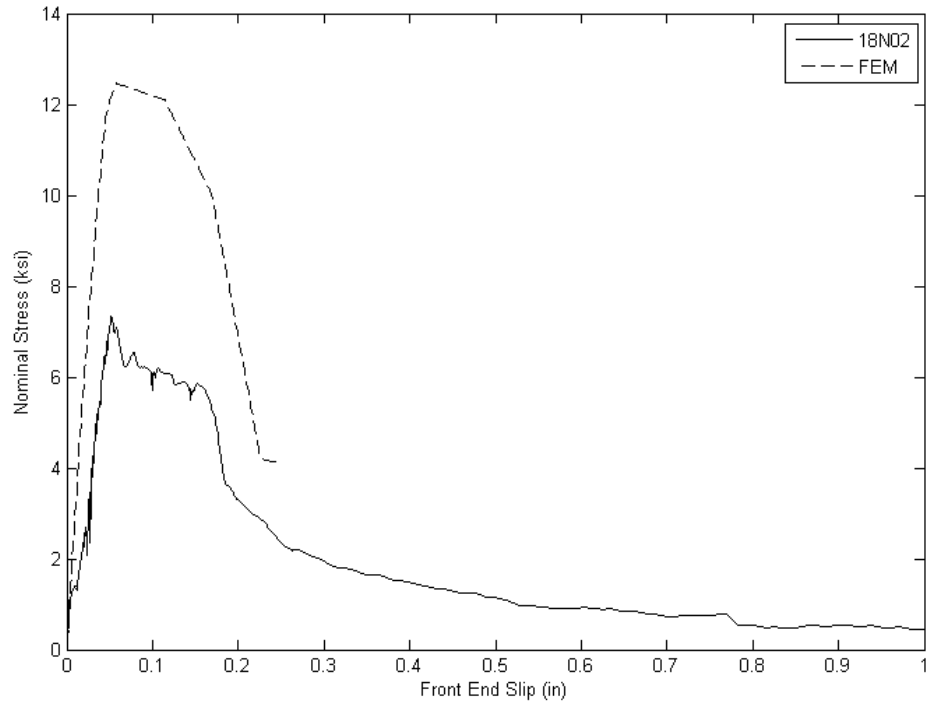


Figure E.11: 18N02

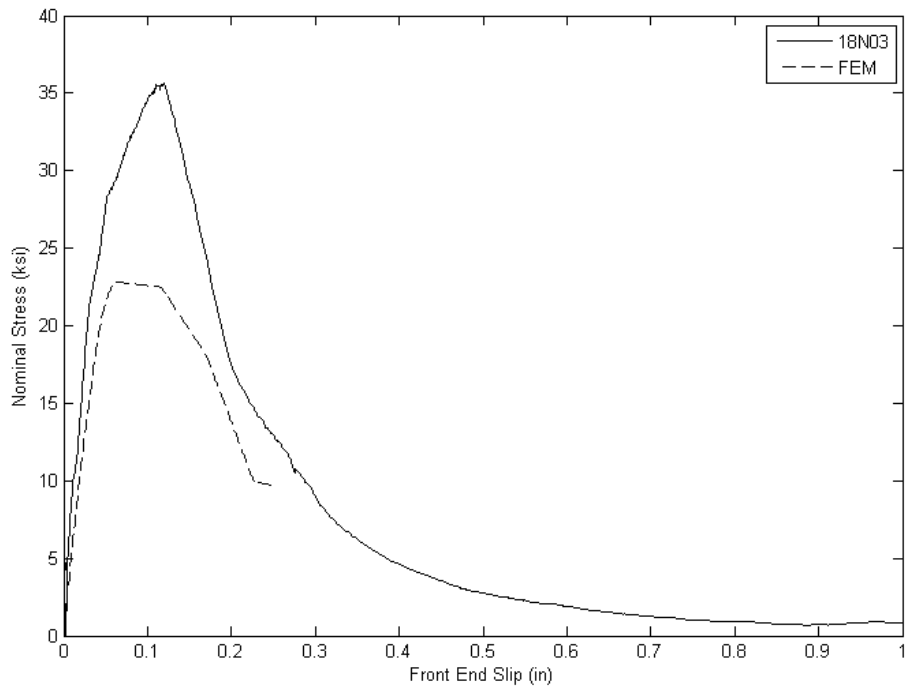


Figure E.12: 18N03

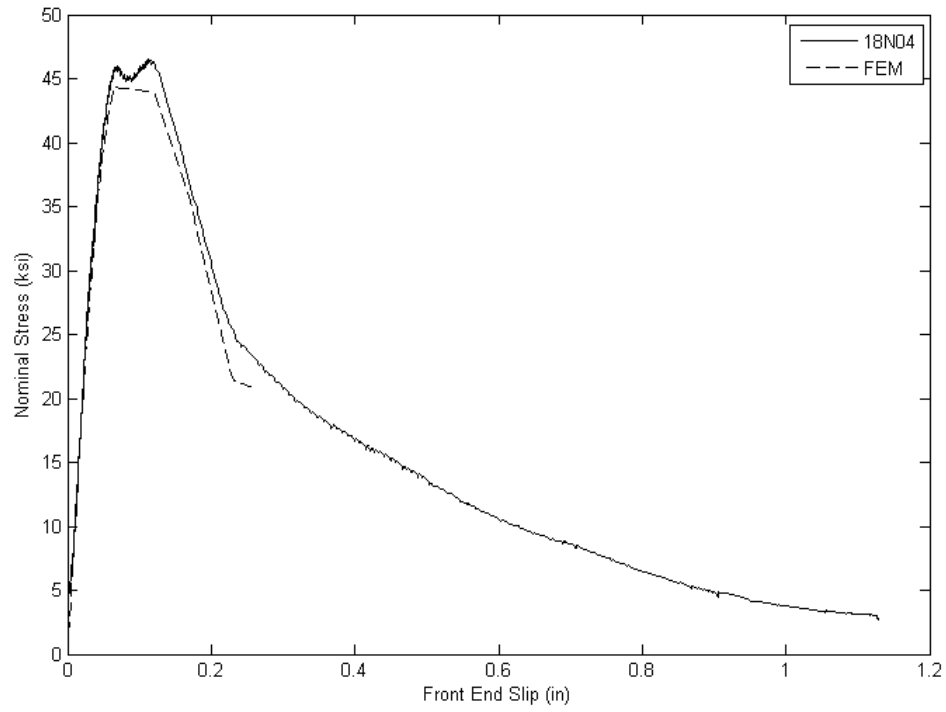


Figure E.13: 18N04

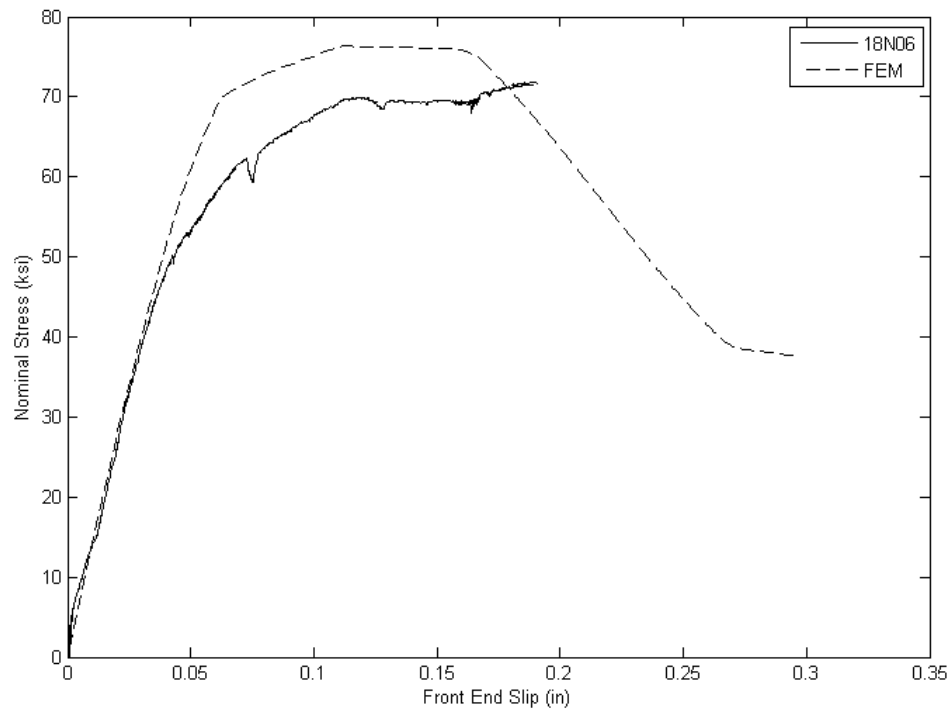


Figure E.14: 18N06 (Note: Displacement measurements became unreliable before peak load reached.)

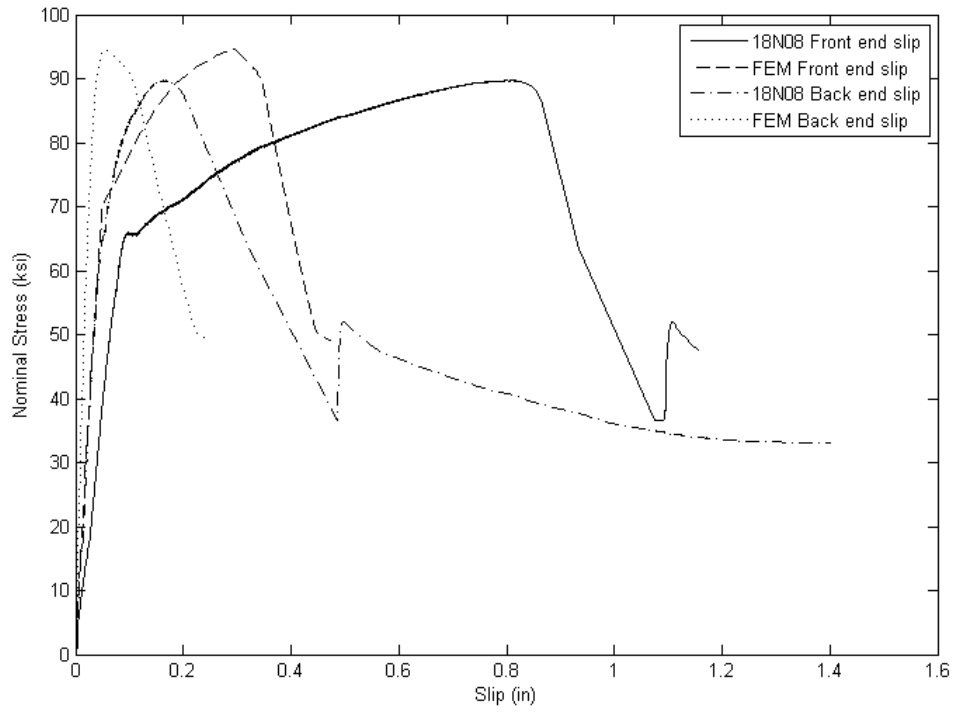


Figure E.15: 18N08

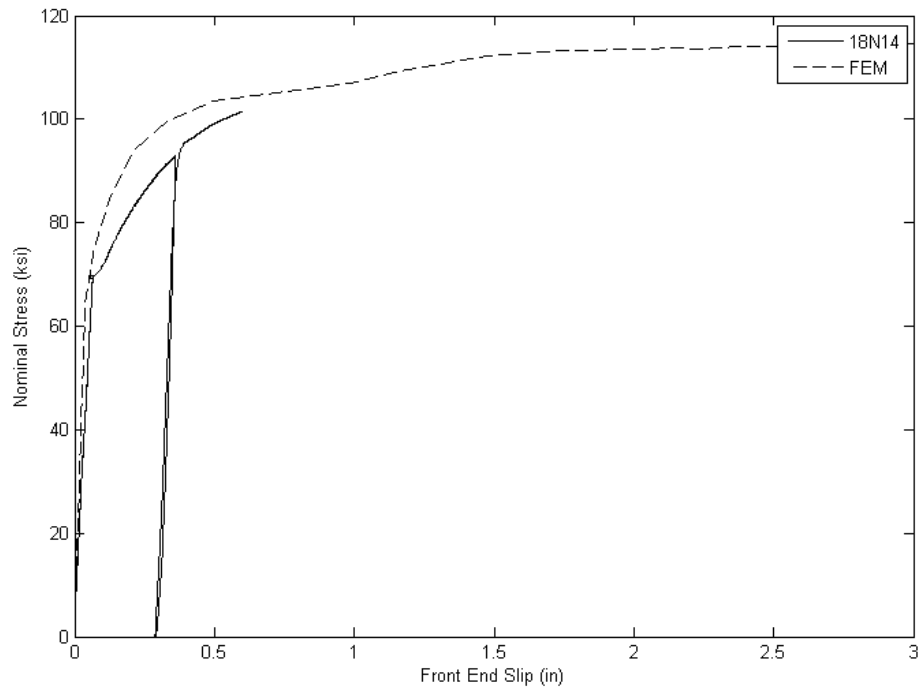


Figure E.16: 18N14 (Note: Displacement measurements became unreliable before peak load reached)

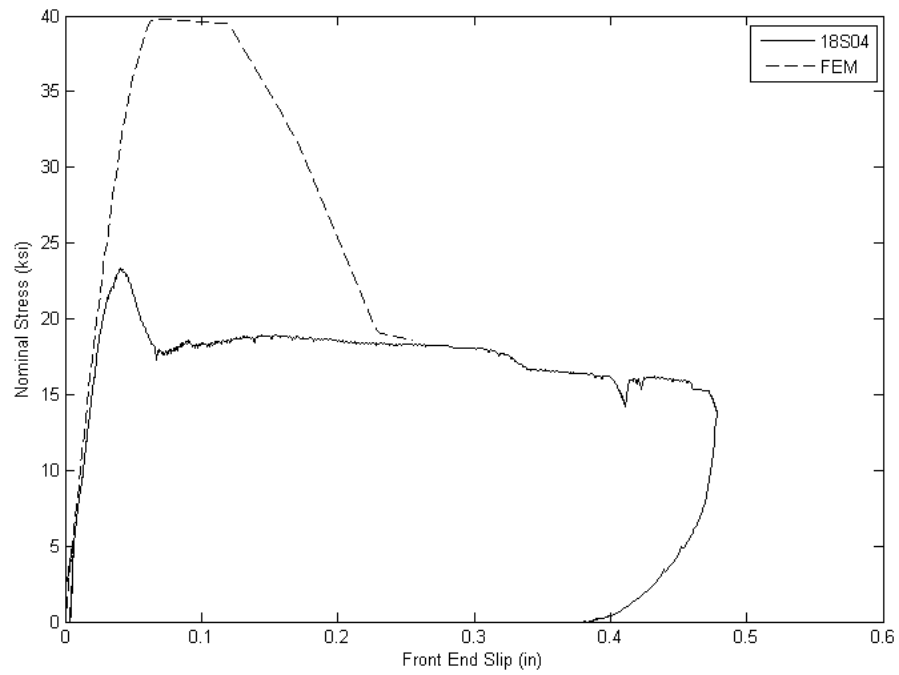


Figure E.17: 18S04 (Note: concrete splitting mode not included in model)